UCLA
UCLA Electronic Theses and Dissertations

Title
Micromechanical Resonators with Nanoporous Materials for Enhanced Vapor Sensing

Permalink
https://escholarship.org/uc/item/2x5235rp

Author
Hwang, Yong Ha

Publication Date
2012

Peer reviewed|Thesis/dissertation

eScholarship.org Powered by the California Digital Library
University of California

UNIVERSITY OF CALIFORNIA

Los Angeles

Micromechanical Resonators with Nanoporous Materials for Enhanced Vapor Sensing

A dissertation submitted in partial satisfaction of the

requirements for the degree Doctor of Philosophy

in Electrical Engineering

by

Yong Ha Hwang

2012

© Copyright by

Yong Ha Hwang

2012

ABSTRACT OF THE DISSERTATION

Micromechanical Resonators with Nanoporous Materials for Enhanced Vapor Sensing

by

Yong Ha Hwang

Doctor of Philosophy in Electrical Engineering

University of California, Los Angeles, 2012

Professor Rob N. Candler, Chair

Resonant sensors can detect chemical and biological analytes by measuring shifts in the resonant frequency due to adsorption-induced mass changes. This work describes a sensing approach that provides the sensitivity of nanoscale devices without sacrificing capture area through the use of highly porous surface so as to increase the adsorbed mass. Three strategies for exceptional capturing area are studied to achieve high sensitivity gas sensors; (1) porous-etched silicon resonator, (2) ZIF (zeolitic imidazolate framework)-agglomerated resonator by drop casting, and (3) ZIF-coupled resonator by dielectrophoresis.

Microscale silicon resonators with nanoscale pores are developed for increased surface area. Increased mechanical stability and detection performance are also achieved by keeping parts of the resonating device nonporous and adding a receptor coating. Partially-porous silicon

resonators and receptor-coated partially-porous silicon resonators are improved up to 165% and 654% in resonator sensitivity, respectively, as compared to nonporous silicon resonators.

This work also presents ZIF-agglomerated resonators whose sensitivity shows an improvement up to 78 times (780% improvement) over the silicon resonators with identical dimensions while additionally utilizing the inherently selective adsorption properties of ZIFs. ZIF nanoparticles provide previously unattainable surface area as well as the ability to tailor crystal structure for inherent selectivity. A unique fabrication technique in combination with a drop casting method is presented, enabling deposition of a wide variety of materials on released MEMS devices by providing a temporary support layer of photoresist.

Lastly, ZIF nanoparticles are coupled to resonators using dielectrophoresis (DEP) to maximize adsorption of ZIFs so as to gain further sensitivity enhancement. By utilizing an inherently sensitive and selective adsorption property of ZIFs, amplitude of frequency shift shows a sensitivity improvement up to 158 times over the silicon resonator. Also, consistent decay constant of the frequency shift provide significant chemical recognition ability of the ZIF-coupled resonant sensor.

The dissertation of Yong Ha Hwang is approved.

Pei-Yu Chiou

Oscar M. Stafsudd

Benjamin S. Williams

Rob N. Candler, Committee Chair

University of California, Los Angeles

2012

TABLE OF CONTENTS

Chapter 1 Introduction 1
1.1 Gas detection 1
1.1.1 Conductivity sensors 1
1.1.2 Piezoelectric sensors....................3
1.1.3 Optical sensors 4
1.1.4 MOSEFET (Metal-oxide-semiconductor field-effect transistor) sensors 6
1.1.5 Cantilever sensors 7
1.2 Organization 9
Chapter 2 MEMS/NEMS resonant sensors 10
2.1 Theory of resonant sensors....................11
2.1.1 Resonant device principles 11
2.1.2 Sensitivity as a mass sensor 14
2.2 Enhancement of sensitivity 15
2.2.1 Scaling of resonant sensors....................15
2.3 Surface enhanced resonant sensors....................19
Chapter 3 Porous silicon resonators....................20
3.1 Design and Simulation 21
3.2 Fabrication....................28
3.3 Experimental results 33
3.3.1 Experimental Setup 33
3.3.2 Changes in resonator frequency and Q by porosification....................37
3.3.3 Vapor detection 38
Chapter 4 Receptor-coated porous silicon resonators....................43
4.1 Fabrication of receptor-coated porous silicon resonators 43
4.2 Experimental results 46
Chapter 5 ZIF-agglomerated resonant gas sensor using a drop casting manipulation 51
5.1 ZIF (zeolitic imidazolate frameworks) 51
5.2 Fabrication process for integrating nanoparticles with released structures 52
5.3 Device design 53

5.4 Fabrication......55
5.5 Experimental results 62
Chapter 6 ZIF-coupled resonant gas sensor using dielectrophoretic nanoassembly 71
6.1 Dielectrophoresis......71
6.1.1 Simulation of DEP force......72
6.1.2 Measurements of Clausius-Mossotti (CM) factor......74
6.2 Fabrication......79
6.3 Test setup for self-oscillating 82
6.4 Experimental results 86
Chapter 7 Conclusions 93

LIST OF FIGURES

Figure 1. Typical structure of a conductivity sensor [1]. 3

Figure 2. Quartz crystal microbalance with sensing material [3]. 4

Figure 3. Surface acoustic wave sensor [4]. 4

Figure 4. Optical fiber sensor for gas detection [7]. 5

Figure 5. Cross-section image of fabricated porous silicon [9]...6

Figure 6. MOSFET gas sensor with gas sensitive membrane deposited on top of SiO_2 [11]. 7

Figure 7. SEM image of a 2 μm long, doubly-clamped NEMS resonator and zeptogram-scale mass sensing experimental result [25, 28]...11

Figure 8. Mass-spring system. 11

Figure 9. Mass spring system in the presence of friction and external driving force. 12

Figure 10. Transfer function vs. frequency for a mass-spring-dashpot system. At resonance, the mass and spring pass harmoniously back and forth between one another. The amplitude at resonance is determined by driving force and dissipation from the dashpot............................13

Figure 11. Schematic of cantilever in a translational mode (left) and resonant frequency shift caused from adsorption of mass (right). 15

Figure 12. Required time for accumulating analyte molecules on a disk-shaped surface. Hydrogen gas molecules at 1 ppb are used as a model analyte for this example. For radii below 10 nm, more than one hour is necessary to detect 1 fg of analytes...17

Figure 13. Quality factor vs. resonator size, where thickness is defined in the direction of the smallest dimension. The dashed line is a guide to the eye. 18

Figure 14. Schematic diagrams of (a) the nonporous silicon resonator, (b) the fully-porous silicon resonator, and (c) the partially-porous silicon resonator. The nonporous silicon resonator consists of whole polycrystalline silicon deposited with LPCVD. While both center paddle and torsional beams of the fully-porous structures consist of porous-etched silicon, for the partially-

porous resonator, only the center paddle is porous-etched, and the torsional beams and edges of the center paddle remain nonporous-etched silicon in order to maintain their stiffness...........21

Figure 15. First four modes of oscillation of the designed resonator. (a) First mode corresponds to motion of a translational or trampoline mode. (b) Second mode corresponds to twisted motion of a torsional mode. (c) and (d) Additional modes are observed at higher frequencies. Note that change in color from blue to red illustrates greater displacement; however, amplitude of displacement of each mode is normalized to its maximum value. 23

Figure 16. (a) Schematic diagram of resonator (l_1 = 45 μm, w_1 = 10 μm, l_2 = w_2 = 45 μm) with a composite nonporous and porous silicon layer of thickness t_b and t_t, respectively. (b) Fabricated porous silicon layer on the polysilicon in cross-section view. 24

Figure 17. Simulated torsional resonant frequencies of resonators with different surfaces of the fully-porous (a) and the partially-porous silicon resonators (b), respectively. Resonant frequency is simulated for a range of Young's modulus values for the porous silicon. The Young's modulus is found by fitting the simulations to the experimentally measured resonant frequency. The Young's modulus of the top porous silicon layer of the two-layered structures ranges between 0.1 GPa and 100 GPa, while that of the bottom nonporous silicon layer remains as constant at 135 GPa. Square, circle, triangle, and star shaped points are measured average values for each resonator type etched for 10, 20 and 30 seconds, respectively. By comparing simulated resonant frequencies with experimentally measured values of each resonator type, the effective Young's modulus of the porous silicon layer used for these devices can be estimated at ~5 GPa..27

Figure 18. Fabrication process for partially-porous silicon resonators. (a) Deposition of SiO_2 and polysilicon by LPCVD. (b) Photolithography and polysilicon etching by DRIE for defining body of the resonator. (c) Photolithography for opening of porous region. (d) Au catalyst layer deposition by E-beam evaporator. (e) Porous silicon etching and Au layer removal. (f) Sacrificial layer etching and drying with CPD. Step (c) is omitted for fully-porous silicon resonators...29

Figure 19. Schematic of the electroless metal-assisted porous etch process...............................30

Figure 20. SEM images showing l_1 = 45 µm, w_1 = 5 µm, and $l_2 = w_2$ = 45 µm resonators. (a) Nonporous silicon resonator. (b) Fully-porous silicon resonator (c) Partially-porous silicon resonator. Both center paddle and torsional beams of nonporous and fully-porous silicon resonators consist of LPCVD-deposited silicon and porous-etched silicon, respectively. For the partially-porous resonator, only the center paddle is porous-etched. 31

Figure 21. Cross sectional SEM images of porous-etched silicon layer for different etch times, t_{etch}: (a) 0 second (*i.e.* nonporous silicon), (b) 10 seconds, (c) 20 seconds, (d) 30 seconds. 32

Figure 22. AFM images of (a) the nonporous silicon and (b) the porous silicon. The porous silicon is etched for 30 seconds. The values of the RMS roughness are 7.8 nm and 264 nm, respectively. 32

Figure 23. (a) Schematic diagram. (b) Photos of the experimental setup for mechanical actuation and readout by using a Laser Doppler vibrometer. 34

Figure 24. (a)-(e) Comparison of positions of laser beams of the LDV system. The beams are on edge-edge, corner-corner, corner-bottom, corner-pad, and center-pad in order. (f) The measured amplitudes of each resonance mode depend on the positions of two beams. 36

Figure 25. Measured quality factors of resonators. Above 0.1 Torr, data of the nonporous, fully-porous, and partially-porous silicon resonator are described by $Q = 129/P^{0.953}$ (dash dot line), $Q = 168/P^{0.808}$ (dashed line) and $Q = 135/P^{0.823}$ (solid line), respectively. Below that pressure, another energy loss mechanism limits the quality factor. 38

Figure 26. Measured frequency spectra of (a) nonporous and (b) fully porous silicon resonators with no IPA (dashed line) and 5000 ppm of IPA (solid line). 39

Figure 27. A comparison of relative frequency shifts vs. gas concentration. The error bars indicate the standard deviation in the data, which comprised five measurements at five minute intervals for each concentration. 41

Figure 28. Fabrication process for partially-porous silicon resonators. (a) Deposition of SiO_2 and polycrystalline silicon by LPCVD. (b) Photolithography and polycrystalline silicon etching by DRIE for defining body of the resonator. (c) Photolithography for opening of selective porous region. (d) Random gold cluster coating. (e) Porous silicon etching and gold layer removal. (f)

Cr/Au deposition as linker of receptor material. (g) Liftoff of Cr/Au. (h) Sacrificial layer etching and receptor coating. 45

Figure 29. SEM images of the partially-porous silicon resonator with receptor-coated Cr/Au film. Only the center paddle is porous-etched. The porous etched region is coated with Cr/Au film and 4-MBA as receptor material. 46

Figure 30. Measured (a) resonant frequencies and (b) quality factors for different etch times and torsional beam lengths. The values of zero–second-etched condition indicate the case of nonporous silicon resonators. 47

Figure 31. A comparison of relative frequency shifts vs. gas concentration. The error bars indicate the standard deviation in the data, which comprised five measurements at five-minute intervals for each concentration. 48

Figure 32. Various MOF (metal organic framework) sensors using the MOF's property of high surface area. Sensor are based on change of (a) impedance [86], (b) and (c) refractive index [87, 88], (d) strain [89], and surface acoustic wave [90]....................52

Figure 33. (a) Sketch of the proposed nanoparticle-agglomerated resonator. ZIF nanoparticles are attached on a target region in the center paddle of the resonator. (b) Crystal structures of ZIF-69. The largest cage in each ZIF is shown with ZnN_4 in blue and CoN_4 in pink polyhedra, and the links in ball-and-stick presentation. The yellow ball indicates space in the cage. H atoms are omitted for clarity [91]....................54

Figure 34. Fabrication process for ZIF-agglomerated resonator by a drop casting. (a) Depositing of SiO_2 and polysilicon. (b) Patterning body of the resonator. (c) Etching the sacrificial layer. (d) After rinsing, replacement of rinsing liquid with melted p-DCB. (e) Coating thick photoresist. (f) Patterning the photoresist support structure as a sacrificial layer and cavities for a target region of ZIF particles. It is important to note that the PR support replaces the solid p-DCB under the released resonator and also defines the mold on top of the resonator. (e) Sweeping of distributed ZIF particles by a flat blade, leaving packed ZIFs in the cavity. (f) Dissolution of the PR support layer and sublimation drying with p-DCB. 58

Figure 35. SEM images of resonator cross-sections. (a) Cross-section taken along BB' after definition of the resonator structure. (b) Cross-section taken along CC' after patterning of the PR support layer. The PR support as the second sacrificial layer completely covers the torsional beam of the released polysilicon resonator. 60

Figure 36. SEM image of resonator cross-section cross-section taken along CC' in **Figure 35** when the PR is coated after sublimation of the p-DCB is completely finished (*i.e.*, no replacement of the PR with the p-DCB). The resonator becomes adhered to the substrate.......61

Figure 37. Tilted SEM images of the ZIF-agglomerated resonators. (a) and (b) the resonator of the same design is usually adhered to the substrate if measures are not taking to address stiction (*i.e.* after removal of the PR support with acetone, the sample is air dried). However, (c) and (d) the resonator is successfully released by the aid of the sublimation drying of p-DCB. 61

Figure 38. SEM images. (a) A silicon resonator without nanoparticles. (b) A ZIF-agglomerated resonator with a 10 µm × 10 µm × 3 µm casting of ZIFs by the drop casting method. (c) Enlarged image of ZIFs attached on the surface of the resonator. (d) Enlarged image of agglomerated ZIFs 62

Figure 39. Resonator frequency distribution and response to gas. The resonant frequency distribution of the silicon resonators without the PR support technique (*i.e.*, just a single p-DCB release), with the PR support technique (and resulting bending) with no nanoparticles, and with the PR support technique and nanoparticles. Standard deviation of the resonant frequencies is 3.87 kHz, 2.40 kHz, and 5.03 kHz, respectively. Each data point is for a separate device. Eight devices were measured for each category. 63

Figure 40. Measured noise floor and Q factors of the systems with (a) the ZIF-agglomerated resonator and (b) the silicon resonator during 1000 s measurement period with a 0.62 Hz resolution bandwidth. 65

Figure 41. Measured performance of the ZIF-agglomerated resonant gas sensors. (a) Frequency spectra of with no CO_2 (dashed line) and 9000 ppm of CO_2 (solid line). (b) A typical set of real time frequency shifts exposed to IPA and CO_2 gas. 66

Figure 42. (a) A typical set of measured frequency shifts for ZIF-agglomerated resonators exposed to CO_2 gas, (b) resonant frequency vs. analyte gas pressure (CO_2) extracted from (a). 68

Figure 43. Response of the ZIF-agglomerated, porous, and silicon resonant gas sensors to N_2, IPA and CO_2 gas. 69

Figure 44. Two dimensional simulations for parallel electrodes with a spacing of (a) 5 µm, (b) 20 µm, (c) 40 µm, and (d) 80 µm. (Surface plot: $\log_{10}$(DEP force) [N], Arrows and stream lines: ∇E^2[V^2m^{-3}], Arrow lengths do not represent magnitude of the electric field gradient.) (e) DEP forces are calculated through parametric study as the electrode gaps are changed. 74

Figure 45. Schematic and photos of the experimental setup for dielectrophoretic particle capture. 76

Figure 46. An example setup of the particle tracking plug-in. By controlling a threshold of brightness of the recorded video, particles to be tracked are selected. 77

Figure 47. Coplanar electrodes (10 µm wide and 15 µm spacing) with ZIF-69 particles at 10 kHz, 200 kHz and 1 MHz suspended in DI water. The particles are attracted to the edges of the electrode by positive DEP at 10 kHz and are repelled to the center gaps between electrodes by negative DEP at 1 MHz. 78

Figure 48. Clausius–Mossotti (CM) factor as a function of frequency for ZIF-69 in a range of 10 kHz up to 2 MHz. Particle motions are recorded and the CM factors were extracted by their velocities. The crossover frequency for positive- and negative DEP is ~300 kHz....................78

Figure 49. Fabrication process for ZIF-coupled resonator using DEP. (a) Patterning body of the resonator. (b) Lift-off for planar electrodes. (c) Covering passivation layer for the metal electrodes. (d) Etching the first sacrificial layer and filling p-DCB underneath the resonator. (e) Pouring thick photoresist over the solid p-DCB. (f) Reflowing the photoresist and patterning it as the second sacrificial layer and cavity for a target region of ZIF particles. (g) Assembling ZIF particles by DEP-induced attractive force. (f) Releasing the ZIF-coupled resonator. 80

Figure 50. Tilted-view SEM images of the fabricated resonators without ZIFs (left) and with ZIFs (right). ZIF-69 particles assembled on the surface of the resonator are shown as an inset. 82

Figure 51. (a) Experimental setup for the self-oscillation of the resonator. (b) Schematic diagram of the feedback circuit. 85

Figure 52. Sensing responses of the ZIF-coupled resonant gas sensors as a function of IPA/CO_2 gas concentration. The resonator with ZIFs assembled by DEP shows higher sensitivity than the resonator with ZIFs agglomerated by drop casting. 86

Figure 53. (a) Real time gas sensing experiment with the ZIF-coupled resonator and (b) measured noise floor is over the course of 300 sec. The standard deviation value reflects attainment of ~0.35 pg mass resolution...89

Figure 54. (a) Expanded view of the frequency drop from adsorption of IPA (blue) and CO_2 (red) with a period of 50 msec. The experimental curves are fit to an exponential decay function (light blue and light red solid lines) and the each fitting parameters are compared in **Table 7**. (b) The decay constants for IPA and CO_2 are 1.43±0.28 and 0.49±0.17, respectively. 91

LIST OF TABLES

Table 1. Summary of properties of sensor types 2

Table 2. Examples of performances of each sensor type. 9

Table 3. Comparison of thickness for each type of resonator. 25

Table 4. Electrochemical reaction of the metal-assisted porous etch 30

Table 5. Relative performances for each type of resonator...42

Table 6. Relative performance for each type of resonator. 50

Table 7. Summary of the feedback circuit design...85

Table 8. Fitting parameters of experimental frequency drops arising from different concentration of IPA and CO_2. 92

ACKNOWLEDGMENTS

I would not have been where I am today without all the help and support I received during my UCLA studies. First and foremost, I will always be grateful to my advisor, Rob N. Candler, for all his continuous guidance, encouragement, and support throughout the course of my research and dissertation. Also, I would like to thank my committee members - Professors Pei-Yu Chiou, Oscar M. Stafsudd, and Benjamin S. Williams - for their very helpful insights and suggestions.

Additionally, I would like to express my thanks to Sensors and Technology Lab members - Jere Harrison, Omeed Paydar, Jonathan Lake, Srikanth Iyer and Hyunmin Sohn - for their great help and assistance with running the experiments.

I am thankful to Jiyoung Kim, Kyungsik Shin, Sungmin Kim, Augustin Hong, Myungjun Lee and Wonho Park, who have helped me with many insightful discussions throughout my studies. Special thanks to Professors Jungho Pak, Seounoh Han and Sungkyu Seo, who have encouraged me to pursue my dreams.

I am forever indebted to my mom and dad for their understanding, endless patience and encouragement when it was most required. Thanks to my sister, Miseon. Thanks also to Myungsoo and Jungil for being my excellent friends. Perhaps most important, I would like to thank my dearest wife, Sunhee, for her love and support.

VITA

2004	B.S. in Electrical Engineering Korea University Seoul, Korea
2004-2006	Graduate Student Research Assistant Department of Electrical Engineering Korea University Seoul, Korea
2006	M.S. in Electrical Engineering Korea University Seoul, Korea
2006-2007	Assistant Research Engineer Samsung Electronics Co., Ltd. Gyeonggido, Korea
2008-2012	Graduate Student Research Assistant Sensors and Technology Loboratory Department of Electrical Engineering University of California, Los Angeles Los Angeles, California, USA

PUBLICATIONS

Journal publications

[1] Y.H. Hwang, A. Phan, K. Galatsis, O.M. Yaghi, and R.N. Candler, "Zeolitic imidazolate framework-coupled resonators for enhanced gas detection," Applied Physics Letters (In review).

[2] Y.H. Hwang, and Rob N. Candler, "Fabrication process for integrating nanoparticles with released structures using photoresist replacement of sublimated p-dichlorobenzene for temporary support," Journal of Microelectromechanical Systems (Accepted for publication).

[3] Y.H. Hwang, F. Gao, A.J. Hong, and R.N. Candler, "Microresonators with partially-porous silicon surface for improved vapor detection," Journal of Microelectromechanical Systems, Vol. 21, No. 1, pp. 235-242, 2012.

[4] J.Y. Kim, A.J. Hong, S.M. Kim, K.S. Shin, E.B. Song, Y.H. Hwang, F. Xiu, K. Galatsis, C.O. Chui, R.N. Candler, S.Y. Choi, J.T. Moon, and K.L.Wang, "A stacked memory device on logic 3D technology for ultra high density data storage," Nanotechnology, Vol. 22, Issue. 25, pp. 254006-1, 2011.

[5] S.M. Kim, E.B. Song, S. Seo, D.H. Seo, Y.H. Hwang, R. Candler, and K.L. Wang, "Suspended multi-layer graphene beam electromechanical switch with ideal on-off characteristics and zero leakage current," Applied Physics Letters. Vol. 99, Issue. 2, pp. 023103, 2011.

[6] Y.H. Hwang, S.O. Han, B.K. Lee, J.S. Kim, and J. Pak, "Two-step micromirror for low voltage operation," KIEE International Transactions on Electrophysics and Application, Vol. 5-C, No. 6, pp. 270-275, 2005.

Conference proceedings

[1] Y.H. Hwang, A. Phan, K. Galatsis, O.M. Yaghi, and R.N. Candler, "ZIF-coupled microresonator for highly sensitive and selective gas detection," in Proc. International Conference on Miniaturized Systems for Chemistry and Life Science (MicroTAS 2012), pp. 231-233, 2012.

[2] Y.H. Hwang, S.M. Kim, and R.N. Candler, "Receptor-coated porous silicon resonators for enhanced sensitivity of vapor detection," in Proc. 2011 Joint Conference of the IEEE International Frequency Control Symposium and European Frequency and Time Forum, p. 294, 2011.

[3] Y.H. Hwang, F. Gao, and R.N. Candler, "Porous silicon resonator for sensitive vapor detection," in Proc. A Solid-State Sensors, Actuators and Microsystems Workshop (Hilton Head 2010), pp. 150-153, 2010.

[4] R.N. Candler, Y.H. Hwang, and F. Gao, "Sensitivity enhancement of vapor sensors with porous silicon resonant structures," SPIE Defense, Security and Sensing 2010 (Invited paper), Vol.7679, p. 76790K

[5] Y.H. Hwang, F. Gao, and R.N. Candler, “Porous silicon resonator for sensitive vapor detection,” in Proc. the 4th Nagoya University–UCLA International Symposium, p.22, 2009.

[6] S.O. Han, Y.H. Hwang, J.S. Kim, J.S. Kim, and J. Pak, "A novel double-stacked electrostatic micromirror for low voltage operation," in Proc. 13th Korean Conference on Semiconductors, pp. 235-236, 2006.

[7] Y.H. Hwang, S.O. Han, B.K. Lee, J.S. Kim, and J. Pak, "A low voltage two-step micromirror for the pinhole of the confocal microscope," in Proc. Conf. IEEE/LEOS Optical MEMS, pp. 49-50, 2005.

[8] Y.H. Hwang, S.O. Han, B.K. Lee, J.S. Kim, and J. Pak, "Low voltage two-step micromirror for in-vivo endoscopic biopsy," in Proc. Conf. 7th Korean MEMS, pp.216-219, 2005.

Chapter 1 Introduction

Sensors are devices that are able to interface the chemical and physical world with, in most cases, that of electronics in order to store, process and present data. For example, a gas sensor detects the presence of various gases within an area and transduces it into a resulting signal, usually as part of a health and safety system (e.g., medical diagnostics, air quality monitoring, and detection of toxic and explosive materials). There are continuing needs for the development of fast, sensitive, reliable, and cheap sensors in environmental, agricultural, biomedical, and industrial applications.

1.1 Gas detection

Gas molecules interact with solid-state sensors by absorption, adsorption or chemical reactions with the sensor materials. There are many ways to detect gases by monitoring various physical/chemical changes. The most common types of changes used in gas sensor systems are shown in Table 1 for a range of sensing techniques.

1.1.1 Conductivity sensors

Metal oxides and conducting polymers are the most commonly used sensing materials in conductivity sensors, which are based on the principle that changes in the material properties resulting from interaction with analytes lead to a change in resistance in the sensor. The materials are coated on interdigitated or parallel electrodes so as to form electrical connections, as shown in Figure 1 [1].

Metal oxide sensors typically consist of a metal-oxide (e.g., SnO_2, TiO_2, ZnO, ZrO_2) deposited on a ceramic substrate, such as alumina. The resistance is retained to a background level at equilibrium when oxygen from the air is dissolved in the metal-oxides' lattice. During

the measurement, the volatile analytes are adsorbed at the surface and react with the dissolved oxygen species, causing a further change in the resistance of the device. The sensitivity and selectivity of the metal oxide sensors are determined by the choice of the semiconductor material, the modification by doping, and the operational temperature. Since very high temperatures (typically 200-500 ˚C) are necessary for achieving effective reactions, a heating element should be integrated with the sensor when metal oxides are employed as a sensing material [1].

Table 1. Summary of properties of sensor types

Principle	Sensor type	Advantages	Disadvantages
Conductivity	Metal oxides	Fast response	High operating temperature
	Polymer composites	Cheap, various materials for selectivity	Response drift due to aging
Piezoelectricity	SAW	Fast response, IC integratable	Difficult to integrate Poor signal-to-noise performance
	QCM	Stable quality, diverse range of coating	Difficult to integrate
Optical intensity/spectrum	Optical fibers	Immune to electromagnetic environments, diverse range of coating	Short lifetime due to photobleaching, Need light detection, Difficult to integrate
	Porous silicon	IC integratable	Difficult to reproduce, need light detection
Work function	MOSFET	CMOS comparability, reproducibility, low cost	Response drift due to temperature
Mechanical motion	Cantilever	Ultrafine minimum detectable mass, reduced size, on-chip integration	Fragility to mechanical shock

Polymer composite sensors work on the principle that vapor analytes permeate into the polymer and cause the polymer film to expand, inducing an increase in the electrical resistance

arising from reduction of the number of conductive pathways for charge carriers due to the expansion of the polymer. The response depends on the permeability and mobility of the anlaytes inside the polymer, the volume of the polymer, and the operational temperature. Because various polymers are available on the market, high discrimination of the sensor can be easily achieved with relatively inexpensive costs. The main drawback, however, is aging, resulting in drift of the sensor [2].

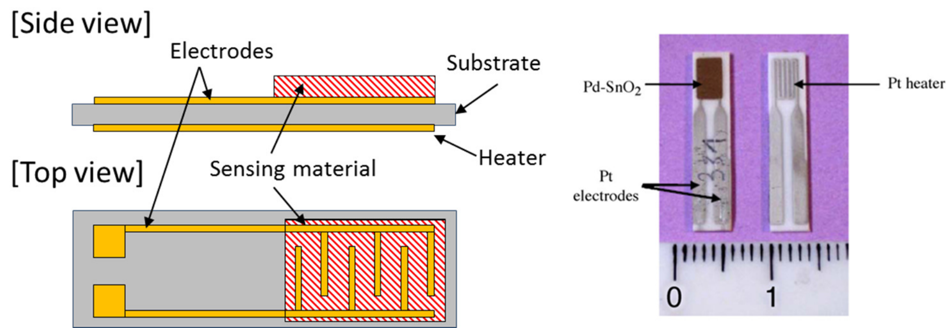

Figure 1. Typical structure of a conductivity sensor [1].

1.1.2 Piezoelectric sensors

QCM (quartz crystal microbalance) and SAW (surface acoustic wave) sensors consist of a piezoelectric material coated with a sensing membrane and electrodes. When an ac voltage is applied across the piezoelectric quartz crystal, inducing oscillation at its resonant frequency, increase in mass due to adsorbate species on the membrane modulates the resonant frequency, as shown in Figure 2 [3]. The SAW sensors detect the frequency of the acoustic wave, which is created by one electrode pair and then changed during propagating through a sensing membrane, as shown is Figure 3 [4]. The difference between QCM and SAW is the oscillating mode, in the entire bulk and at the surface, respectively. The selectivity and sensitivity rely on the

composition of the coated membrane for sensing, which enables the sensors to be tuned for certain adsorbate species. One current challenge for piezoelectric sensors is that they are difficult to integrate [5]. Besides, a good calibration technique is required to correlate obtained data [6].

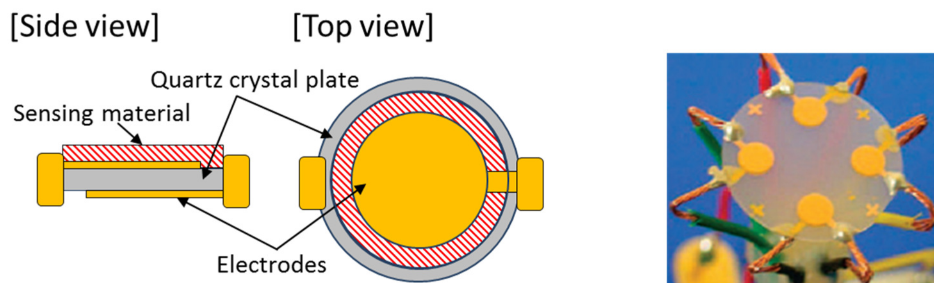

Figure 2. Quartz crystal microbalance with sensing material [3].

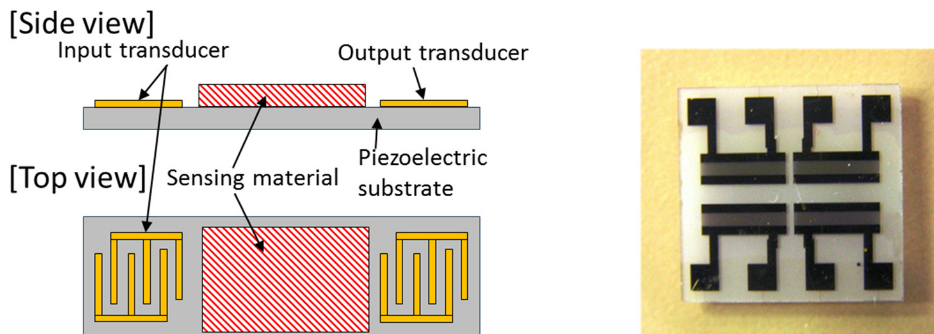

Figure 3. Surface acoustic wave sensor [4].

1.1.3 Optical sensors

Fluorescence techniques generally employ optical fibers [7]. The sides or tips of the optic fibers are coated with fluorescent dyes. The polarity of the light in the fibers is affected by analyte molecules, allowing changes in the dye's optical properties, such as intensity and

wavelength, as shown in Figure 4. The sensitivity of the fiber sensor is related to the type of fluorescent dye or mixture of dyes. However, the supporting electronics are very complex, leading to increased cost. In addition, the sensors have quite a short lifetime because the optical changes from the fluorescent dyes are accompanied with photobleaching [8]. Thus, effective monitoring temporal responses should be prepared.

Visible photoluminescence from porous silicon has attracted considerable attention. The efficiency and wavelength range of the emitted light are affected by modulated photonic bandgaps of the porous silicon surface, which is apparently dependent on geometry of pores, as shown in Figure 5 [9]. Hence, the factors that affect the sensitivity include pore size, depth, density, and uniformity. Due to its large internal surface and high chemical reactivity with the environment, the porous silicon has stimulated great interest on sensing applications. However, since formation of pores inside silicon significantly varies depending on the property and quality of the substrate silicon (e.g., doping type and concentration, defects, and uniformity of doping), reproducibility of the sensor must still be worked out [10]. Moreover, diverse ranges of functionalization are restricted because the characteristics of photoluminescence are strongly dependent on porous surface condition.

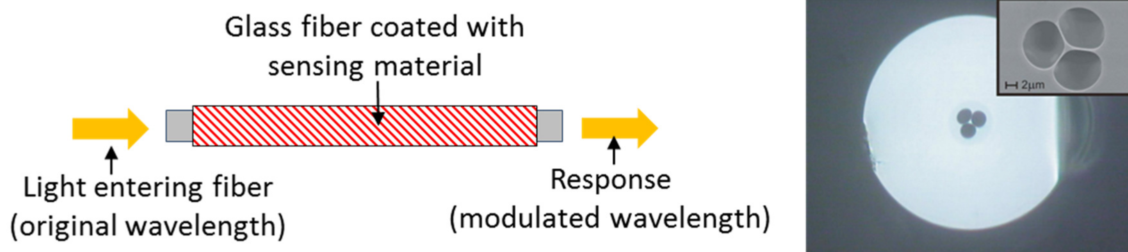

Figure 4. Optical fiber sensor for gas detection [7].

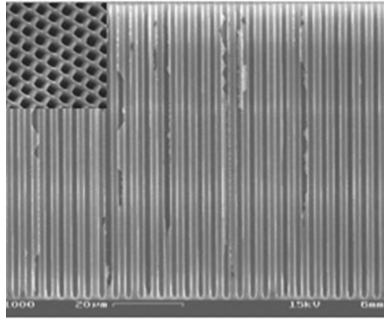

Figure 5. Cross-section image of fabricated porous silicon [9].

1.1.4 MOSEFET (Metal-oxide-semiconductor field-effect transistor) sensors

As shown in Figure 6, the MOSFET sensor is based on changes in threshold voltage and source-drain current due to interaction of the gate material, usually a catalytic metal, with analytes [11]. The interaction means a change in the work function of the metal and the oxide insulator of the gate derived from changes in charge carriers. The MOSFET sensors offer a high sensitivity and a real simplicity in function. In addition, the possibility of easily combining with control electronics allows simplified design of an entire sensor system. The factors that affect the sensitivity of the FET-based devices include operating temperature, composition and structure of the catalytic metal. In order to achieve a high surface-to-bulk ratio for analyte accessibility, various nanowires and nanotubes can be deployed on the gate or channel between source and drain of the MOSFET. However, the MOSFET should overcome issues arising from temperature-induced drifts [12, 13].

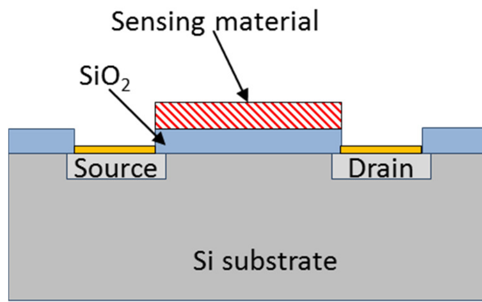

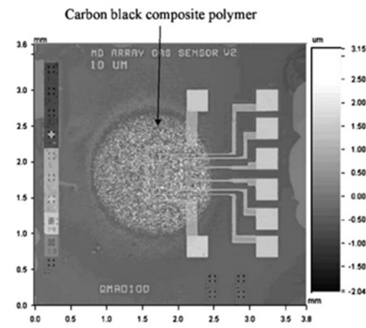

Figure 6. MOSFET gas sensor with gas sensitive membrane deposited on top of SiO_2 [11].

1.1.5 Cantilever sensors

MEMS and NEMS devices create opportunities for novel, label-free detectors with high sensitivity and fine resolution. They are based on the change of mechanical motion induced by stress on their surface or their own resonant frequency due to interaction with adsorbate species.

In a first operating mode, static deflection of the cantilever is detected, based on change in difference of surface stress between the two faces of the cantilever. A bending is explained by Stoney's formula, [14]

Equation 1

$$z = \frac{3(1-\nu)L^2}{Et^2}\sigma$$

Here, z is the displacement, ν is the Poisson's ratio, L is the length, E is the Young's modulus, t is the thickness, and σ is the surface stress of the cantilever. Accordingly, this technique has been used to directly measure change in surface stress as a sensing method by functionalizing one surface with a specific receptor material. When analyte binds to the surface, causing the surface stress, the cantilever will bend up or down depending on direction of the stress. From Equation 1, it is clear that the amplitude of deflection is related to the length and thickness of the cantilever, so that longer and thinner devices are preferred for improved motion detection. Particularly this

principle is most promising to study in biological reactions that take place in liquid, such as detecting antigen or antibody [15, 16]. It is because a static deformation of the cantilever in liquid is relatively insensitive to damping and thus energy dissipation than a dynamic motion used for dynamic operation, which is described in the following paragraph.

The second operating mode of the cantilever sensors is based on the fact that the resonant frequency of the cantilever depends on the total mass of the cantilever and the resonant frequency shifts downward as the mass increases. The mechanism will be explained in detail in Chapter 2, and this work shall focus on the so-called resonant devices.

Compared to aforementioned gas sensor techniques, especially commercially available gas sensors such as the QCM and SAW sensors, the resonant nano/micromechanical cantilever features the advantages of high sensitivity, ultrafine minimum detectable mass, reduced device size, on-chip integrated self-sensing elements such as piezoresistors, CMOS compatibility, and integration into arrays for multiplexing, as compared in Table 1. Thus, cantilever sensors are promising for a sensor platform for the detection of chemical and biological analytes. However, energy dissipations, which impact performances of MEMS/NEMS resonators operating at room temperature, are still not fully understood [17].

Table 2. Examples of performances of each sensor type.

Sensor type	Sensitivity	Detected range	Detection limit	Reference
Polymer composites	1×10^{-3}% (ΔR/R)/ppm for ethanol at 50 kΩ	100-10000 ppm	$\leq$ 1 ppm	[18]
	5×10^{-3}% (ΔR/R)/ppm for C_3H_8 at 350 ˚C	250-2000 ppm	$\leq$ 1 ppm	[1]
QCM	0.3×10^{-6}% ((Δf/f)/ppm for H_2O at 10 MHz (0.03 Hz/ppm)	1000-8000 ppm	1 ng mass change	[19]
Optic fiber	1×10^{-3}% (absorbance)/ppm for NH_3	200-10000 ppm	1 ppm	[20]
MOSFET	0.5×10^{-3}% ((ΔV/V)/ppm for toluene at 0.595 V (2.8 uV/ppm)	0.1 ppm	$\leq$ 1 ppm	[11]
Resonant cantilever	1.3×10^{-3}% (Δf/f)/ppm for DIMP (diisopropylmethyl phosphonate) at 8 MHz (7.7 kHz/ppm)	0.1-1.5 ppm	0.6 ppb	[21]

1.2 Organization

The remainder of this work is organized as follows:

Chapter 2 details the background and theory of MEMS/NEMS resonant sensors.

Chapter 3 describes the design and the fabrication of the porous silicon resonators.

Chapter 4 is an explanation of the receptor-coated porous silicon resonators.

Chapter 5 is a study of ZIF (zeolitic imidazolate framework)-agglomerated resonator, which is fabricated by drop casting method.

Chapter 6 demonstrates enhanced sensitivity and selectivity using the ZIF-coupled resonator using dielectrophoresis force.

Chapter 7 is a summary of the work.

Chapter 2 MEMS/NEMS resonant sensors

Until the late 1980s, the main detection methods used in sensors include thermoelectric effect (Seebeck effect) [22], electrochemical approach (potentiometric or amperometric) [23], optical spectroscopy [23], and mass detection by piezoelectricity [24]. Thereafter, advances in microelectromechanical systems (MEMS) have developed sensors that involve transduction of mechanical energy. Especially, development of microfabricated cantilevers for atomic force microscopy (AFM), which utilized sharp tip to mechanically inquire surface geometry, implied an important milestone in technological approaches to MEMS sensors. More recently, scaling the dimensions of the mechanical structures has led to a new generation of systems called nanoelectromechanical systems (NEMS) [25]. Operations of MEMS/NEMS sensors are based on mechanical motions and deformations of their microfabricated components, such as single-clamped beams (cantilevers), double-clamped suspended beams (bridges), or suspended diaphragms. MEMS/NEMS are being considered for sensing application with a hope of acquiring better sensitivity because the relative change of analyte is bigger for smaller devices.

MEMS/NEMS resonators have been employed in a wide variety of applications, including force or displacement detection, scanning probe microscopy, and resonant mass sensing of chemical and biological species. In physical, chemical and biological application, the vibrational motion of the device is changed by binding events on the device surface altering the total mass, allowing for measurement of the mass via a shift in resonant frequency. (Given its small mass changes, resonator's compliance is unaffected.) As shown in Figure 7, The tiny active mass of the devices enables them to be extremely sensitive to added mass of the adsorbates [26], [27] [28].

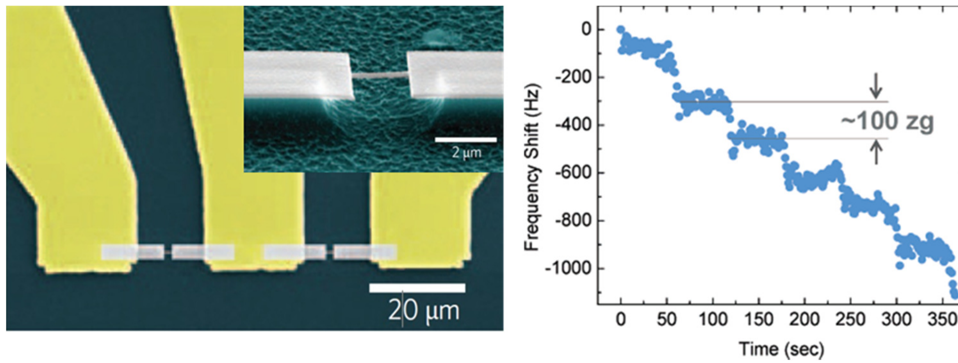

Figure 7. SEM image of a 2 μm long, doubly-clamped NEMS resonator and zeptogram-scale mass sensing experimental result [25, 28].

2.1 Theory of resonant sensors

2.1.1 Resonant device principles

A mechanical resonator can be modeled as a simple harmonic oscillator. Given a mass-spring system as shown in Figure 8, which is a point mass m, suspended from a motionless support by a massless spring having stiffness k, the goal is to find a relationship that describes oscillating properties.

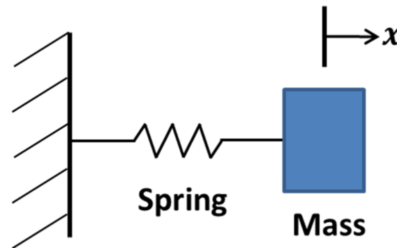

Figure 8. Mass-spring system.

Using Newton's second law, applied forces are given by $\sum F_i = ma = m\ddot{x} = m\frac{d^2x}{dt^2}$, where F_i are the individual forces consisting of the system. In this simplest case which has only one force element from the spring, $F_{spring} = -kx$, the equation of motion is written in the form

Equation 2

$$\mathrm{m}\ddot{x} + kx = 0$$

Solution of the differential equation is given by

Equation 3

$$\mathrm{x(t) = Asin}(w_0 t + \phi)$$

where $w_0 = \sqrt{\frac{k}{m}}$, the natural frequency of undamped oscillations, A is the amplitude, and ϕ is the initial phase of free oscillation.

In the case of oscillations in the presence of friction and external driving force, the system is illustrated as shown in Figure 9.

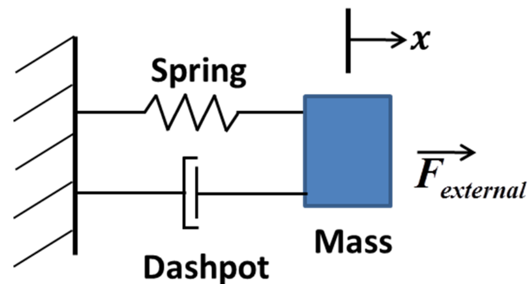

Figure 9. Mass-spring system in the presence of friction and external driving force.

The individual forces are from the spring, dashpot, and externally applied force, $f(t)$. The governing equations for the spring and dashpot are $F_{spring} = -kx, F_{dashpot} = -b\dot{x}$. Summing all these forces gives

Equation 4

$$f(t) - kx - b\dot{x} = m\ddot{x}$$

Assuming that only periodic signals are used, the transfer function H(s) is given by Fourier analysis

Equation 5

$$\mathrm{H(w)} = \frac{\mathrm{X(w)}}{F(w)} = \frac{1/m}{-w^2 + jw\frac{b}{m} + \frac{k}{m}}$$

which is illustrated in Figure 10.

For systems with small dissipation (small b), the resonant frequency is approximately given by

Equation 6

$$\mathrm{w_n} = \sqrt{\frac{\mathrm{k}}{\mathrm{m}}}, \mathrm{or}\ f_0 = \frac{1}{2\pi}\sqrt{\frac{\mathrm{k}}{\mathrm{m}}}$$

The resonant frequency is generally used as a starting point in estimating the mass sensitivity of resonant sensors of various and sizes.

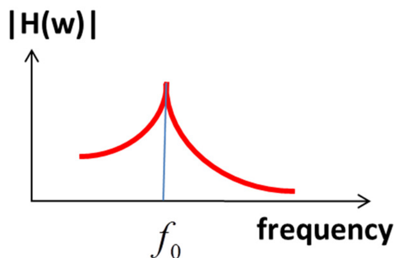

Figure 10. Transfer function vs. frequency for a mass-spring-dashpot system. At resonance, the mass and spring pass harmoniously back and forth between one another. The amplitude at resonance is determined by driving force and dissipation from the dashpot.

2.1.2 Sensitivity as a mass sensor

For mass sensitivity of a resonant sensor, taking the natural log of Equation 6, we have

Equation 7

$$\ln(f) = \ln\left(\frac{1}{2\pi}\right) + \frac{1}{2}\ln(k) - \frac{1}{2}\ln(m)$$

Assuming the equivalent stiffness of the resonator due to an infinitesimal dimensional change, Differentiated Equation 7 predicts that the change in the resonant frequency will be

Equation 8

$$\frac{\partial f}{f} = -\frac{1}{2}\frac{\partial m}{m}$$

This expression assumes that an elastic property (therefore the stiffness) of the resonator is unaffected (*i.e.* $\partial k \approx 0$) by small changes in mass by the added analytes (*i.e.* $\partial m \ll m$). Thus the mass sensitivity is typically defined as the resonant frequency shift per unit loaded mass

Equation 9

$$\frac{\partial f}{\partial m} = -\frac{1}{2}\frac{f}{m}$$

For example, in the case of the translational frequency mode of the single-ended cantilever with an equivalent Young's modulus E and equivalent mass density ρ (Figure 11), the mass sensitivity is

Equation 10

$$\frac{\Delta f}{\Delta m} = -\frac{1}{2}\frac{E^{1/2}}{4\pi\rho^{3/2}}\frac{1}{WL^3}$$

where $k = \frac{EWH^3}{4L^3}$ and $m = \rho WHL$. Equation 10 clearly motivates approaches to increase in the mass sensitivity of cantilever sensors. The first approach is to reduce the size of the cantilever. When the dimensions of the cantilever shrink by a factor α, the mass sensitivity will be improved

by α^4. Another approach is to use lighter and stiffer materials instead of silicon in order to decrease the mass density and to increase the Young's modulus.

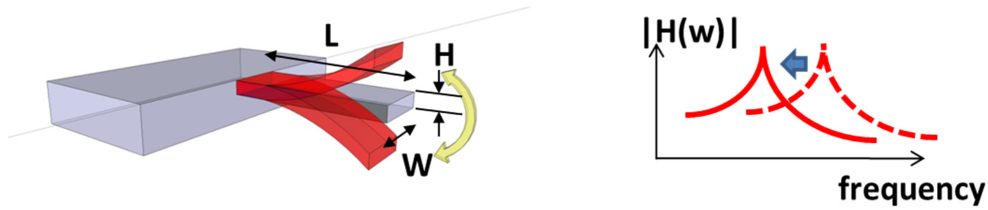

Figure 11. Schematic of cantilever in a translational mode (left) and resonant frequency shift caused from adsorption of mass (right).

2.2 Enhancement of sensitivity

2.2.1 Scaling of resonant sensors

A variety of methods to enhance the sensitivity of MEMS/NEMS resonant sensors have been explored, including scaling the devices to smaller size [29], treatments of sensor surfaces to improve quality factor [30], [31], modifications of readout schemes of sensors to measure more efficiently [32], and explorations of different resonator materials to obtain relevant properties such as hardness [33], [34].

As the aforementioned example of the simple cantilever, a straightforward approach to enhance the sensitivity is to miniaturize the dimensions of the sensor device. From Equation 9 the change of the resonant frequency is given by

Equation 11

$$\Delta f = -\frac{1}{2}\frac{\Delta m}{m}f_0$$

In general, when the dimensions are decreased, the resonant frequency increases and the mass decreases. Therefore, improved sensitivity (*i.e.*, larger fractional frequency shifts ($\Delta f / f_0$)) can be achieved by miniaturization due to scaling (*i.e.*, ratio of adsorbed mass to resonator mass (Δm / m)), which is the reason for scaling sensors toward nanometer dimensions. Substantial research has been undertaken in exploring the fundamental limits of resonant sensor performance, resulting in the ability to detect mass with zeptogram resolution [28] and quantum ground state [35]. However, ultrahigh vacuum (10^{-10} Torr) and/or extremely low temperatures (25 mK) are required for these fundamental studies in order to reduce noise, thereby improving resolution. While extremely useful for scientific study, these pressure and temperature conditions are not feasible for all situations, such as portable sensing systems. Besides, device scaling, which is beneficial for increased sensitivity, does create additional challenges. For example, ultra-small sensors suffer from increased accumulation time, which means that longer time is required for the analyte molecules to find the device.

Assuming a disk-shaped sensor detecting a hydrogen gas, the required accumulation time for the number of molecules attached to such device's surface is determined by

Equation 12

$$t = \frac{N}{4DN_A c_0 a}$$

where N is the number of molecules, D is the diffusion coefficient of molecules (in this case, hydrogen gas), N_A is the Avogadro's number, c_0 is the concentration of gas, and a is the radius of the sensor [36]. From the Equation 12, Figure 12 plots times required for sensors with radius ranging between 1 nm and 1 mm to accumulate different number of molecules. For example, a sensor with a radius of 10 nm needs about 1 hour for collecting molecules of 1 fg in 1 ppb (parts per billion) hydrogen environment.

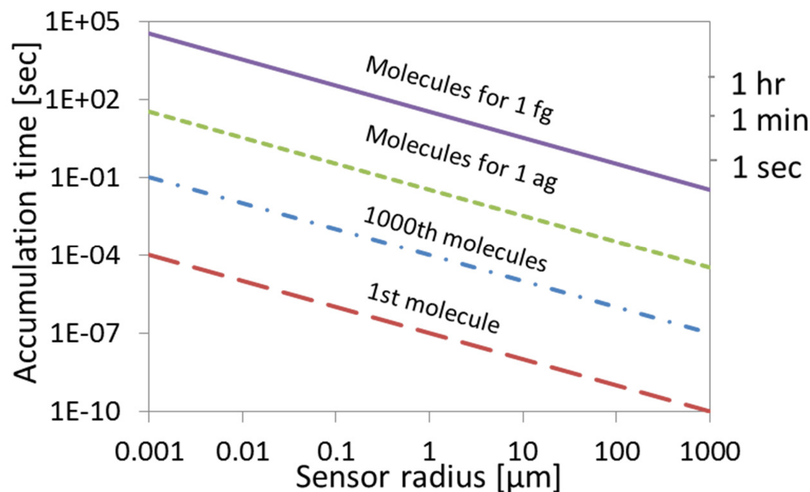

Figure 12. Required time for accumulating analyte molecules on a disk-shaped surface. Hydrogen gas molecules at 1 ppb are used as a model analyte for this example. For radii below 10 nm, more than one hour is necessary to detect 1 fg of analytes.

This problem is most pronounced for detection of low concentrations [36], unless specific methods such as highly controlled flux of analytes are applied [28]. If we consider an application of resonant sensors in liquid, the required time for detection becomes more critical, as the diffusion of analytes in liquid is far slower than in gas (typically, about four orders of magnitude) [37].

Furthermore, smaller devices have shown a trend of decreased quality factor. Figure 13 summarizes quality factor dependence on resonator sizes from the literature [27, 28, 38-49]. Given thermally driven random motion of the mechanical device, the minimum measurable frequency shift can be defined by [50]

Equation 13

$$\Delta f_{min} = \frac{1}{A}\sqrt{\frac{f_0 k_B T B}{kQ}}$$

where A is the amplitude of oscillation, k_B is the Boltzmann constant, T is the temperature, B is the bandwidth, k is the spring constant, and Q is the quality factor. Consequently, scaling of resonators may result in degradation of detectable frequency shift.

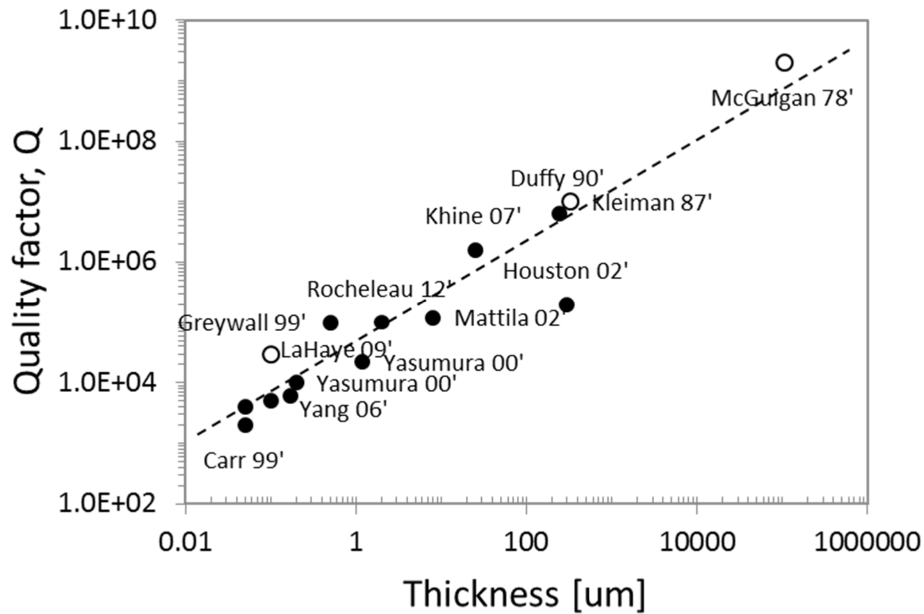

Figure 13. Quality factor vs. resonator size, where thickness is defined in the direction of the smallest dimension. The dashed line is a guide to the eye.

This work describes a sensing approach that provides the sensitivity of nanoscale devices through increasing the adsorbed mass (Δm) without sacrificing capture area, rather than through decreasing the resonator mass (m).

2.3 Surface enhanced resonant sensors

The goal of this work is to investigate porous materials to enhance the sensitivity and sensitivity of the resonant sensors for gas sensing applications using standard top-down microscale fabrication processes. The primary advantage of porous micromechanical resonators is an increased surface area for enhanced adsorption of a desired analyte without aforementioned issues due to scaling. This, in turn, leads to a larger resonant frequency shift and range of detectable mass shifts when compared with non-porous sensors. Three strategies will be introduced to achieve high sensitivity gas sensors;

(1) Integration of porous silicon into the silicon resonator structure,

(2) Functionalization of porous silicon surface through a receptor coating,

(3) Coupling of ultra-high porous materials (*i.e.*, zeolitic imidazolate frameworks (ZIFs)) to the silicon resonator. To couple the porous materials, two different approaches (*i.e.*, drop casting method and dielectrophoresis method) will be discussed.

Chapter 3 Porous silicon resonators

To offer impressive mass sensitivity, porous materials have been employed to increase the surface area of adsorption. Specifically, porous silicon has been proposed for many applications in sensor technology because of its unique material properties; optical [51], electrical [52], thermal [53], and structural [54]. Despite its large surface area and high chemical activity, approaches for mechanical devices of porous silicon have been limited by reduced stiffness and structural integrity. Therefore, porous materials have previously been limited for use as a coating on the surface of solid resonators to increase the surface area of adsorption [55, 56].

Both miniaturization and the addition of surface coatings can add additional complexity to fabrication, functionalization, and readout. However, nanoscale sensitivity from widely available microscale fabrication techniques can potentially be achieved in the approach described here. Porous silicon resonators are designed to provide increased sensitivity in resonant vapor sensors by making use of the increased surface area, where the resonant structure itself is fabricated from porous silicon. This work also focuses on resonators with target regions of porosity, called partially-porous silicon resonators. The partially-porous resonator, as illustrated in Figure 14, allows for the combination of surface enhancement from porous silicon and structural integrity from solid silicon, which is more robust during fabrication and easier to test. The nonporous silicon resonators of this work consist of whole polycrystalline silicon. For the fully-porous resonators, both center paddle and torsional beams consist of porous-etched silicon. For the partially-porous resonators, only the center paddle is porous-etched, and the torsional beams and the center paddle remain whole polycrystalline silicon in order to maintain their stiffness. The porous etch for the porous-etched device is not through the entire thickness of the device. As

described in the next section, the porous devices are composed of a layer of porous silicon on top of a layer of nonporous silicon.

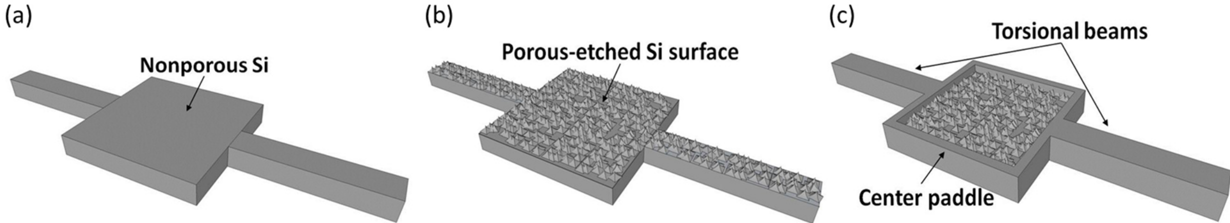

Figure 14. Schematic diagrams of (a) the nonporous silicon resonator, (b) the fully-porous silicon resonator, and (c) the partially-porous silicon resonator. The nonporous silicon resonator consists of whole polycrystalline silicon deposited with LPCVD. While both center paddle and torsional beams of the fully-porous structures consist of porous-etched silicon, for the partially-porous resonator, only the center paddle is porous-etched, and the torsional beams and edges of the center paddle remain nonporous-etched silicon in order to maintain their stiffness.

3.1 Design and Simulation

A torsional beam resonator is designed and simulated, as shown in Figure 15 and Figure 16 **(a)**. In a range from 100 kHz to 1 MHz, four modes of oscillation are observed. The first mode of oscillation, called translational or trampoline mode, corresponds to motion of the center paddle normal to the substrate surface, and the second mode, called torsional mode, corresponds to rotation of the center paddle about the beam axis.

In comparison with the translational mode, the torsional mode has the advantage of reduced air damping. While the translational mode induces a bending strain of the beams, the generated shear strain under the torsional motion is without volume tension or compression, resulting in suppressing volume change of the structure. Thereby, the torsional mode effectively restrains volume-change-induced thermoelastic dissipation [17, 57]. Furthermore, air damping [58, 59],

and clamping loss [60] of resonators in the torsional mode are depressed, contributing to a relatively high quality factor.

In addition, torsional mode is known to be relatively insensitive to mechanical nonlinear effects due to the increase in drive amplitude [61], because the nonlinear effect is induced by beam stretching.

Further, because of the fixed-fixed boundary conditions of this bridge structure, the resonator is relatively free from stiction during fabrication. The torsional resonant frequency of the double-ended beam structure is

Equation 14

$$f_0 = \frac{1}{2\pi}\sqrt{\frac{4E\,t_1^3\,w_1}{(1+\nu)\rho\,l_1\,l_2\,t_2\,w_2\,(t_2^2+\,w_2^2)}}$$

where E is the Young's modulus of the resonator, ν is the Poisson's ratio, and ρ is the density of the resonator [62, 63]. Figure 16 (a) shows the torsional beam resonator characterized by its dimensions, length l_1, l_2, thickness t_1, t_2, and width w_1, w_2 of the torsional beams and the center paddle, respectively.

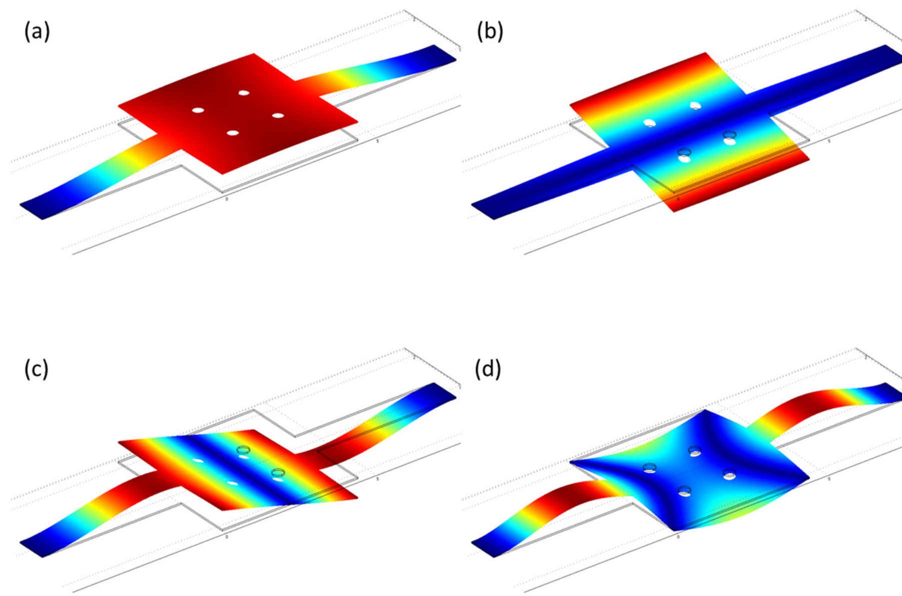

Figure 15. First four modes of oscillation of the designed resonator. (a) First mode corresponds to motion of a translational or trampoline mode. (b) Second mode corresponds to twisted motion of a torsional mode. (c) and (d) Additional modes are observed at higher frequencies. Note that change in color from blue to red illustrates greater displacement; however, amplitude of displacement of each mode is normalized to its maximum value.

Figure 17 (a) and (b) show the change of the resonant frequencies of the fully-porous and partially-porous silicon resonator for different etch times for different thickness of porous silicon layer as a function of Young's modulus of the top porous silicon layer of the two-layered structures. In the same figure the experimentally measured frequency values are plotted for each resonator type with the same dimensions, which are porous-etched for 10, 20 and 30 seconds.

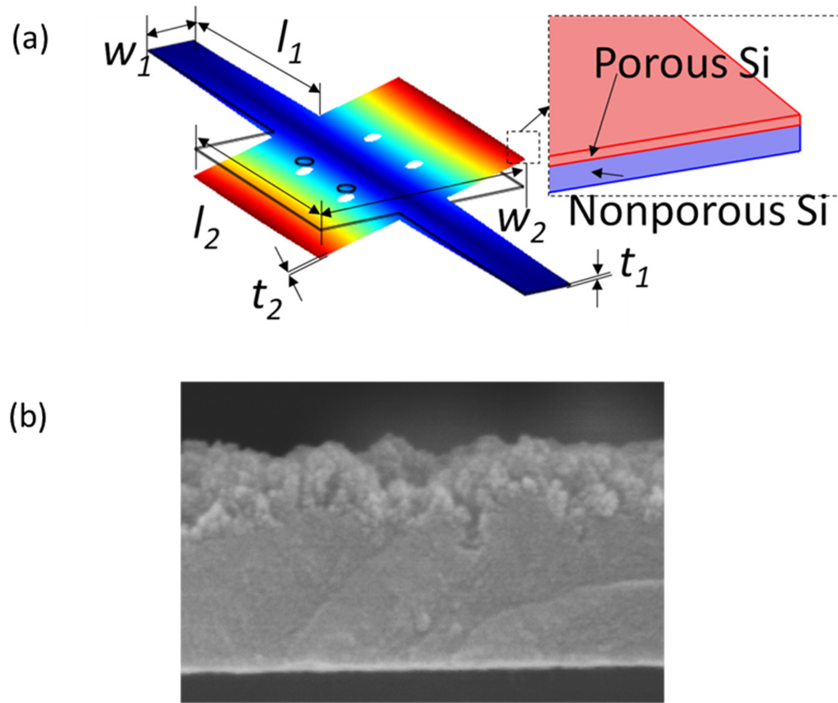

Figure 16. (a) Schematic diagram of resonator (l_1 = 45 µm, w_1 = 10 µm, l_2 = w_2 = 45 µm) with a composite nonporous and porous silicon layer of thickness t_b and t_t, respectively. (b) Fabricated porous silicon layer on the polysilicon in cross-section view.

The porous silicon has a different Young's modulus, Poisson's ratio, and density than nonporous silicon, depending on its porosity. Silicon that has been porous etched partway through its thickness can be modeled as a two-layered stack structure, which includes a bottom layer of nonporous silicon and a top layer of porous silicon, as illustrated in the inset and SEM images of Figure 16 [64]. As the Young's modulus for both the fully-porous and the partially-porous silicon resonators changes, the responses of the resonant frequencies are estimated by COMSOL Multiphysics 3.5 in order to assess unknown effective Young's modulus of the porous silicon layer for this work. The simulated structures consist of 45-µm-long, 10-µm-wide torsional

beams and 45-µm-long, 45-µm-wide center paddle with a composite nonporous and porous silicon layer. Table 3 compares the thicknesses of layers of each resonator type in Figure 16.

Table 3. Comparison of thickness for each type of resonator.

Type of resonator	Thickness of the center paddle		Thickness of the center paddle	
	t_b	t_t	t_b	t_t
Nonporous Si	470 nm	0 nm	470 nm	0 nm
Fully-porous Si	280 nm	110 nm	280 nm	110 nm
Partially-porous Si	470 nm	0 nm	280 nm	110 nm

As shown in Figure 16 (a), t_b and t_t are the thickness of nonporous and porous silicon layer, respectively.

In the modeling process, a two-layered stack structure is used, where the Young's modulus of the bottom nonporous polysilicon layer was experimentally fit to 135 GPa, and the Young's modulus for the top porous silicon layer is varied from 0.1 GPa to 100 GPa. The density of the porous silicon layer affects the Young's modulus, E_P, as described by

Equation 15

$$E_p = CE_B\rho_r^2$$

where C is a constant including the geometric scaling factor (C = 0.75), E_B is the Young's modulus of nonporous silicon, and ρ_r is the relative density of porous silicon [65]. Equation 15 is valid for $E_P < 100$ GPa, since $E_P > 100$ GPa makes ρ_r greater than unity. For the Young's modulus of 100 GPa where densities of both silicon layers are almost identical, differences between the resonant frequencies of each resonator are as a result of the decrease in thickness and density of top porous silicon layer by the porous-etching process. Decrease of the Young's

modulus of the top porous silicon results in a decrease of the resonant frequency of the fully-porous silicon resonator due to the decrease of the stiffness of the torsional beams. In contrast, for the partially-porous silicon resonator, the resonant frequency slightly increases due to the density reduction of the center paddle, because the partially-porous silicon resonator has nonporous silicon torsional beams. That is, mass is decreased for the partially-porous resonators while stiffness remains the same. From the plot, calculated resonant frequencies were compared with experimentally measured values of each resonator type. Therefore, the effective Young's modulus of the porous silicon layer used for these devices can be estimated at ~5 GPa by measuring each resonant frequency, where differences between measured and calculated values are within 7.8%, as presented in Figure 17. Reasons for discrepancy between prediction and experiment could include overall thickness variation of the resonators and depth variation of the etched pores.

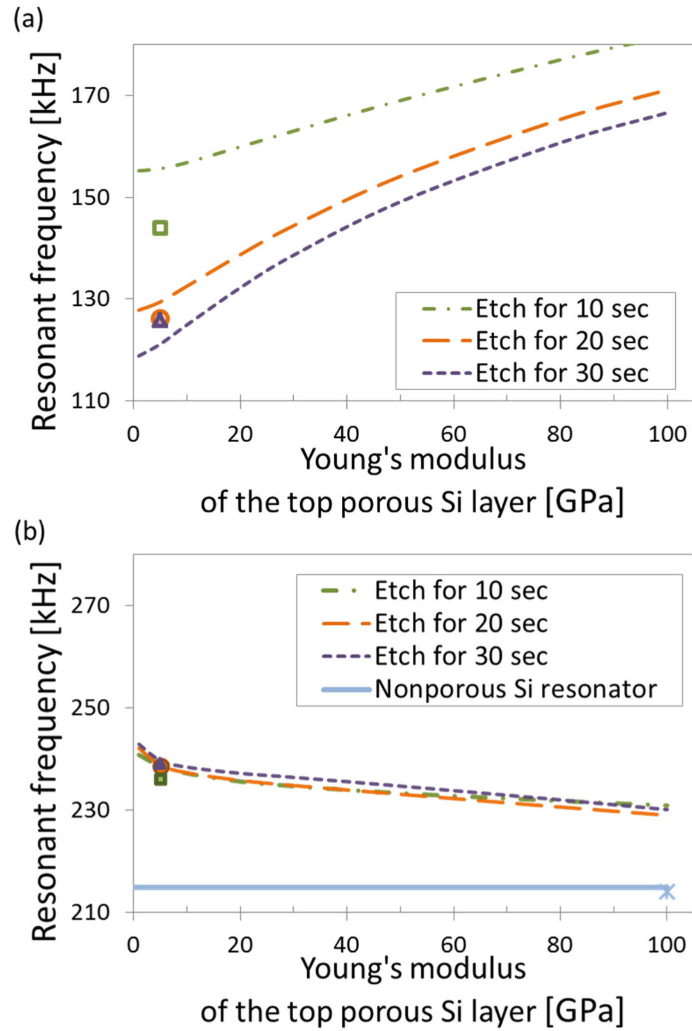

Figure 17. Simulated torsional resonant frequencies of resonators with different surfaces of the fully-porous (a) and the partially-porous silicon resonators (b), respectively. Resonant frequency is simulated for a range of Young's modulus values for the porous silicon. The Young's modulus is found by fitting the simulations to the experimentally measured resonant frequency. The Young's modulus of the top porous silicon layer of the two-layered structures ranges between 0.1 GPa and 100 GPa, while that of the bottom nonporous silicon layer remains as constant at 135 GPa. Square, circle, triangle, and star shaped points are measured average values for each resonator type etched for 10, 20 and 30 seconds, respectively. By comparing simulated resonant frequencies with experimentally measured values of each resonator type, the effective Young's modulus of the porous silicon layer used for these devices can be estimated at ~5 GPa.

3.2 Fabrication

Torsional beam resonant gas sensors are designed and fabricated using surface micromachining process as shown in Figure 18. The fabrication process is based on a process for the fully-porous silicon resonators [66]. The fully-porous, partially-porous, and nonporous silicon resonators are simultaneously fabricated on the same silicon wafer to quantify the sensitivity enhancement. The resonators are fabricated on 4-inch (100) silicon wafers as the substrates, followed by depositions of 5.5-μm-thick silicon dioxide (PECVD, Plasmatherm 790) serving as a sacrificial layer and 470-nm-thick polysilicon by LPCVD (Tystar Titan II furnace). The structures of the resonators are then defined by photolithography (KarlSuss MA-6 aligner) and deep reactive ion etching (SLR 770 ICP). Next, standard photoresist (AZ 5214) is spin coated and patterned to serve as a mask for porous etching.

Electroless metal-assisted etching of the silicon surface is used to porosify the silicon structures [67, 68] as described in the following sentences. The wafer is dipped in an Au (gold) coating solution, which is made by dissolving 0.01M $KAuCl_3$ (98% Aldrich) in a 10 wt% HF solution, for 10 seconds to deposit Au clusters selectively onto the exposed silicon. As illustrated in Figure 19, on the upper surface of Au cluster a cathode reaction happens with hydroperoxide, and on the bottom surface an anode reaction happens with silicon and HF. These reactions supply hole injections into silicon and etched silicon molecules underneath Au clusters, as displayed in Table 4. Thin Au clusters served as chemical catalysts for silicon etching. Therefore, silicon molecules underneath Au clusters are etched away in the etching solution (49.9% HF, 30% H_2O_2, and H_2O with a volume ratio of 1:5:10) for 10-30 seconds depending on desired level of porosification. The remaining Au clusters are subsequently removed by immersing the samples in Au etchant (651818, Sigma Aldrich) for 15 seconds, followed by removal of the photoresist

mask. The electroless metal-assisted porous etching steps are omitted for the nonporous silicon resonators and the second photolithography for partial opening of the center paddle is omitted for the fully-porous silicon resonators.

Finally, silicon dioxide sacrificial layers of both nonporous silicon and porous silicon resonators are removed by 49% HF solution for 150 seconds and rinsed by deionized water, followed by drying using a critical point dryer (CPD, Automegasamdri- 915B) to prevent stiction.

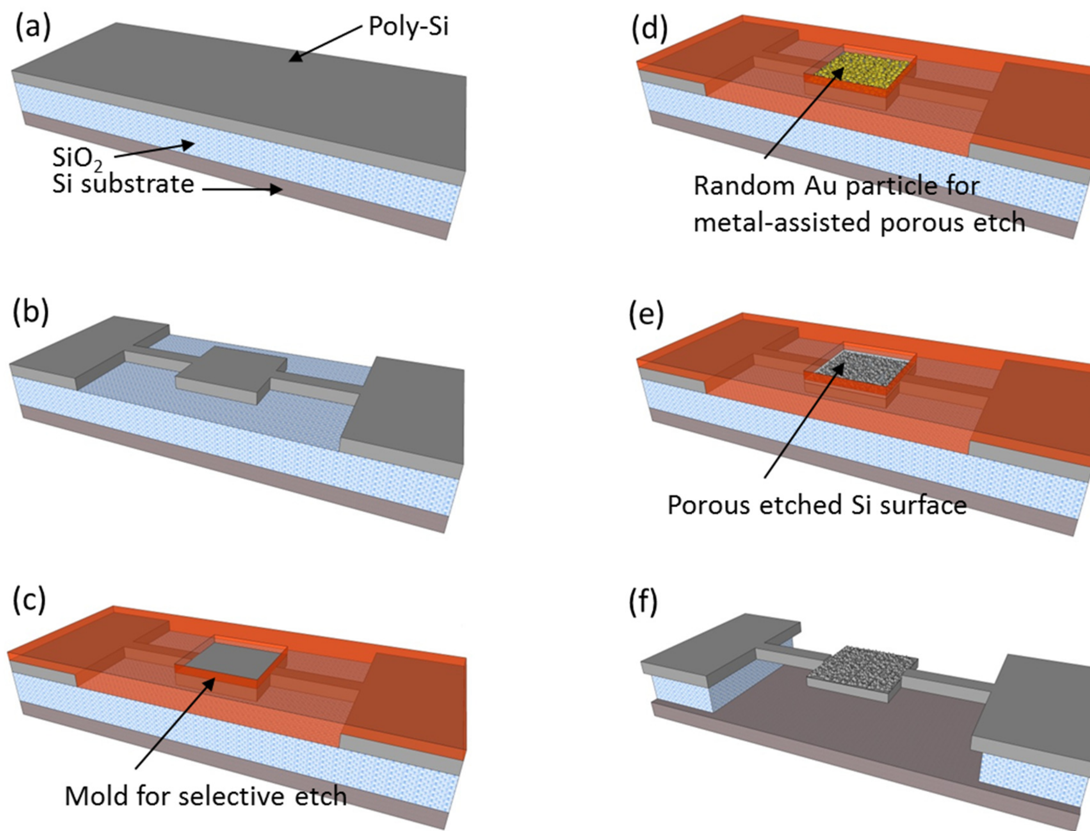

Figure 18. Fabrication process for partially-porous silicon resonators. (a) Deposition of SiO_2 and polysilicon by LPCVD. (b) Photolithography and polysilicon etching by DRIE for defining body of the resonator. (c) Photolithography for opening of porous region. (d) Au catalyst layer deposition by E-beam evaporator. (e) Porous silicon etching and Au layer removal. (f) Sacrificial layer etching and drying with CPD. Step (c) is omitted for fully-porous silicon resonators.

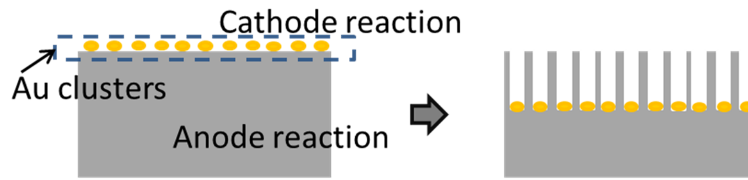

Figure 19. Schematic of the electroless metal-assisted porous etch process.

Table 4. Electrochemical reaction of the metal-assisted porous etch

Cathode reaction	$H_2O_2 + 2H^+ \rightarrow 2H_2O + 2h^+$ $2H^+ + 2e^- \rightarrow H_2$
Anode reaction	$Si + 2e^- \rightarrow H_2$ $SiF_4 + 2HF \rightarrow H_2SiF_4$

Figure 20 shows the change of roughness from the porous etching process, which allows the porous silicon resonator to have a larger surface area than the nonporous silicon resonator of the same dimensions. It is observed that the nonporous silicon film initially has a 30 nm-deep hemispherical grain region, whereas the porous silicon film has nanoscale pores 70 nm, 110 nm, and 120 nm into the surface for different porous silicon etch times, shown in Figure 21. Further, porous silicon etching makes torsional beams pliable, causing stiction during release of some of the fully-porous resonators. The morphology of the porous-etched silicon surface is observed with AFM (atomic force microscopy), as presented in Figure 22. With scan range of 5×5 μm^2, surface area from the images of the nonporous silicon and the porous silicon are 28.5 μm^2 and 158 μm^2, respectively.

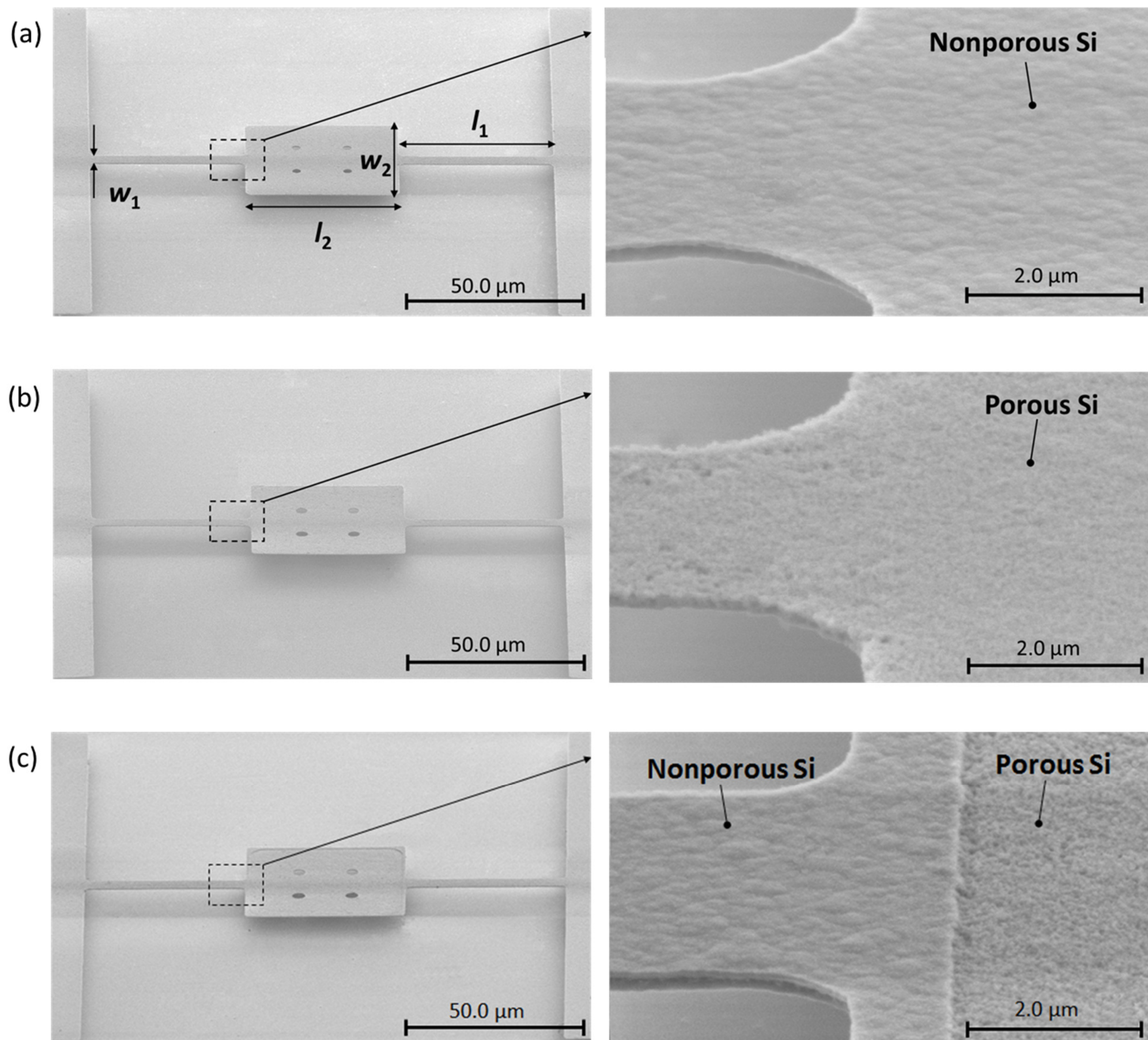

Figure 20. SEM images showing l_1 = 45 µm, w_1 = 5 µm, and $l_2 = w_2$ = 45 µm resonators. (a) Nonporous silicon resonator. (b) Fully-porous silicon resonator (c) Partially-porous silicon resonator. Both center paddle and torsional beams of nonporous and fully-porous silicon resonators consist of LPCVD-deposited silicon and porous-etched silicon, respectively. For the partially-porous resonator, only the center paddle is porous-etched.

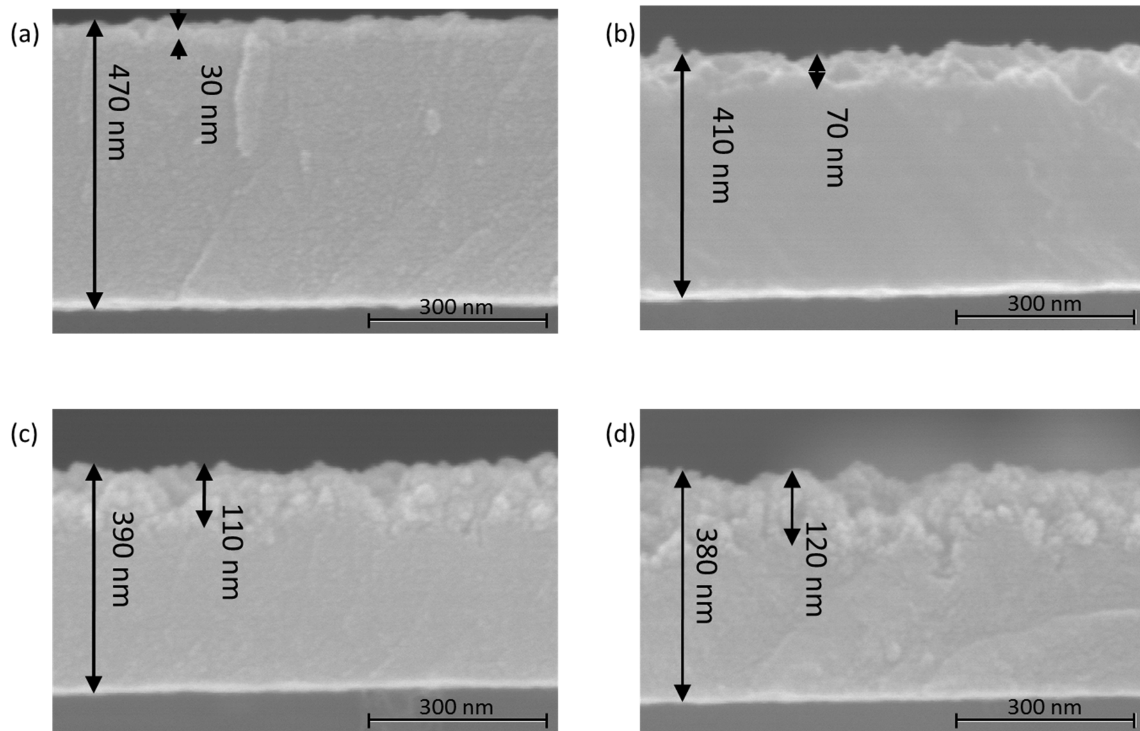

Figure 21. Cross sectional SEM images of porous-etched silicon layer for different etch times, t_{etch}: (a) 0 second (*i.e.* nonporous silicon), (b) 10 seconds, (c) 20 seconds, (d) 30 seconds.

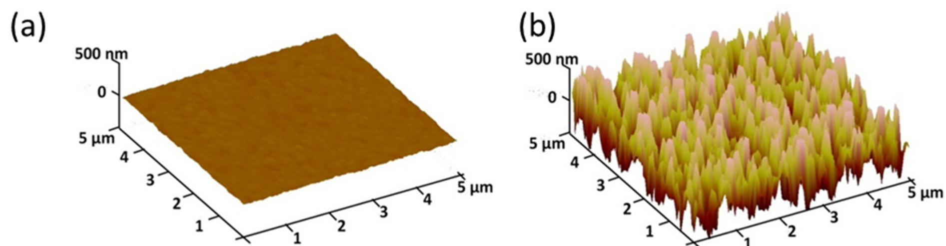

Figure 22. AFM images of (a) the nonporous silicon and (b) the porous silicon. The porous silicon is etched for 30 seconds. The values of the RMS roughness are 7.8 nm and 264 nm, respectively.

3.3 Experimental results

3.3.1 Experimental Setup

The frequency spectra of the resonant gas sensors are measured with a test setup that consists of a Laser Doppler vibrometer (LDV, Polytec OFV-5000), a custom-built vacuum chamber with roughing and turbo pumps, a microscope unit (Mitutoyo FS70), and a network analyzer (HP 8753D), as shown in Figure 23. To induce mechanical resonance, the device is mounted on a piezoelectric actuator (Thorlabs AE0203D08F), which is controlled by the stimulus signal of the network analyzer. Measurements are performed in a vacuum chamber in order to avoid energy losses by air damping and are at room temperature. A stainless-steel reservoir that is connected with the vacuum chamber via a metering valve is used to control gas flow. Resonator vibration is differentially detected using two laser signals, one focused on the resonator and the other focused on the anchor of the resonator. The reflected beams are converted to an electrical signal by the LDV controller, and the network analyzer recorded the resonant frequency of the resonator mass sensor. Silicon resonators can detect IPA (isopropyl alcohol) vapor since IPA adsorbs to silicon surfaces via oxygen atoms [69].

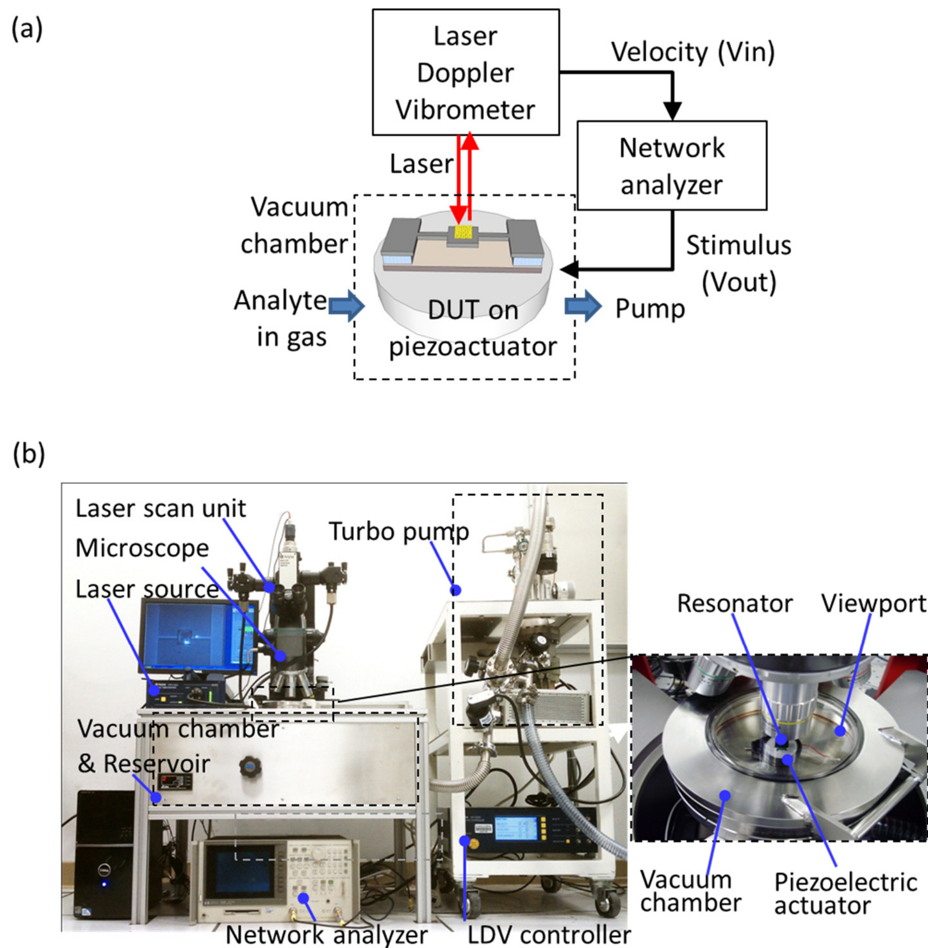

Figure 23. (a) Schematic diagram. (b) Photos of the experimental setup for mechanical actuation and readout by using a Laser Doppler vibrometer.

The first two modes of oscillation for the resonator are a translational mode, corresponding to motion of a center paddle normal to a substrate, and a torsional mode, corresponding to rotation of the center paddle around the axis of the torsional beams. The LDV system measures the difference of motion at different two positions. One reflected beam for reference is positioned on the nonmoving pad structure, and the other is on the center of the paddle or edge to see the translational mode or torsional mode. After identifying frequency of each mode, one can measure each resonant frequency mode on most suitable positions for reflecting beams in order

to maximize the height difference of the moving structure (and thus higher detection signal of the LDV). As presented in Figure 24, experimental results show the torsional mode has greater peaks than the translational mode and the highest amplitude of the signal when the beams are shined onto both sides of edge of the center paddle.

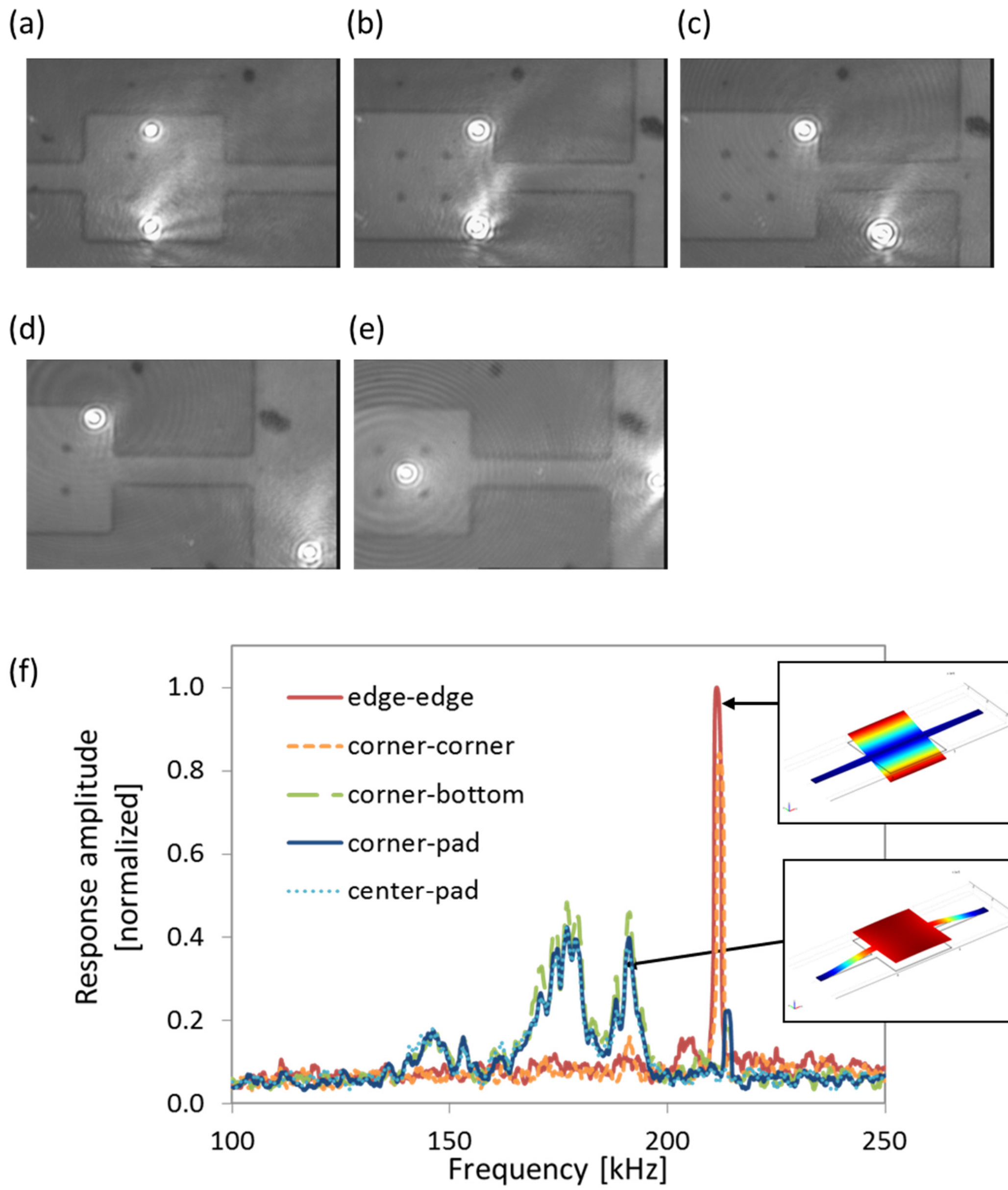

Figure 24. (a)-(e) Comparison of positions of laser beams of the LDV system. The beams are on edge-edge, corner-corner, corner-bottom, corner-pad, and center-pad in order. (f) The measured amplitudes of each resonance mode depend on the positions of two beams.

3.3.2 Changes in resonator frequency and Q by porosification

Air damping is frequently a dominant energy loss mechanism in sub-GHz devices that are not operated under high vacuum [70]. Since operating pressure affects air damping and is dependent on vapor concentration, it is necessary to understand the dependence of resonator quality factor on pressure. Figure 25 shows changes of quality factor for resonators as a function of pressure. The quality factors of each type of resonator are a strong function of pressure down to 0.1 Torr. The quality factor, Q, and dependence on pressure, P for the nonporous, fully-porous, and partially-porous silicon resonators are of the form $Q = 129/P^{0.953}$, $Q = 168/P^{0.808}$, and $Q = 135/P^{0.823}$, respectively. The relationship between quality factor and pressure for the simplest case has a relationship of the form $Q \propto 1/P$ [71]. Below 0.1 Torr, the quality factors are determined by damping mechanisms other than air damping. As a result, the pressure range where the quality factor is limited by air damping is roughly independent of the resonators' porosity.

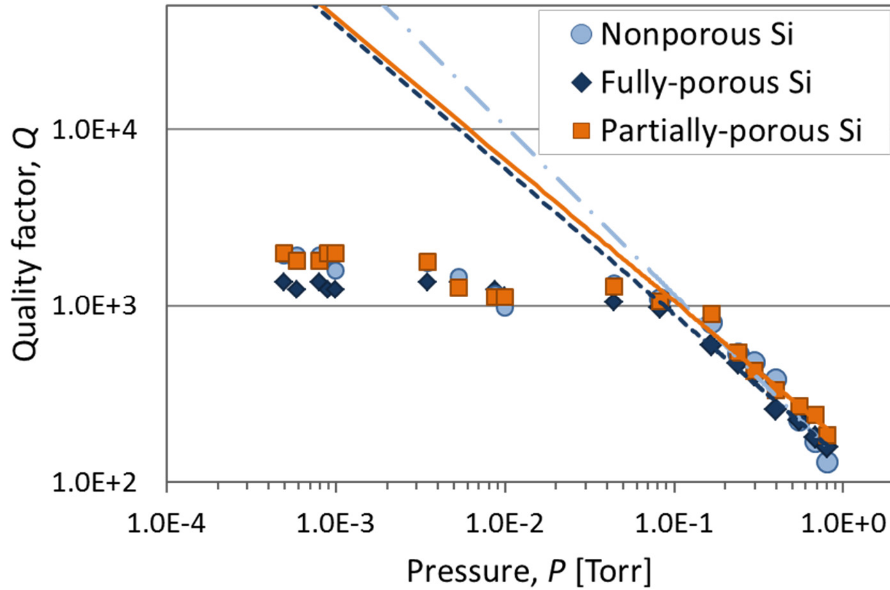

Figure 25. Measured quality factors of resonators. Above 0.1 Torr, data of the nonporous, fully-porous, and partially-porous silicon resonator are described by $Q = 129/P^{0.953}$ (dash dot line), $Q = 168/P^{0.808}$ (dashed line) and $Q = 135/P^{0.823}$ (solid line), respectively. Below that pressure, another energy loss mechanism limits the quality factor.

3.3.3 Vapor detection

Figure 26 contains characteristic frequency spectra showing shifts in the torsional mode resonant frequency under 5000 ppm of IPA (isopropyl alcohol) vapor. The resonant frequency shift is measured with respect to the partial pressure of IPA, which is normalized with respect to one atmosphere to provide units of ppm. The porous silicon resonator displays a frequency shift significantly greater than that of the nonporous silicon resonator.

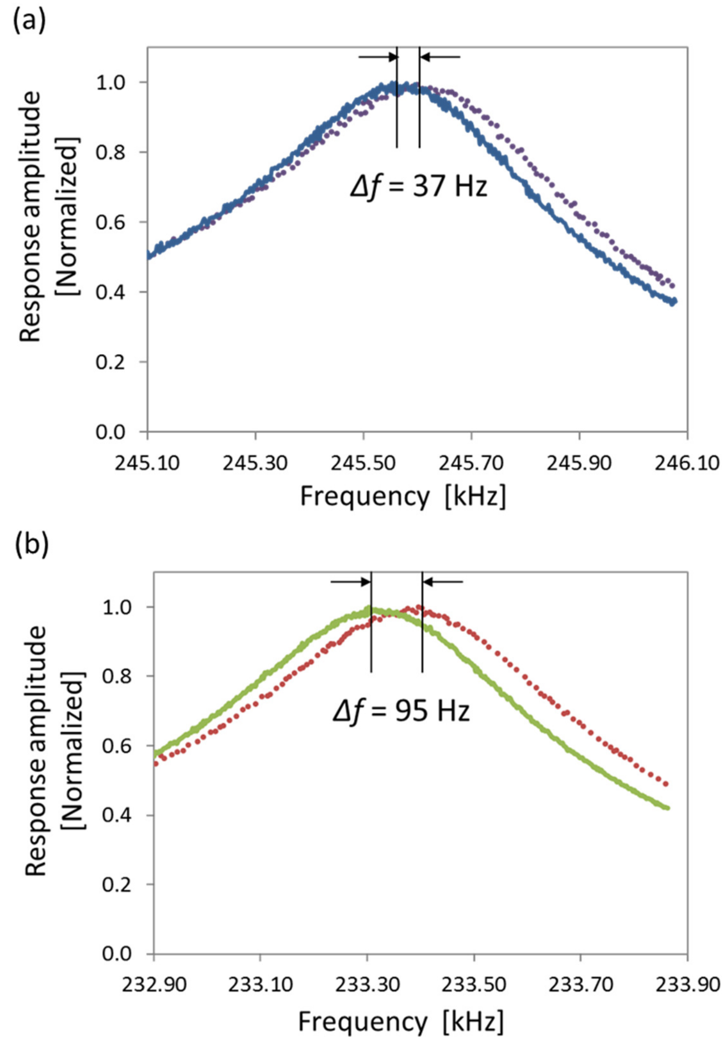

Figure 26. Measured frequency spectra of (a) nonporous and (b) fully porous silicon resonators with no IPA (dashed line) and 5000 ppm of IPA (solid line).

Resonators with l_1 = 45 µm, w_1 = 10 µm, l_2 = w_2 = 45 µm, and t_{etch} = 20 seconds have been utilized to investigate how resonant frequency shifts are affected when the resonators are porosified. Figure 27 plots the different responses of the non-porous, fully-porous, and partially-porous silicon resonators by the relative resonant frequency shift (the resonant frequency shift, Δf is divided by the resonant frequency, f_0) versus the IPA concentration. The fully-porous silicon

resonators show higher frequency shift ranging between 99% and 14% for different gas concentrations of 8500 ppm and 5000 ppm compared to the nonporous silicon resonators, whereas frequency shift of the partially-porous silicon resonator is enhanced ranging between 60% and 4%. Thus, by calculating slope of the normalized frequency shifts, the resonator sensitivity for fully-porous resonators and partially-porous resonators is improved up to 261% and 165%, respectively, as compared to nonporous silicon resonators. The higher sensitivity of fully-porous resonators as compared to partially-porous resonators could result from several causes:

1) Reduction of the surface area of the partially-porous silicon resonator due to nonporous silicon torsional beams decreases the vapor mass adsorbed on the resonator 2) The initial mass of the partially-porous silicon resonator is larger than the fully-porous resonator, which is relevant because sensitivity is dependent upon fractional mass change of adsorbed species.

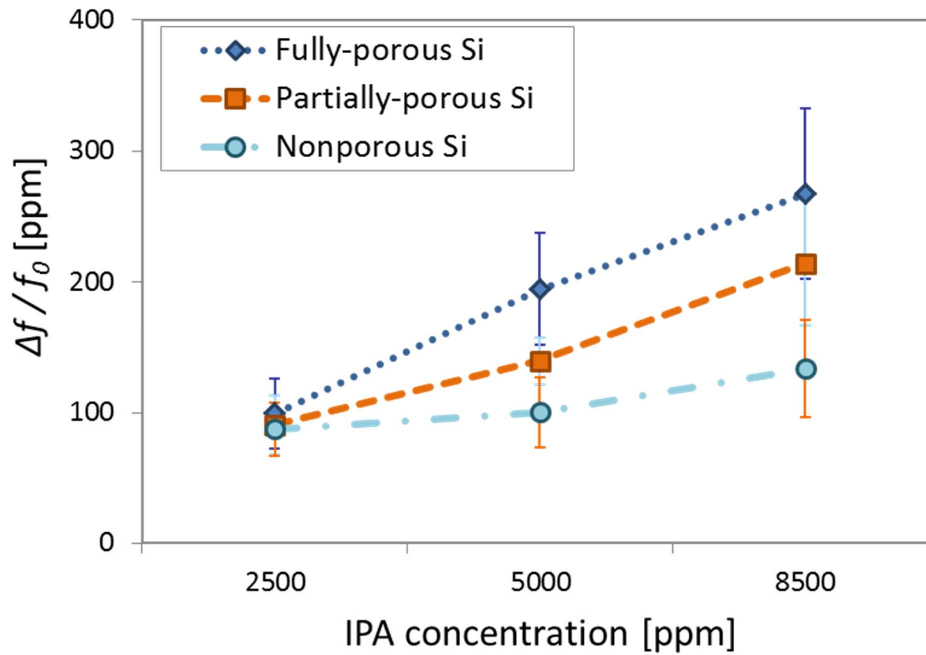

Figure 27. A comparison of relative frequency shifts vs. gas concentration. The error bars indicate the standard deviation in the data, which comprised five measurements at five minute intervals for each concentration.

The relative performances comparing the nonporous silicon resonator are summarized in Table 5 [72, 73]. It is demonstrated that the resolution of the partially-porous and fully-porous silicon resonator was reduced by 44% and 59%, respectively, as compared to the nonporous resonators. Since the partially-porous silicon resonator has enhanced quality factor as compared to the fully-porous resonator, its resolution should be enhanced [74]. Moreover, the weakened torsional beams of the fully-porous silicon structure limit further porosification for larger surface area, whereas the porous paddle of the partially-porous silicon structure can be porous-etched more deeply in order to further enhance the sensitivity.

Table 5. Relative performances for each type of resonator.

Type of resonator	Sensitivity [a]	Noise [b]	Resolution [c]
Nonporous Si	S_0	$\frac{1}{Q_0} = N_0$	R_0
Fully-porous Si	$3.61\ S_0$	$\frac{1}{0.46\ Q_0} = 2.17\ N_0$	$0.59\ R_0$
Partially-porous Si	$2.65\ S_0$	$\frac{1}{0.85\ Q_0} = 1.17\ N_0$	$0.44\ S_0$

Each performance parameter is shown in relative values in terms of the nonporous silicon resonator.

[a] $\text{Sensitivity} = \frac{\text{Output of sensor change}}{\text{Input change of measurand}}$

[b] $\text{Noise} \propto \frac{1}{\text{Quality factor}}$ [26]

[c] $\text{Resolution} \propto \frac{\text{Noise}}{\text{Sensitivity}}$

Chapter 4 Receptor-coated porous silicon resonators

Surface treatments used in functionalization of sensors provide the devices further capability for sensing. To detect chemicals, cantilevers are typically functionalized with receptor materials that either specifically interact with the desired analyte or show a higher affinity response. For example, gold coated microcantilevers have been used to detect mercury vapor [75] and humidity sensors have been demonstrated with gelatin-coated cantilevers [76]. Also, various polymer films adsorb volatile organic compounds [77] or chemicals required for realizing an artificial nose [78].

This chapter focuses on silicon resonators with targeted regions of porosity and functionalization, combining the advantages of increased surface area of porous silicon with the structural strength of nonporous silicon and further adsorption by chemical treatment.

4.1 Fabrication of receptor-coated porous silicon resonators

The nonporous silicon resonator consists of whole polycrystalline silicon. Regions of the nonporous resonators can be converted to porous by electroless metal-assisted etching. Fabrication of each type of resonator using surface micromachining process is presented in Figure 28. As described in section 3.2, porous and nonporous silicon resonators are fabricated on the same wafer in order to quantify the enhancement in sensitivity. The resonators are fabricated on 4-inch (100) silicon wafers as the substrates, followed by depositions of 5.5-µm-thick silicon dioxide serving as a sacrificial layer and 470-nm-thick polycrystalline silicon by LPCVD. After the resonator structures are defined by photolithography and deep reactive ion etched, a standard photoresist (AZ 5214) is patterned to serve as a mask for selective porous etching. The surface is made porous using an electroless metal-assisted etching technique, which involves randomly depositing gold clusters as chemical catalysts [67].

Next, 25 nm-thick chromium and gold films are deposited for adhesion of the receptor coating. The electroless metal-assisted porous etching steps are omitted for the nonporous silicon resonators and the second photolithography for partial opening of the center paddle is omitted for fully-porous silicon resonators. Followed by liftoff of metal layers and sacrificial layer etch, the samples are coated with receptor solution. 4-MBA (4-mercaptobenzoic acid) is used as a receptor material since it interacts with alcohol through hydrogen bonds [79]. Fabricated partially-porous silicon resonator with receptor coating is shown in Figure 29.

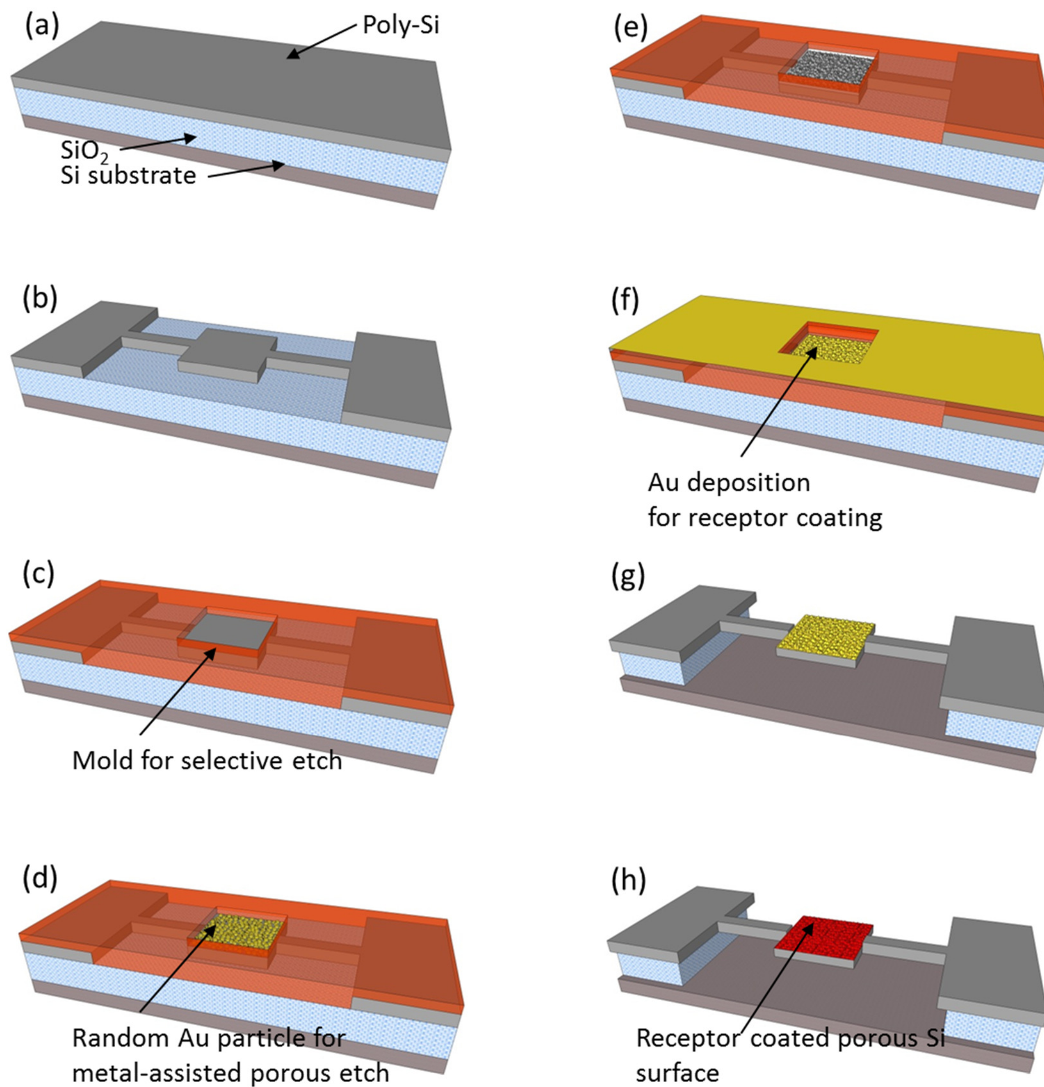

Figure 28. Fabrication process for partially-porous silicon resonators. (a) Deposition of SiO_2 and polycrystalline silicon by LPCVD. (b) Photolithography and polycrystalline silicon etching by DRIE for defining body of the resonator. (c) Photolithography for opening of selective porous region. (d) Random gold cluster coating. (e) Porous silicon etching and gold layer removal. (f) Cr/Au deposition as linker of receptor material. (g) Liftoff of Cr/Au. (h) Sacrificial layer etching and receptor coating.

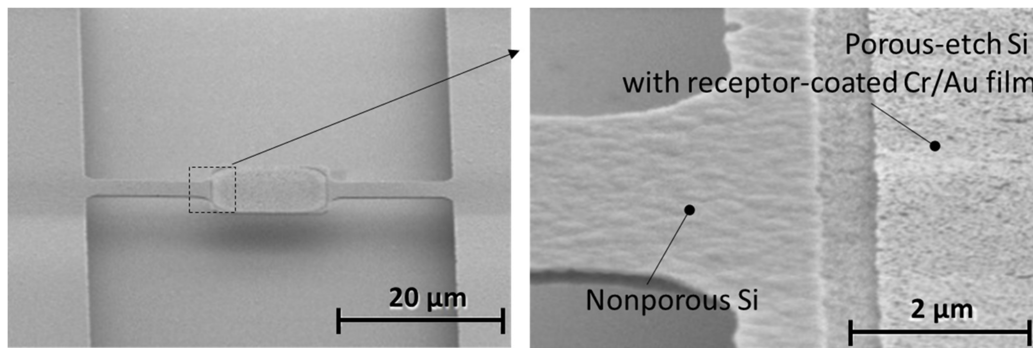

Figure 29. SEM images of the partially-porous silicon resonator with receptor-coated Cr/Au film. Only the center paddle is porous-etched. The porous etched region is coated with Cr/Au film and 4-MBA as receptor material.

4.2 Experimental results

Figure 30 compares the dependence of resonant frequency and quality factor on the etch time for porosification (0-30 seconds) for resonators with different lengths of torsional beams (45-120 µm). As porous etch times increase, the resonant frequencies of fully-porous and partially-porous silicon structures have opposite tendencies because the partial porous structures primarily have a decrease in mass, whereas the fully-porous structures also have a large decrease in stiffness due to the porous beams. Partially-porous silicon structures with metal and receptor coating have the same trends with uncoated partially-porous silicon structures except having a frequency offset due to additional coating of metal and receptor. The quality factor gets decreased gradually as surface-to-volume ratio of resonators increases due to further porous etch. Figure 30 (b) illustrates that the quality factors of the partially-porous structures are generally improved by employing nonporous silicon torsional beams.

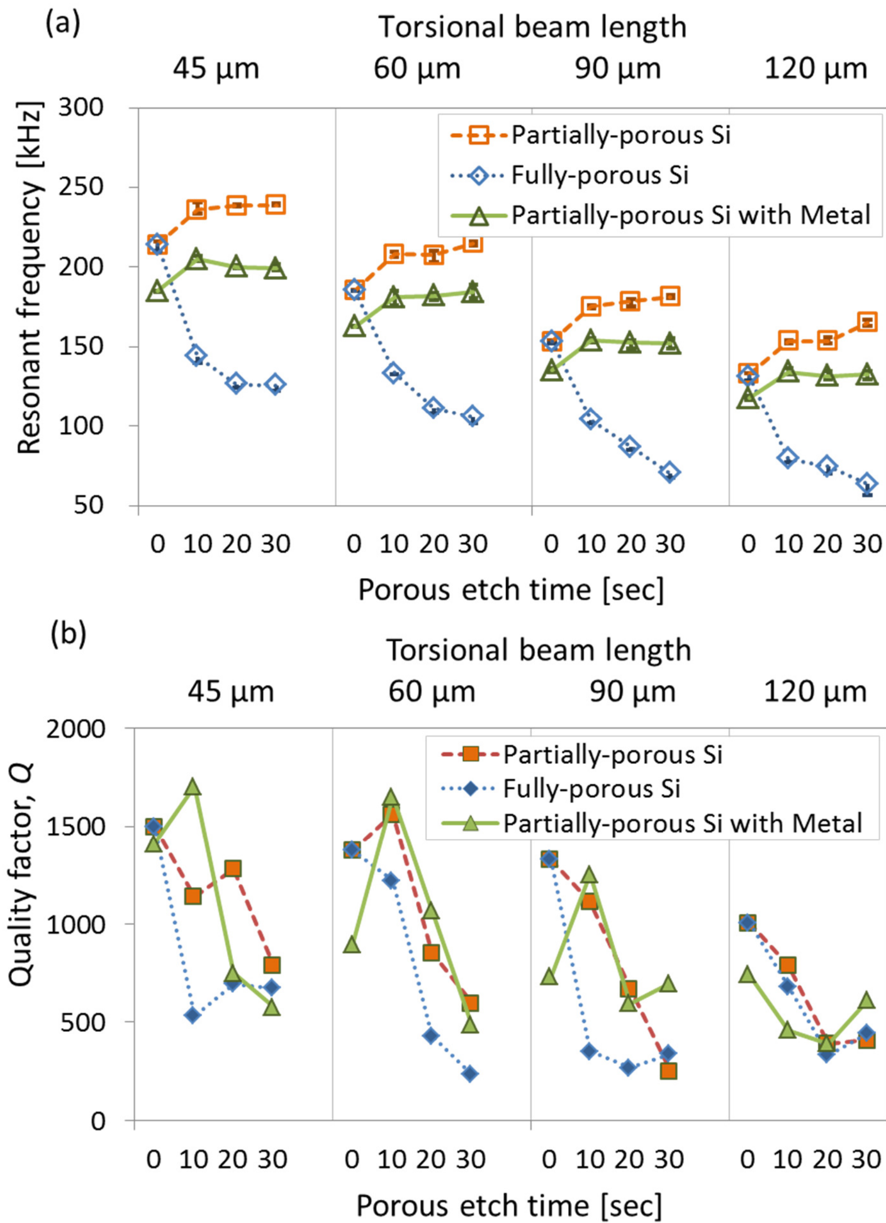

Figure 30. Measured (a) resonant frequencies and (b) quality factors for different etch times and torsional beam lengths. The values of zero–second-etched condition indicate the case of nonporous silicon resonators.

Figure 31 illustrates the different responses of each type of structure by the relative resonant frequency shift from different IPA concentration. The resonator sensitivities are calculated from

the slopes of the normalized frequency shifts. The relative sensitivities of partially-porous, fully-porous, and receptor coated partially-porous structure are improved to 261%, 165%, and 654%, respectively. The partially-porous structures have a slightly smaller improvement in sensitivity when compared to the fully-porous structure because the fully-porous structures have higher surface area. Another reason is the initial mass of the partially-porous silicon resonator is greater than the fully-porous resonator, which is relevant because sensitivity is dependent upon fractional mass change of adsorbed gas molecules.

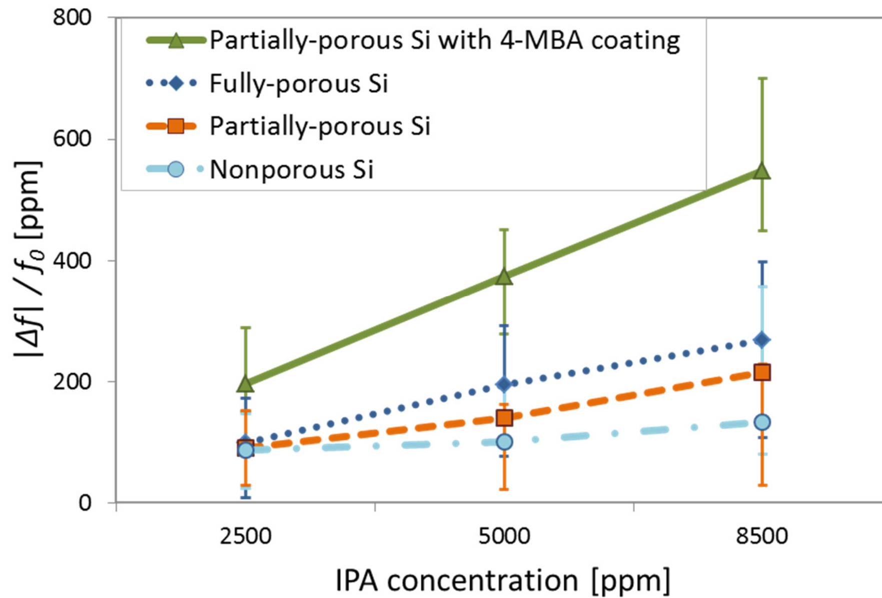

Figure 31. A comparison of relative frequency shifts vs. gas concentration. The error bars indicate the standard deviation in the data, which comprised five measurements at five-minute intervals for each concentration.

Relative resolution is inversely proportional to the product of sensitivity and quality factor [26, 74], with low resolution being preferred. As shown in Table 6, it is demonstrated that the resolution was reduced to 44% of nonporous silicon structure in the case of the partially-porous

silicon structure, and 26% for the receptor-coated partially-porous silicon structure. In addition, torsional beams of the fully-porous silicon structure which are already weakened by porosification limit further porosification for larger surface area, whereas porous paddle of the partially-porous silicon structure can be porous-etched more deeply in order to further enhance the sensitivity.

Therefore, enhanced chemical vapor sensitivity using partially porous functionalized silicon resonators by using a microscale device with nanoscale features is demonstrated. By keeping critical parts of the resonator non-porous, the mechanical stability of these resonators is improved over their fully porous counterparts. The combination of porous surface and functionalization for resonant sensing can be extended to many other adsorption-based sensing applications.

Table 6. Relative performance for each type of resonator.

Type of resonator	Sensitivity [a]	Noise [b]	Resolution [c]
Nonporous Si	S_0	$\frac{1}{Q_0} = N_0$	R_0
Fully-porous Si	$3.61\ S_0$	$\frac{1}{0.46\ Q_0} = 2.17\ N_0$	$0.59\ R_0$
Partially-porous Si	$2.65\ S_0$	$\frac{1}{0.85\ Q_0} = 1.17\ N_0$	$0.44\ R_0$
Partially-porous Si with 4-MBA coating	$7.54\ S_0$	$\frac{1}{0.49\ Q_0} = 2.04\ N_0$	$0.26\ R_0$

Each performance parameter is shown in relative values in terms of the nonporous silicon resonator.

[a] $\text{Sensitivity} = \frac{\text{Output of sensor change}}{\text{Input change of measurand}}$

[b] $\text{Noise} \propto \frac{1}{\text{Quality factor}}$ [26]

[c] $\text{Resolution} \propto \frac{\text{Noise}}{\text{Sensitivity}}$

Chapter 5 ZIF-agglomerated resonant gas sensor using drop casting manipulation

It has been demonstrated that various functionalization methods [80, 81] or porous treatment [56, 82] of the sensor surface enable the sensors to have better sensitivity arising from more adsorption. In this chapter, the approach uses highly porous nanoparticles, ZIFs (zeolitic imidazolate frameworks) to provide both the sensitivity of nanoscale devices with the capture area of microscale devices and the selectivity to desired analytes, which is noteworthy because ZIFs have more surface area than any material previously used for resonant sensing [83].

5.1 ZIF (zeolitic imidazolate frameworks)

ZIFs are a new class of three-dimensional crystalline structures synthesized from transition metals bridged by imidazolate. ZIFs are receiving attention for gas storage due to their ultra-high surface area, and they show promise in filtering applications due to their tailorable nanoporosity [84, 85]. These properties of high surface area and tailorable nanoporosity (and therefore selectivity) are also attractive for various sensing methodologies, such as detecting changes of impedance [86], refractive index [87, 88], strain [89], and surface acoustic wave [90], as displayed in Figure 32. Previous research has investigated the potential for sensitivity enhancement with various porous material coatings on resonant sensors [56]. However, the work described here marks the first demonstration of resonant sensors using ZIFs, which is noteworthy because ZIFs have higher surface area than any material previously used for resonant sensing. As an example, ZIF-69, has a high Langmuir surface area of 1070 m^2/g and a high affinity for CO_2, enabling superior adsorption and selectivity properties [83, 91].

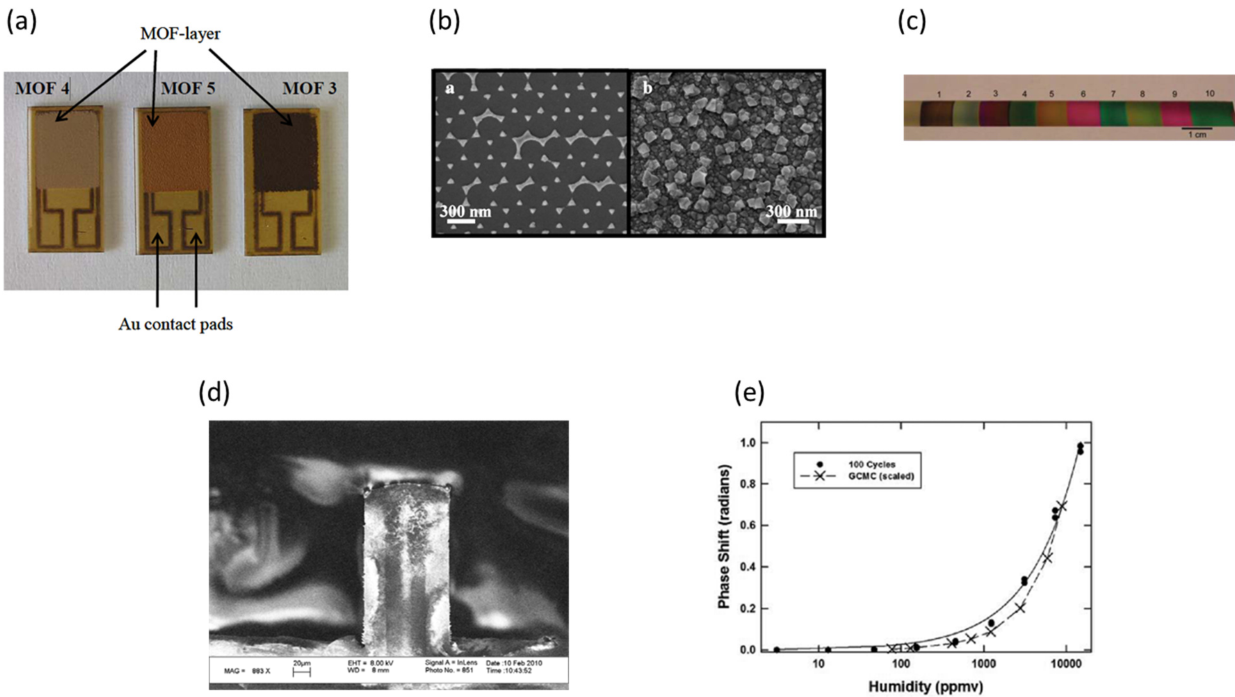

Figure 32. Various MOF (metal organic framework) sensors using the MOF's property of high surface area. Sensor are based on change of (a) impedance [86], (b) and (c) refractive index [87, 88], (d) strain [89], and surface acoustic wave [90].

5.2 Fabrication process for integrating nanoparticles with released structures

To detect chemical or biological entities, devices can be functionalized with appropriate chemical treatments that enhance sensitivity, specificity, or both. These chemical treatments typically require contact of the MEMS/NEMS devices with liquids, which creates challenges in designing process flows. Specifically, MEMS/NEMS devices are typically released very late in the process flow because the devices are fragile and susceptible to stiction after release. However, many functional coatings will not survive the high temperature processing or aggressive chemical etches that are typical in process flows. Thus, an inherent conflict exists between the fragility of released structures and the inability of some functional coatings to survive aggressive

process steps. From this conflict a need arises that both allows for the survival of functional coatings and prevents stiction of the devices during the wet processing commonly used to apply these coatings.

Stiction, or adhesion, has been one of the most challenging problems for MEMS/NEMS yield and reliability [92, 93]. Common methods to avoid stiction during release include HF vapor etching [94] and supercritical point drying [95]. Another method is sublimation drying, where a rinsing liquid (e.g., p-dichlorobenzene (p-DCB)) is solidified and sublimated to avoid formation of a liquid-gas interface, thus eliminating capillary forces that can cause adhesion between released structures and the substrate [96].

This chapter proposes and demonstrates a fabrication technique that circumvents the issues faced by conventional liquid-based functionalization methods, namely stiction, and incompatibility with standard microfabrication processes. The technique involves sublimation drying combined with photoresist reflow replacement of sublimated p-DCB. The proposed technique is applicable to a wide range of coatings and particles, and it is demonstrated here via coupling of nanoparticles to the surface of a MEMS resonant sensor.

5.3 Device design

The goal of this work is to investigate porous materials to enhance the sensitivity and sensitivity of the resonant sensors for gas sensing applications. As illustrated in Figure 33, selected regions of the resonator can be functionalized with nanoparticles to increase the adsorptive surface area.

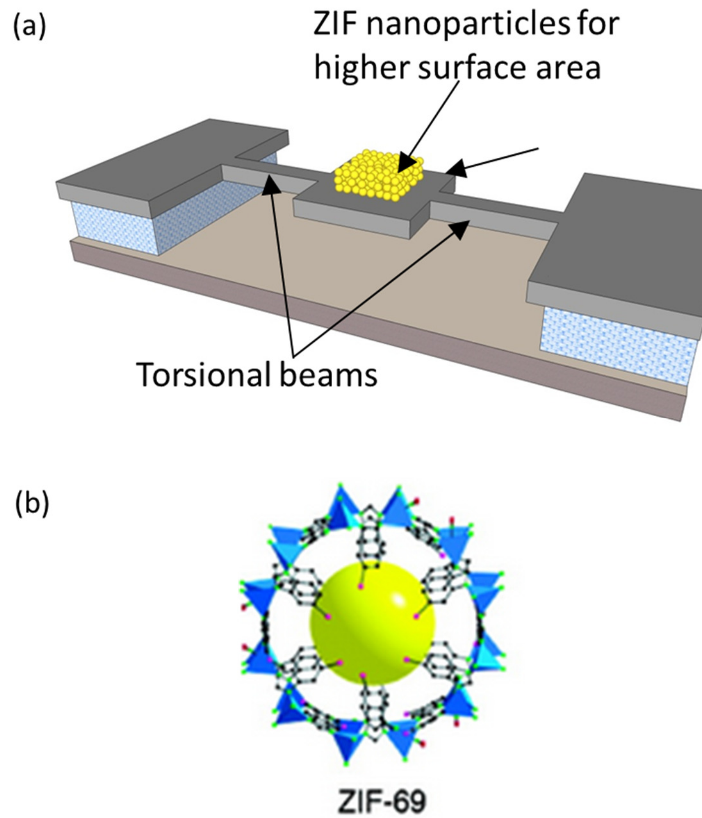

Figure 33. (a) Sketch of the proposed nanoparticle-agglomerated resonator. ZIF nanoparticles are attached on a target region in the center paddle of the resonator. (b) Crystal structures of ZIF-69. The largest cage in each ZIF is shown with ZnN_4 in blue and CoN_4 in pink polyhedra, and the links in ball-and-stick presentation. The yellow ball indicates space in the cage. H atoms are omitted for clarity [91].

Coupling nanoparticles to the silicon resonator requires careful considerations of the thermal and chemical properties of the nanoparticles, as well as factors that affect the performance of the device, as follows.

1) The synthesis and assembly of the ZIFs are separate, because ZIFs are synthesized through several wet chemical steps [83] whose comparability with the standard microfabrication has not been verified. Hence, typical deposition techniques including chemical vapor deposition, sputtering, thermal/e-beam evaporation and atomic layer deposition are not viable to assemble

nanoparticles. On the other hand, it is necessary to note that the separation of synthesizing nanoparticles from assembling them to a sensor structure gives a broader range of choices for functionalization of such resonator sensor.

2) The nanoparticles should have maximum exposure to the surrounding environment to ensure maximum physical adsorption of analytes rather than being swamped in adhesive materials. The random spreading and nanomanipulation techniques [97, 98] are not suited for this case, because dense assembly of large amount of ZIFs is required.

3) The nanoparticles should be deposited in targeted regions of the resonator, as opposed to blanket coatings. Targeting deposition of nanoparticles is preferred over blanket coating because covering the beams could lead to surface stresses, lowering the resonator quality factor due to surface-induced energy dissipation [40] and counterbalancing the resonant frequency shift due to increased bending stiffness of the beams [99].

4) ZIFs are damaged at high temperatures greater than 390 ˚C or in acidic solutions, such as hydrofluoric acid (HF), sulfuric acid, and hydrochloric acid. Therefore, etching of the sacrificial layer must occur before assembly of the nanoparticles. To avoid stiction, a process that utilizes a thick photoresist as the second sacrificial layer during assembly of the nanoparticles has been devised. It is important to note that a diverse class of nanoparticles synthesized by various methods can be deposited with this technique, as the synthesis and assembly of the nanoparticles are separate in this process.

5.4 Fabrication

The nanoparticle-agglomerated microresonators in this work consist of 45-µm-long, 10-µm-wide torsional beams and a 45-µm-long, 45-µm-wide center paddle. They are fabricated using sublimation drying with p-DCB and a two-step sacrificial layer process in combination with

standard surface micromachining processes. Unless otherwise specified, fabrication processes are carried out at room temperature. As depicted in Figure 34, the process starts with PECVD deposition (Plasmatherm 790) of a 5.5-µm-thick layer of silicon dioxide (SiO_2) at 250 ˚C as the first sacrificial layer on a 4-inch (100) silicon wafer. Next, a 470-nm-thick polysilicon structural layer is deposited via LPCVD (Tystar Titan II furnace) at 600 ˚C, patterned via photolithography (AZ 5214 photoresist and KarlSuss MA-6 aligner), and etched via deep reactive ion etching (SLR 770 ICP) to define the resonators (Figure 34 (a-b)). The SiO_2 sacrificial layer is removed by immersing wafers in 49% HF solution for 150 seconds, followed by immersion in DI water (Figure 34 (c)). To eliminate capillary forces, the following immersion steps are performed. First, DI water is replaced with methanol, a low surface tension solvent. Methanol is then replaced with melted sublimation liquid, p-DCB, at ~65 ˚C. Finally, photoresist (PR) (AZ 4620) is immediately poured over the p-DCB (Figure 34 (d-e)). Immediate coating of PR is required because the p-DCB rapidly solidifies and begins to sublimate. The wafer is placed in a vacuum chamber, causing the solid p-DCB under the released structures to sublimate. The PR flows to replace the p-DCB as the p-DCB sublimates. After the p-DCB is fully sublimated, the device will be completely underfilled and covered by PR. The PR is then spun at 2500 rpm to create a uniform thickness for the nanoparticle molds.

The PR is then patterned using conventional photolithography techniques into a mold for the nanoparticles (Figure 34 (f)). The PR layer plays dual roles in this process, acting as both the second sacrificial layer by providing support underneath the resonator and a mold for the nanoparticles on top of the resonator. The PR mold is filled with nanoparticles using the following steps. First, the nanoparticles are sonicated in DI water for 15 minutes to ensure uniformity of the nanoparticle dispersion in water then poured over the PR mold. A flat blade is

used to sweep across the surface of the mold and pack the nanoparticles into the trenches [83], ensuring agglomeration and attachment of the nanoparticles onto the center paddle of the resonator (Figure 34 (g)). The nanoparticles adhere onto the silicon surface without an adhesive layer, possibly a result of van der Waals forces [100].

The nanoparticles utilized in this work are ZIF-69 (zeolitic imidazolate framework), which are synthetic, three-dimensional, crystalline structures constructed from zinc frameworks bridged by imidazolate units. ZIF-69 is prepared by a recently reported synthesis method [83]. They have random shapes less than 1 μm in diameter, and they exhibit a high affinity for CO_2. For example, 1 L of ZIF-69 can store 49.2 L of CO_2 gas at 273 K [91]. The ZIF-69 nanoparticles cannot survive an HF etch or temperatures above 390 ºC but are impervious to the acetone used during final release of the structure, making them ideal candidates for use with this process. Other typical release methods, such as supercritical point drying and HF vapor etching, are not compatible with this two-step sacrificial process; both supercritical point drying and HF vapor etching would fully release the structure, and refilling released structures could lead to surface tension forces and stiction.

Finally, the PR is removed with acetone to release the nanoparticle-agglomerated resonator (Figure 34 (h)), and sublimation drying of p-DCB is performed again to avoid stiction. The second sublimation drying procedure does not prevent the nanoparticles from providing enhanced surface area for adsorption, as it is performed at relatively low temperature (~ 65 ˚C) and adsorbed p-DCB is completely removed by sublimation in a vacuum desiccator for three hours.

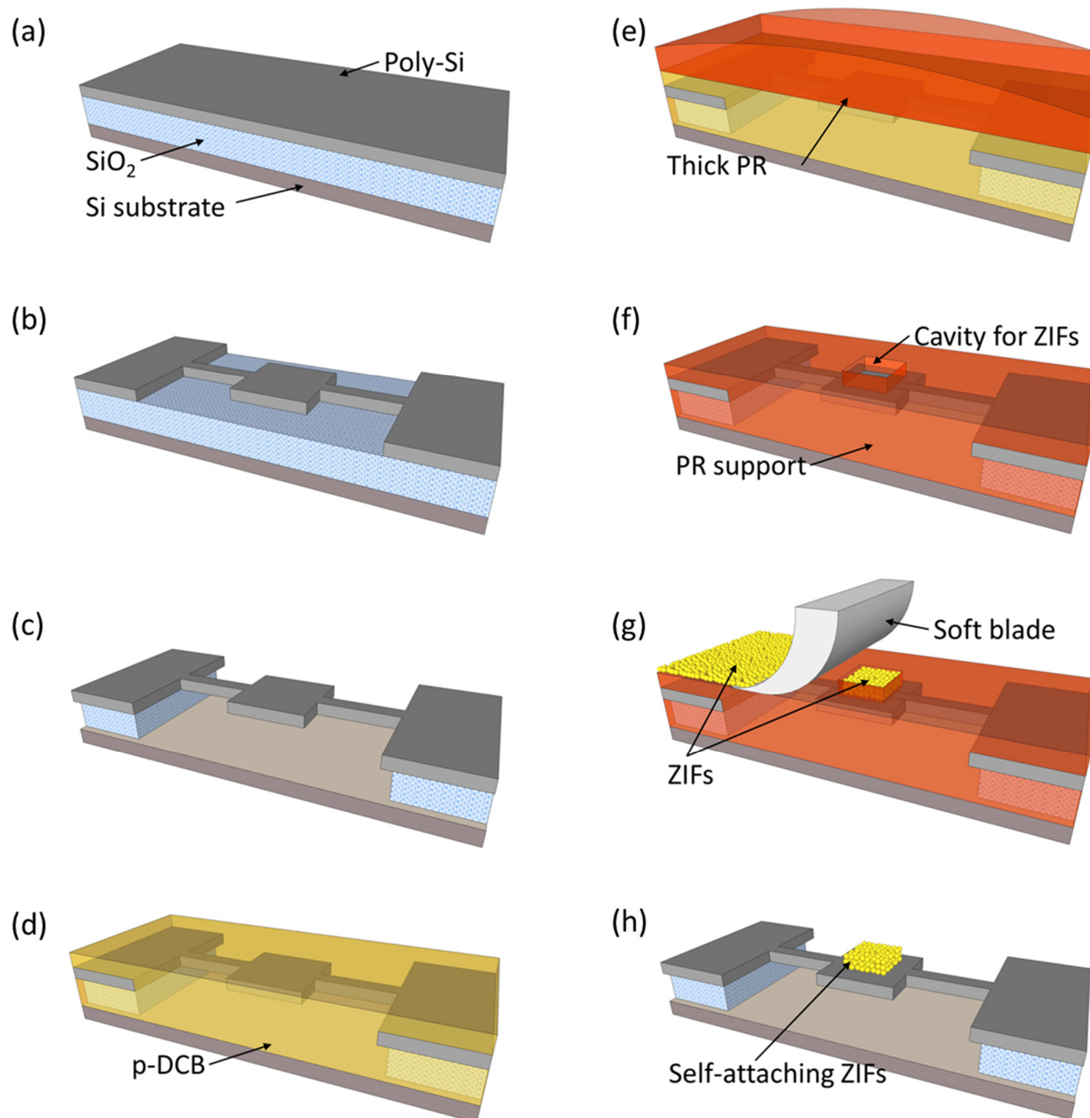

Figure 34. Fabrication process for ZIF-agglomerated resonator by a drop casting. (a) Depositing of SiO_2 and polysilicon. (b) Patterning body of the resonator. (c) Etching the sacrificial layer. (d) After rinsing, replacement of rinsing liquid with melted p-DCB. (e) Coating thick photoresist. (f) Patterning the photoresist support structure as a sacrificial layer and cavities for a target region of ZIF particles. It is important to note that the PR support replaces the solid p-DCB under the released resonator and also defines the mold on top of the resonator. (e) Sweeping of distributed ZIF particles by a flat blade, leaving packed ZIFs in the cavity. (f) Dissolution of the PR support layer and sublimation drying with p-DCB.

The PR is shown to successfully reflow and replace the sublimated p-DCB, as shown in Figure 35. The PR support as the second sacrificial layer completely covers the torsional beam of the released silicon resonator; however, when the PR is coated after sublimation of the p-DCB is completely finished (*i.e.*, no replacement of the PR with the p-DCB), the resonator becomes adhered to the substrate, as presented in Figure 36. Once the support PR is baked, it adequately supports the resonator structure during the subsequent process steps, including when direct force is applied during packing of the nanoparticles. Figure 37 represents several images of samples where the ZIF nanoparticle agglomerates (10 μm in diameter, 5 μm thick) are coupled on the silicon resonators. Resonators are adhered to the substrate when sublimation drying is not used (Figure 37 (a-b)) and are successfully released when sublimation drying is used (Figure 37 (c-d)). The PR support layer becomes slightly thinner under the resonator arising from the centrifugal forces of PR spinning. This thinning of PR induces strain and results in resonator bending (Figure 38 (b)). As demonstrated in Figure 37 and Figure 38, no residues are visible after sublimation drying.

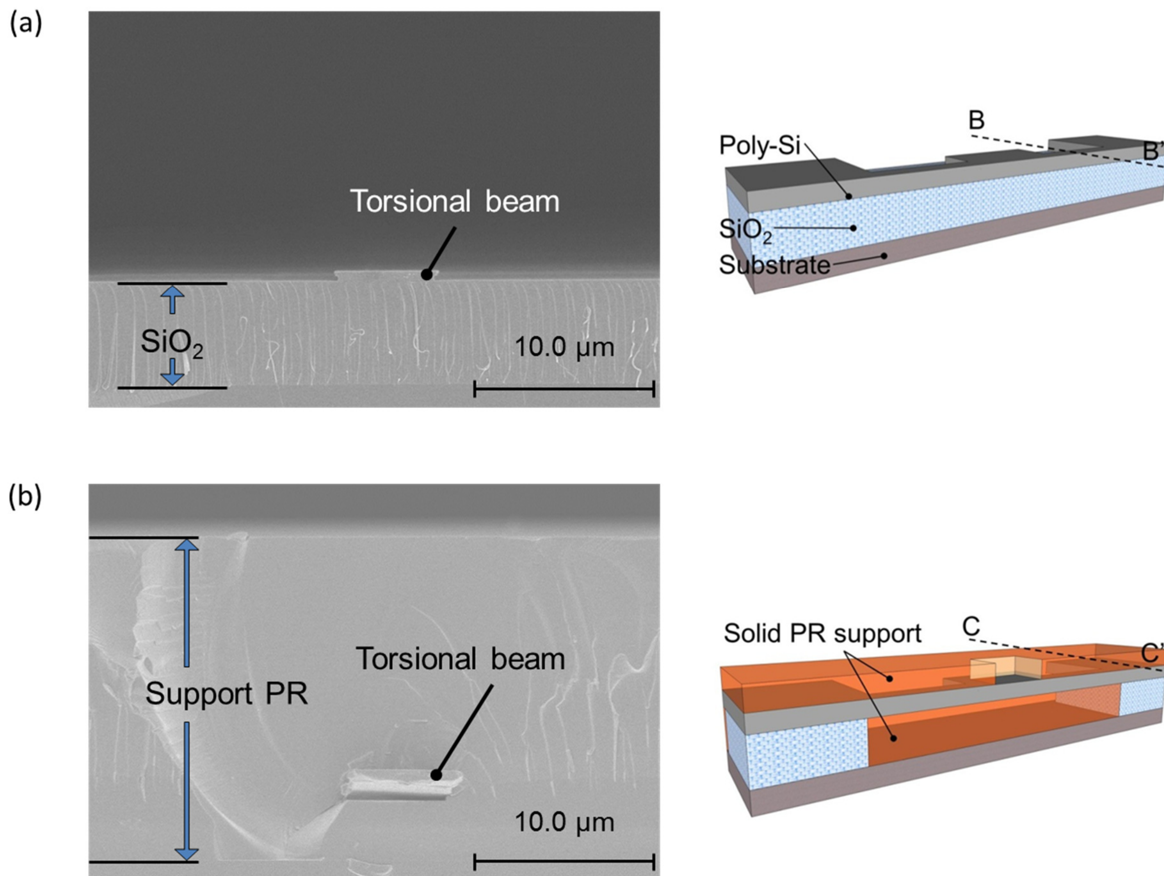

Figure 35. SEM images of resonator cross-sections. (a) Cross-section taken along BB' after definition of the resonator structure. (b) Cross-section taken along CC' after patterning of the PR support layer. The PR support as the second sacrificial layer completely covers the torsional beam of the released polysilicon resonator.

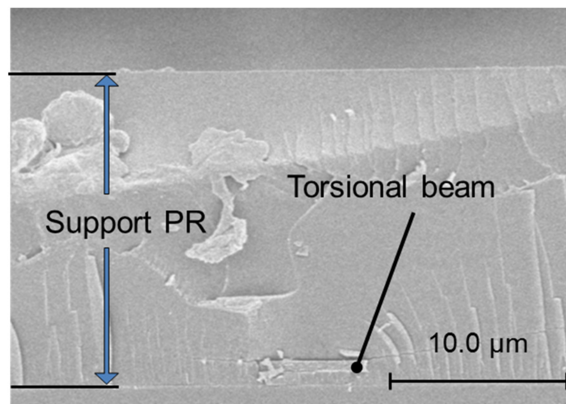

Figure 36. SEM image of resonator cross-section cross-section taken along CC' in Figure 35 when the PR is coated after sublimation of the p-DCB is completely finished (*i.e.*, no replacement of the PR with the p-DCB). The resonator becomes adhered to the substrate.

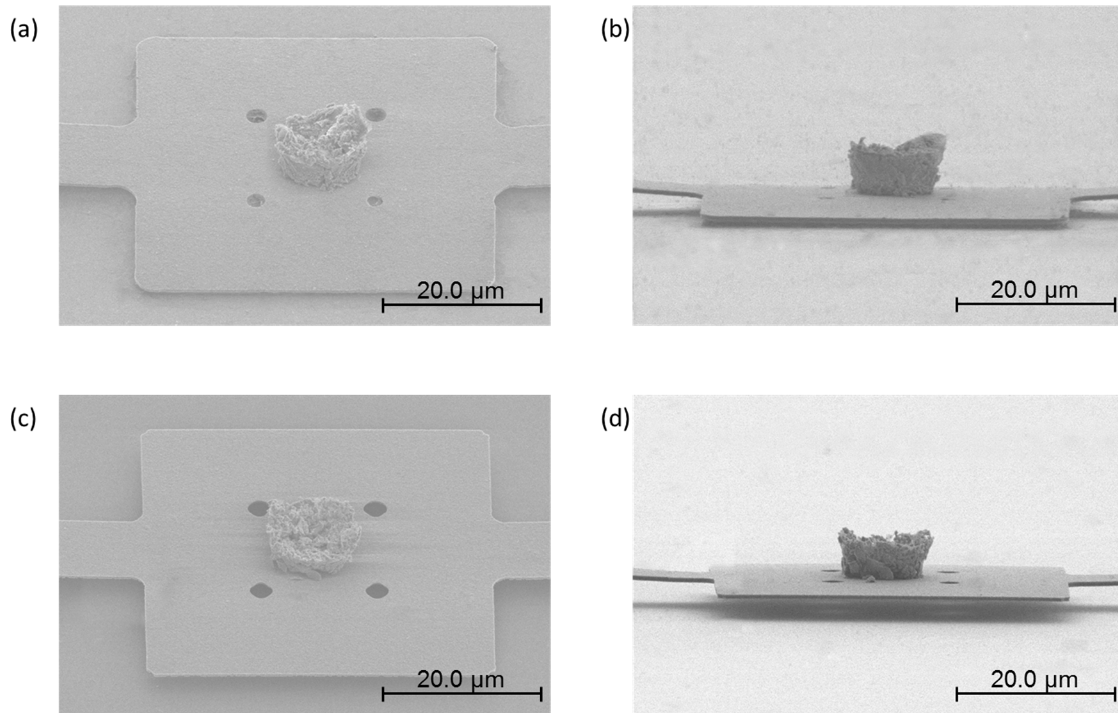

Figure 37. Tilted SEM images of the ZIF-agglomerated resonators. (a) and (b) the resonator of the same design is usually adhered to the substrate if measures are not taking to address stiction (*i.e.* after removal of the PR support with acetone, the sample is air dried). However, (c) and (d) the resonator is successfully released by the aid of the sublimation drying of p-DCB.

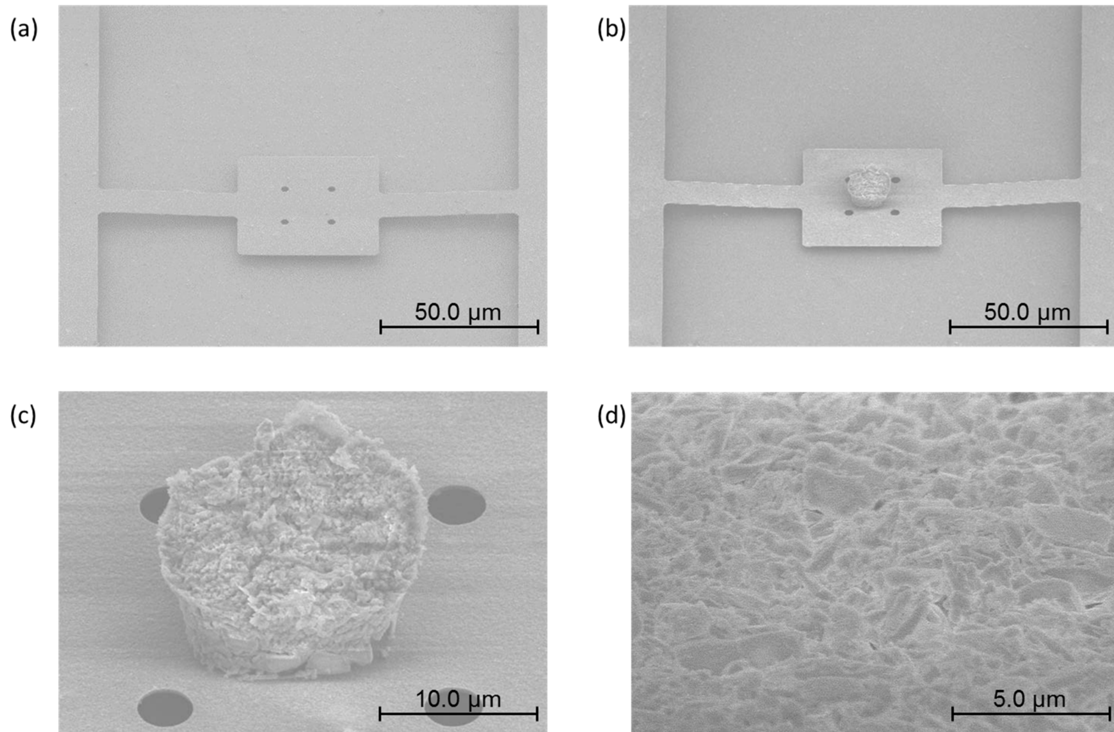

Figure 38. SEM images. (a) A silicon resonator without nanoparticles. (b) A ZIF-agglomerated resonator with a 10 µm × 10 µm × 3 µm casting of ZIFs by the drop casting method. (c) Enlarged image of ZIFs attached on the surface of the resonator. (d) Enlarged image of agglomerated ZIFs

5.5 Experimental results

The ZIF-agglomerated resonators are tested using the Laser Doppler vibrometer system and the network analyzer to verify their potential use as gas sensors. The influence of the process on resonant frequency is described in Figure 39. The fabrication-induced bending of the resonator beams (Figure 38 (b)) leads to an increase in resonant frequency. The addition of ZIF particles shifts the resonant frequency downward due to the increase in mass. However, standard deviation of the resonant frequency was between ~1-2% for each of the three processing

techniques, implying the PR support technique does not have a considerable effect on uniformity of the devices.

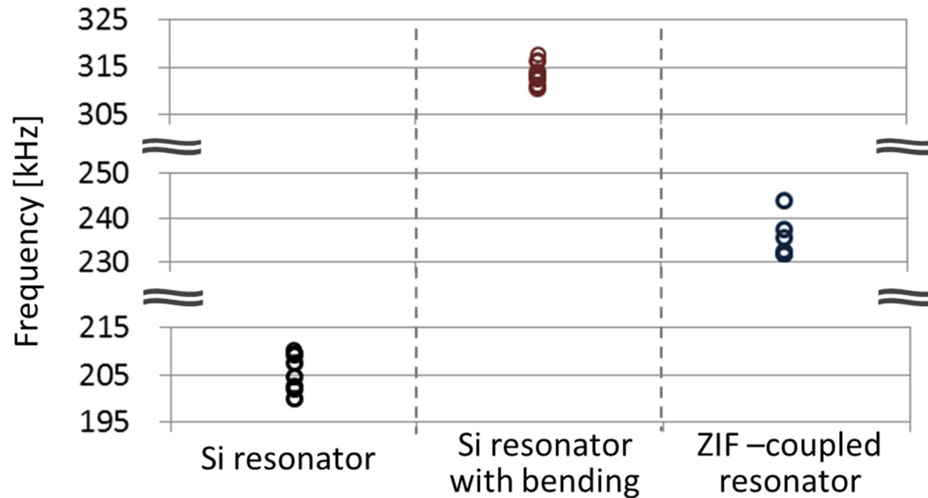

Figure 39. Resonator frequency distribution and response to gas. The resonant frequency distribution of the silicon resonators without the PR support technique (*i.e.*, just a single p-DCB release), with the PR support technique (and resulting bending) with no nanoparticles, and with the PR support technique and nanoparticles. Standard deviation of the resonant frequencies is 3.87 kHz, 2.40 kHz, and 5.03 kHz, respectively. Each data point is for a separate device. Eight devices were measured for each category.

To estimate the ZIF sensing properties, control experiments are performed using silicon resonators without ZIFs, which will subsequently referred to as silicon resonators. The measured short-term frequency noise floor and quality factor of the resonators are shown in Figure 40. The standard deviations of the resonant frequencies of the ZIF-agglomerated and the silicon resonator are 11.42 Hz (49 ppm) and 2.89 Hz (12 ppm), respectively. Temperature-induced frequency drift for silicon resonators is one possible noise source, as the temperature dependence of Young's modulus causes a frequency shift of approximately 10 ppm/˚C [101, 102]. Also, a mismatch of

thermal expansion coefficient of additional material (*i.e.*, ZIFs in this work) might induce stress and a resulting frequency shift [103]. The presence of ZIFs on the resonators reduces the quality factor by a factor of three. Surface-induced energy dissipation [40] is one possible cause of the quality factor degradation seen when ZIFs are added to the resonator. The minimum detectable mass is calculated as $\delta M = 2m\delta f / f_0$ [104], where m (~3.1×10^{-9} g) and $\delta f / f_0$ are the total mass and noise floor of the resonator, respectively. Hence, the limit of detection of the ZIF-agglomerated resonator for gas sensing is expected to be ~0.3 pg.

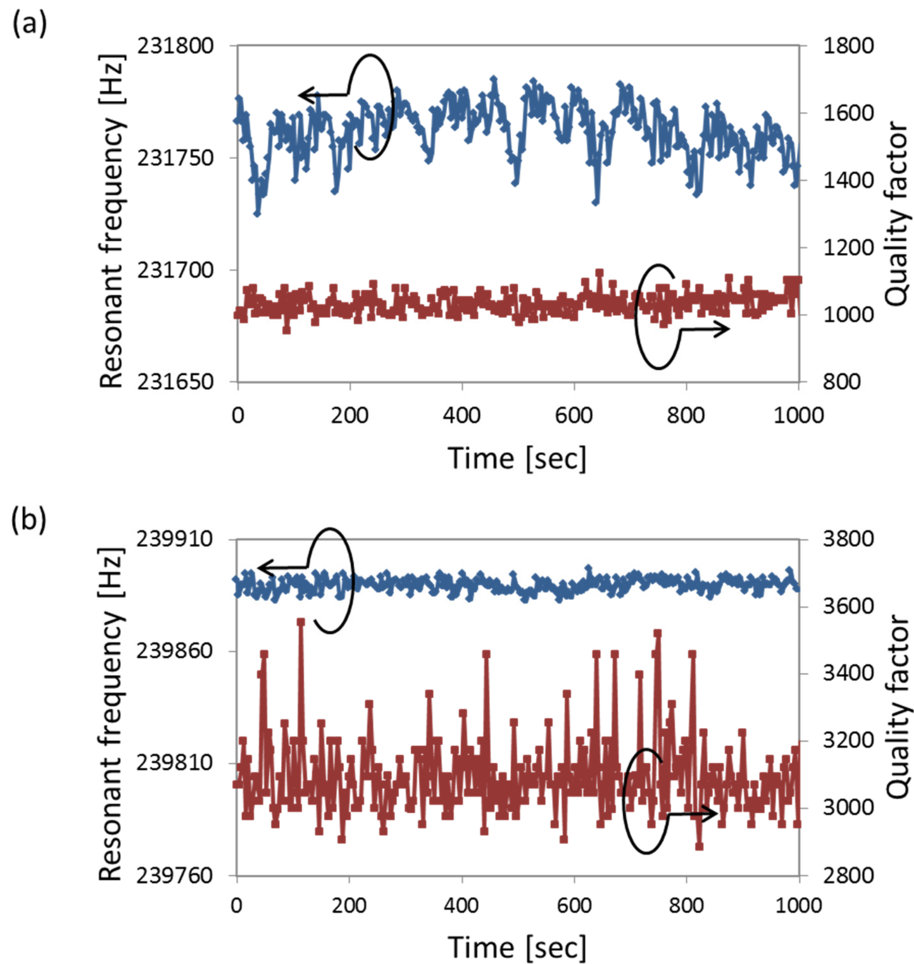

Figure 40. Measured noise floor and Q factors of the systems with (a) the ZIF-agglomerated resonator and (b) the silicon resonator during 1000 s measurement period with a 0.62 Hz resolution bandwidth.

Figure 41 contains characteristic frequency spectra showing shifts and real time frequency measurements under different gas conditions. When 1500 ppm IPA (isopropyl alcohol) is introduced into the testing chamber, 575 Hz frequency drop is observed that is about 50 times the 11 Hz noise floor. The responses are repeatedly recovered to their baseline values upon removal of gas, indicating reversible adsorption.

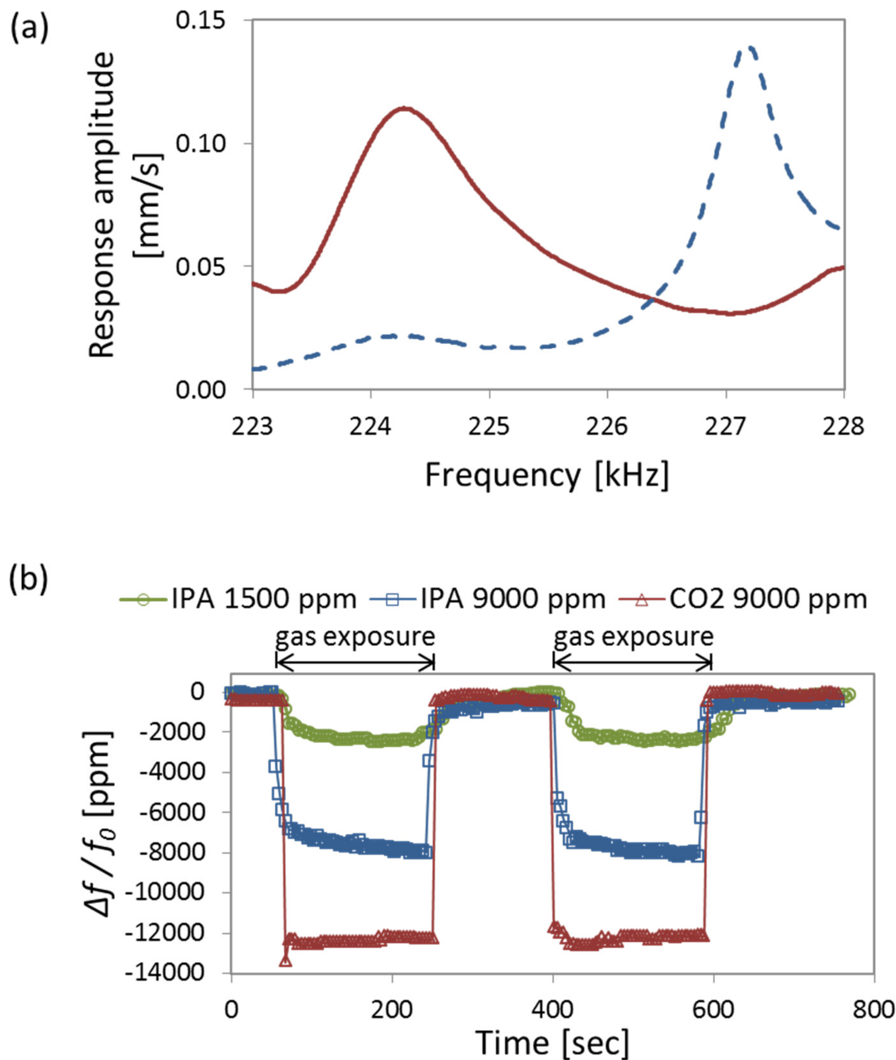

Figure 41. Measured performance of the ZIF-agglomerated resonant gas sensors. (a) Frequency spectra of with no CO_2 (dashed line) and 9000 ppm of CO_2 (solid line). (b) A typical set of real time frequency shifts exposed to IPA and CO_2 gas**.**

Figure 42 presents a typical set of measured frequency shift of the ZIF-agglomerated resonator. Figure 43 shows $\Delta f / f_0$ resulting from adsorption and desorption of different gases and the different responses to gas of the silicon resonators with and without ZIF coupling. Whereas the frequency shifts of the silicon resonator without ZIFs during gas adsorption are almost

negligible because of the insufficient adsorption, the resonant frequency of the ZIF-agglomerated resonators changes substantially due to the increase in surface area afforded by assembled ZIFs. The process flow was designed to avoid adhesive binders that could clog the ZIFs, enabling this enhanced sensitivity to be realized. Nevertheless, the accumulation of gas on the ZIFs is likely to inhibit further absorption at some point, leading to saturation and reduced sensitivity at higher concentrations.

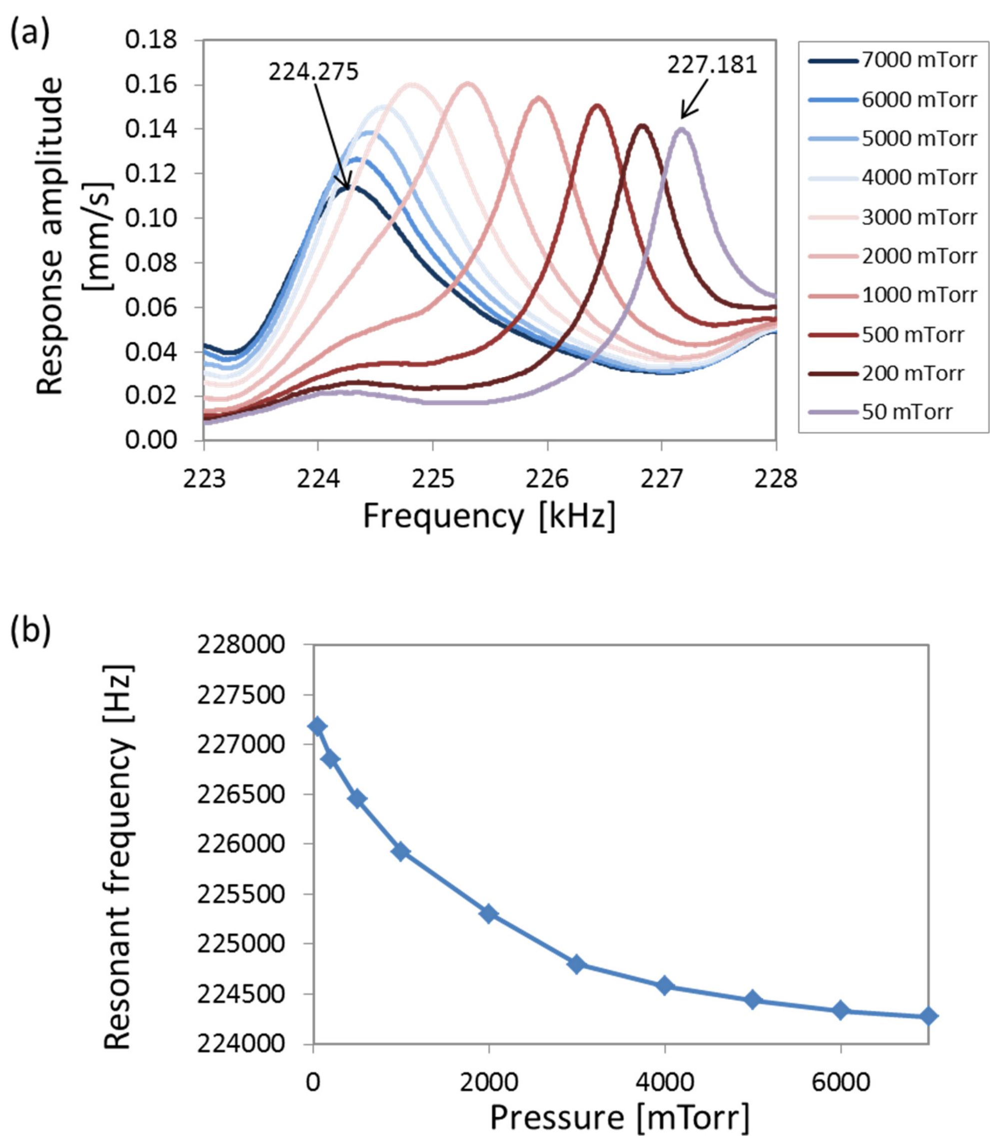

Figure 42. (a) A typical set of measured frequency shifts for ZIF-agglomerated resonators exposed to CO_2 gas, (b) resonant frequency vs. analyte gas pressure (CO_2) extracted from (a).

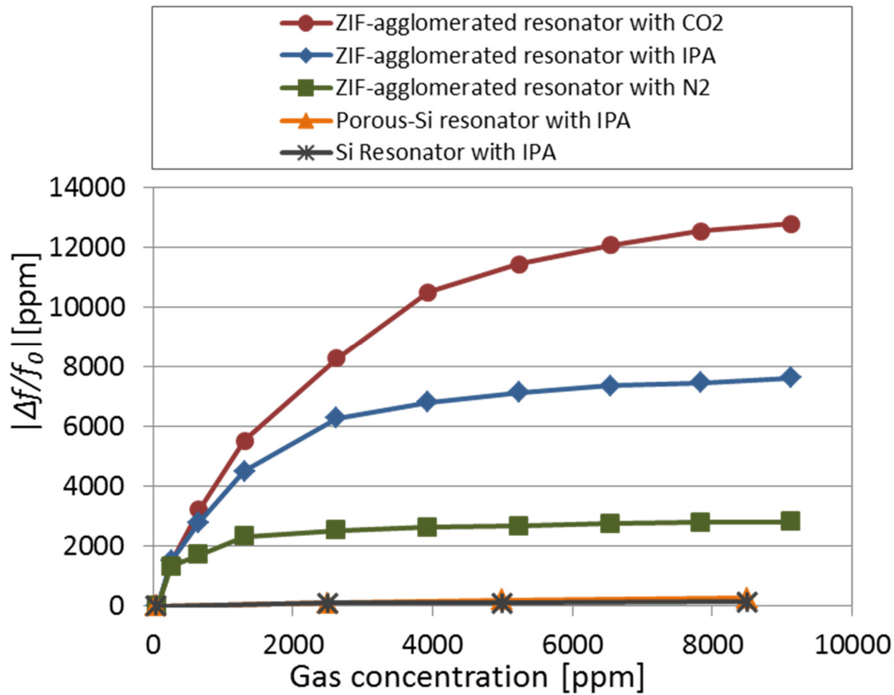

Figure 43. Response of the ZIF-agglomerated, porous, and silicon resonant gas sensors to N_2, IPA and CO_2 gas.

As a result, the ZIF-agglomerated resonators show higher frequency shifts ranging between 35 and 78 times for different gas concentrations compared to resonators without ZIFs. Furthermore, because of the inherent selectivity of ZIFs [83], the ZIF-agglomerated resonator has 1.7 times higher sensitivity to CO_2 than IPA in spite of the lighter molar mass of CO_2. Assuming that the frequency shift is affected only by the mass change, the mass adsorbed on ZIF-agglomerated resonator for a CO_2 concentration of 2500 ppm is calculated to be 51 pg from Equation 11. As an areal mass of CO_2 is calculated as 28 ng/cm^2 [105], the amount adsorbed onto the ZIF-agglomerated resonator corresponds to 37 monolayers on the silicon resonator surface of 4900 μm^2, which implies the adsorption of the ZIF-agglomerated resonator occurs not only on the

surface but also inside the ZIFs as desired. Therefore, the ZIFs enhance the surface area for gas detection, enabling the sensitivity of the gas sensor to be improved.

Chapter 6 ZIF-coupled resonant gas sensor using dielectrophoretic nanoassembly

Although the ZIF-agglomerated resonator using the drop casting method in Chapter 5 demonstrates enhancement of the sensitivity as a gas sensor, it can raise reproducibility issue in terms of fabrication arising from handling ZIF particles by hand-controlled flat blade. In addition, gas adsorption of inner ZIFs of the ZIF agglomerate is likely to be limited at high concentration range of gas. Direct growth [106], catalyst [107], random spreading [97], nanomanipulation [98, 108], and bonding [109] have been demonstrated for positioning nanoparticles. However, such methods are not suited for assembling ZIFs as a sensing material, because dense assembly of large amount of ZIFs is required. Considering uniform assembly and maximum exposure to surrounding gas, dielectrophoresis force can be utilized for alternative ways for assembling ZIF nanoparticles.

6.1 Dielectrophoresis

Dielectrophoresis (DEP) has been demonstrated as a simple and effective method to rapidly manipulate, sort, and assemble both biological and synthetic colloidal particles. DEP force acting on a particle caused by the interfacial polarization between the particle and the media in a non-uniform electric field is predicted as [110],

Equation 16

$$\langle F_{DEP} \rangle = 2\pi r^3 \varepsilon_m Re[CM] \nabla |E|^2$$

Equation 17

$$Re[CM] = \frac{\varepsilon_p - \varepsilon_m}{\varepsilon_p + 2\varepsilon_m}$$

where r is the particle radius, $Re[CM]$ is real part of Clausius-Mossotti (CM) factor, ε_m is the permittivity of the media, ε_p is the permittivity of the particle and E is the electric field. Here, the CM factor is used as an indicator that describes how effective the polarization varies with the material properties and the frequency of the applied electric field, and is bounded by 1 and -0.5 [111]. The CM factor is determined as a function of frequency by measuring velocities of particles when the particles are moved by DEP force generated by coplanar electrodes [110].

At low frequencies it is possible to induce positive DEP ($Re[CM] > 0$), where particles are attracted to an electrode edge. Transition to negative DEP occurs at high frequencies, where particles are repelled into regions of low electric field strength. As ZIFs are newly developed materials, thorough experimental study regarding DEP characteristics of ZIFs has not yet been performed. Thus, properties regarding the DEP phenomenon, such as crossover frequency and CM factor, are studied in this work for ZIFs assembly.

6.1.1 Simulation of DEP force

The two dimensional FEM simulation is carried out using the AC/DC module of COMSOL Multiphysics 4.2. A 200 μm wide, 100 μm high chamber is designed with five electrodes on the bottom surface. The parallel electrodes are modeled with a height of 1 μm, a width of 10 μm, and variable spacing between 1 μm and 90 μm on the bottom surface. For the electrostatics simulation, 5 V voltages are applied on the odd number electrodes, ground on the even number electrode, and zero charge on the outer boundary and the bottom surface.

Figure 44 shows DEP force plots from the normal electric field lines around the microelectrodes, assuming particles of 1 μm in radius, CM factor of 0.5. The arrows and streamlines have uniform density to show only the directions of DEP force, which is towards the electrode edges. According to the electric field gradient, DEP force is maximum close to the

electrode edges. When the spacing is increased from 1μm to 90 μm, Figure 44 (e) shows the change in the DEP forces at the tip regions. For a short spacing of 1 μm the DEP force has a maximum value in the order of 10^{-8} N and confined very strongly at the edges. The arrows depicting the electric field gradient are directed toward electrode edges. As the spacing is increased to 90 μm, the DEP force decreases by almost an order of magnitude to 10^{-9} N. Also, the directions of the arrows diverge and point towards the two electrode edges separately.

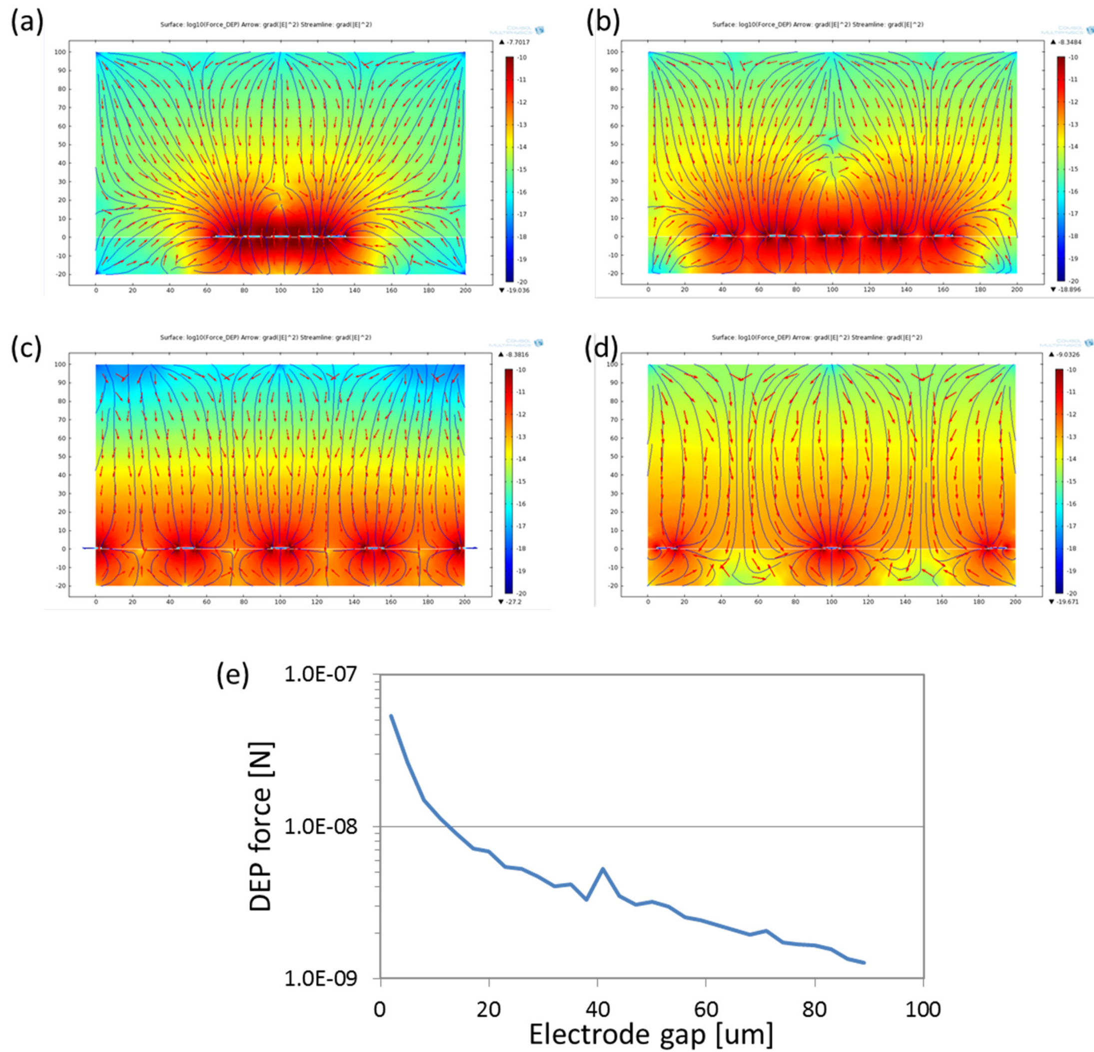

Figure 44. Two dimensional simulations for parallel electrodes with a spacing of (a) 5 μm, (b) 20 μm, (c) 40 μm, and (d) 80 μm. (Surface plot: $\log_{10}$(DEP force) [N], Arrows and stream lines: $\nabla|E|^2[V^2m^{-3}]$, Arrow lengths do not represent magnitude of the electric field gradient.) (e) DEP forces are calculated through parametric study as the electrode gaps are changed.

6.1.2 Measurements of Clausius-Mossotti (CM) factor

When a particle is suspended in a fluid, DEP force can dominate electrokinetic hydrodynamical forces, such as ac electro-osmosis and the electrothermal effect [112]. Thus, the

drag force for a spherical particle with the velocity $U_{particle}$ in a fluid with the viscosity η is given by

Equation 18

$$F_{drag} = 6\pi r\eta U_{particle}$$

When the DEP is induced by an ac voltage, the particle begins to move by a pure DEP regime. Therefore, the drag force to the particle comes from the DEP, indicating $F_{drag} = \langle F_{DEP} \rangle$. From Equation 16, the CM factor of the particle can be determined by

Equation 19

$$Re[CM] = \alpha U_{particle}$$

$$\text{where } \alpha = \frac{3\eta}{r^2 \varepsilon_m \nabla |E|^2}$$

To experimentally determine the CM factor of ZIF-69 [110], the following setup is prepared to measure velocities of particles in solution. Each device used for experimental studies consists of a glass substrate (Pyrex 7740) containing parallel gold electrodes with different width and spacing. A PDMS (Polydimethylsiloxane) cover, containing a recessed chamber and inlet/outlet is then placed on top of the glass to form a completed channel. The 100 µm thick electrodes are fabricated using a lift-off process. The chambers and channels are created using PDMS replica molding, where the mold is formed by a three dimensional printer (Objet 24) [113]. Figure 45 shows experimental setup with an assembled PDMS mold, electrodes and tubes for ZIF dispersion.

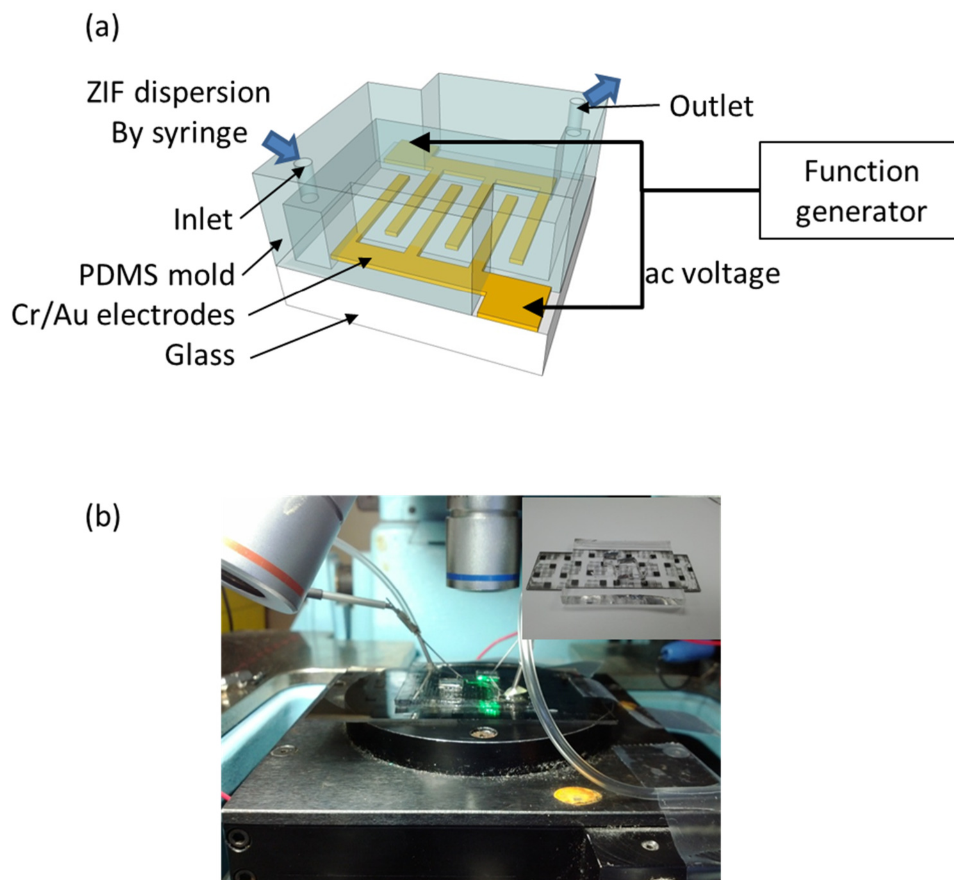

Figure 45. Schematic and photos of the experimental setup for dielectrophoretic particle capture.

Particle motions are recorded via a CCD camera at 59 frames/second. Recorded videos are then analyzed by IMAGEJ software [114]. The particle tracker plug-in is capable of tracking multiple particles and calculating the velocity of each particle. Figure 46 shows a typical parameter setup of the particle tracking software. The average velocities are multiplied by the factor α by Equation 19, where the COMSOL Multiphysics 4.2 simulations extract the electric field gradient.

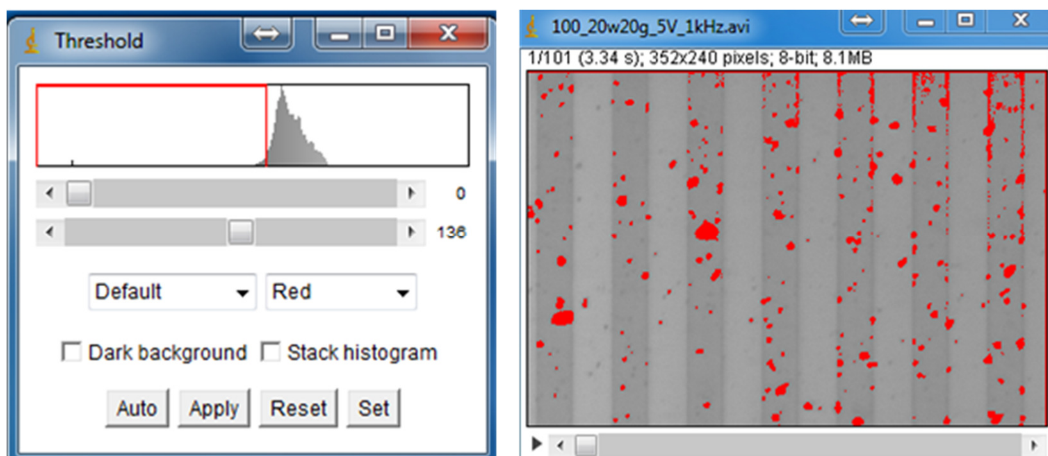

Figure 46. An example setup of the particle tracking plug-in. By controlling a threshold of brightness of the recorded video, particles to be tracked are selected.

As shown in Figure 47, at low frequencies ZIFs are collected along the edge of the electrodes, indicating positive DEP dominant ranges. As the frequency is raised, the strength of positive DEP becomes diminished and is replaced with negative DEP for any applied frequency. Thus, ZIFs accumulate on the center of the electrode, between electrodes, or may even levitate above the electrodes. On intermediate regime some particles are observed to form chains along the electric field gradient lines due to interparticle electrostatic interactions [115]. Experimental CM factor values for ZIF-69 particles are plotted in Figure 48, indicating that the crossover frequency between positive- and negative DEP is around 300 kHz.

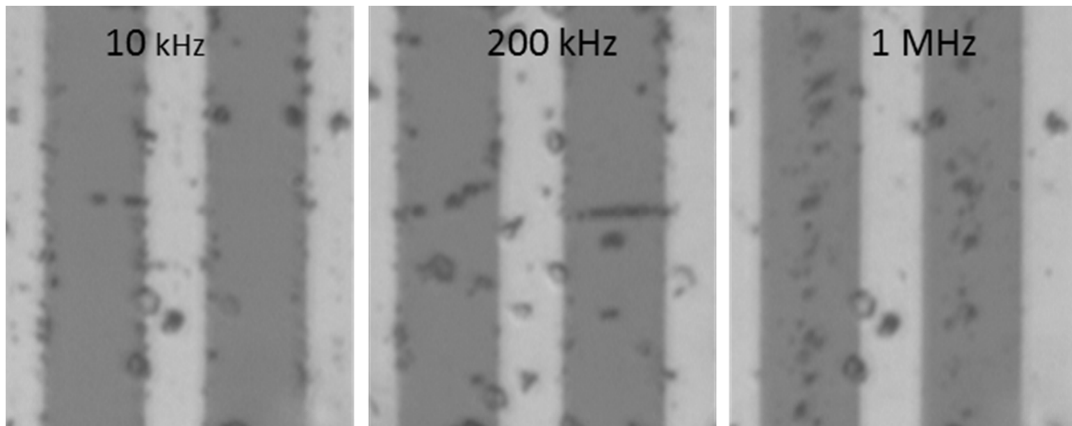

Figure 47. Coplanar electrodes (10 μm wide and 15 μm spacing) with ZIF-69 particles at 10 kHz, 200 kHz and 1 MHz suspended in DI water. The particles are attracted to the edges of the electrode by positive DEP at 10 kHz and are repelled to the center gaps between electrodes by negative DEP at 1 MHz.

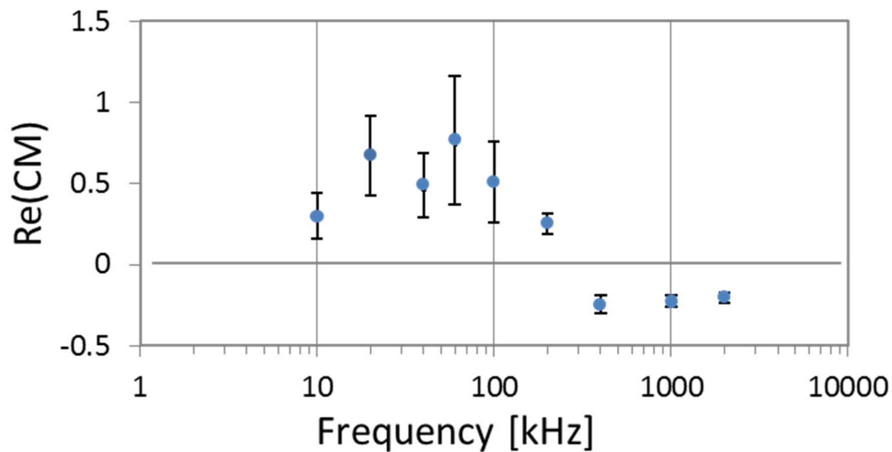

Figure 48. Clausius–Mossotti (CM) factor as a function of frequency for ZIF-69 in a range of 10 kHz up to 2 MHz. Particle motions are recorded and the CM factors were extracted by their velocities. The crossover frequency for positive- and negative DEP is ~300 kHz.

6.2 Fabrication

The ZIF-coupled microresonators are designed to have a 450-nm-thick, 45-µm-long, 45-µm-wide center paddle, which is fixed to anchors through 450-nm-thick, 45-µm-long, 10-µm-wide torsional beams. They are fabricated using DEP for ZIF assembly and a two-step sacrificial layer process in combination with standard surface micromachining processes. As depicted in Figure 49, the process starts with PECVD deposition of a 5.5-µm-thick layer of silicon dioxide (SiO_2) at 250 ºC as the first sacrificial layer and with LPCVD deposition of a 450-nm-thick polysilicon at 600 ºC as a structural layer on a 4-inch (100) silicon wafer. Next the structural layer is patterned via photolithography and etched via deep reactive ion etching to define the resonators (Figure 49 (a)). Cr/Au (chromium/gold) electrodes are fabricated by a lift-off process on the silicon surface for planar electrodes to generate DEP force (Figure 49 (b). After covering photoresist (PR) passivation layer for the metal electrode (Figure 49 (c), the SiO_2 sacrificial layer is removed by immersing wafers in 49% HF solution for 300 seconds, followed by immersion in DI water. In this case, there are no etch holes on the center paddle to ease patterning of the the Cr/Au electrodes, so that longer etch by HF solution is required to fully release the structure. Additional etch of SiO_2 under the fixed pad edges is offset by controlling the size of the PR passivation that covers the fixed pad. Next, the same steps described in section 5.4 is performed for the PR replacement technique (Figure 49 (d-f)).

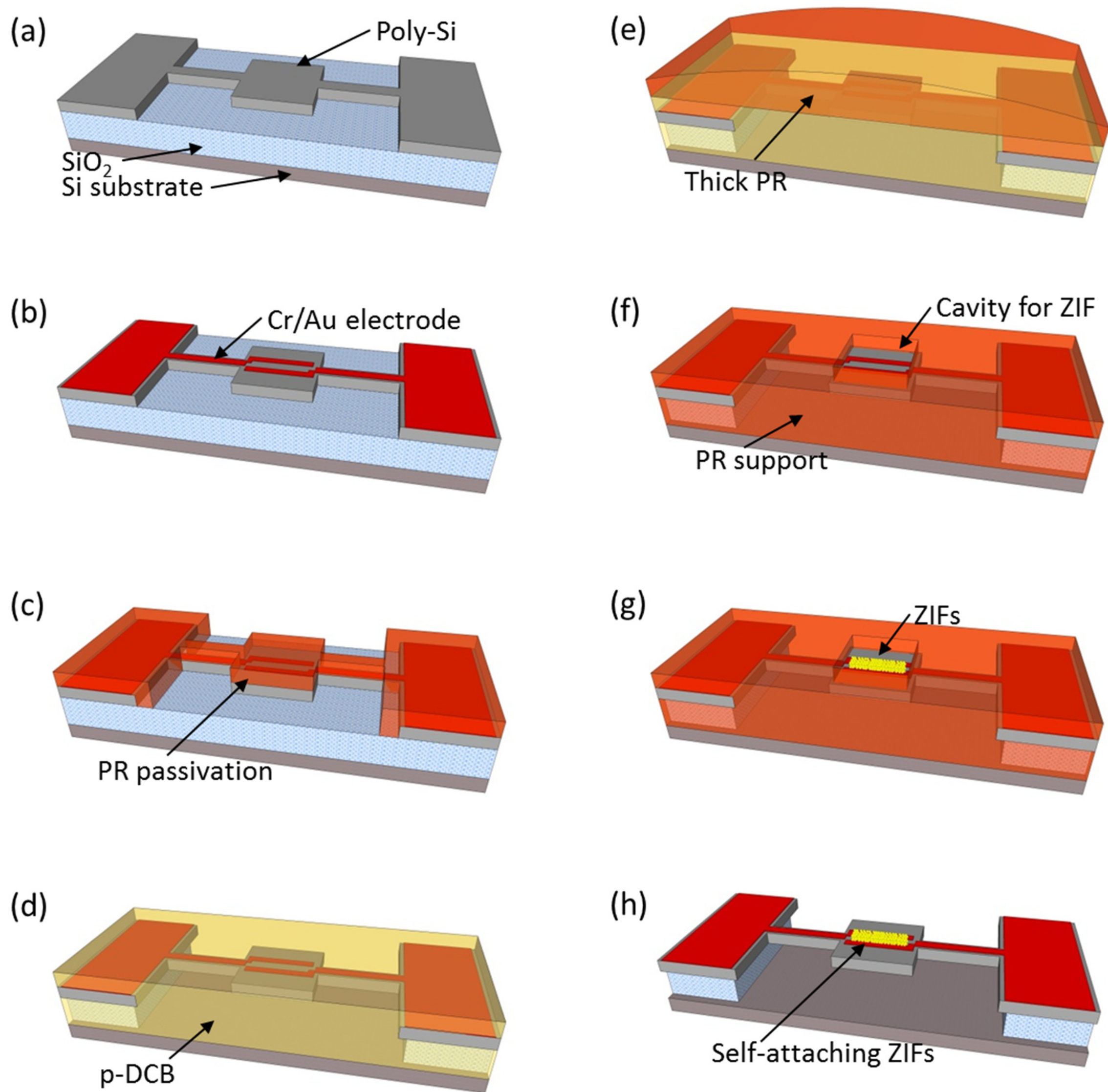

Figure 49. Fabrication process for ZIF-coupled resonator using DEP. (a) Patterning body of the resonator. (b) Lift-off for planar electrodes. (c) Covering passivation layer for the metal electrodes. (d) Etching the first sacrificial layer and filling p-DCB underneath the resonator. (e) Pouring thick photoresist over the solid p-DCB. (f) Reflowing the photoresist and patterning it as the second sacrificial layer and cavity for a target region of ZIF particles. (g) Assembling ZIF particles by DEP-induced attractive force. (f) Releasing the ZIF-coupled resonator.

ZIFs are assembled using the following steps (Figure 49 (g). First, ZIF-69 particles are sonicated in DI water for 15 minutes to ensure uniformity of ZIF dispersion and then poured over the PR mold. To generate DEP force, an ac voltage of 5 V_{pp} at a frequency of 10 kHz by a function generator is applied on the planar electrode. Until the DI water of the poured ZIF dispersion is evaporated, ZIFs are collected and aligned on electrodes of the center paddle. ZIFs adhere onto the silicon surface without an adhesive binder, possibly a result of van der Waals forces [100]. Finally, the PR is removed with acetone to release the ZIF-coupled resonator (Figure 49 (h), and sublimation drying of p-DCB is performed again to avoid stiction.

Figure 50 compares the fabricated silicon resonators with and without ZIFs. ZIFs appear to spread more than the previous results by the drop casting (See Figure 38). By virtue of dense ZIF dispersion, electrodes on the target region are heavily covered with ZIF particles.

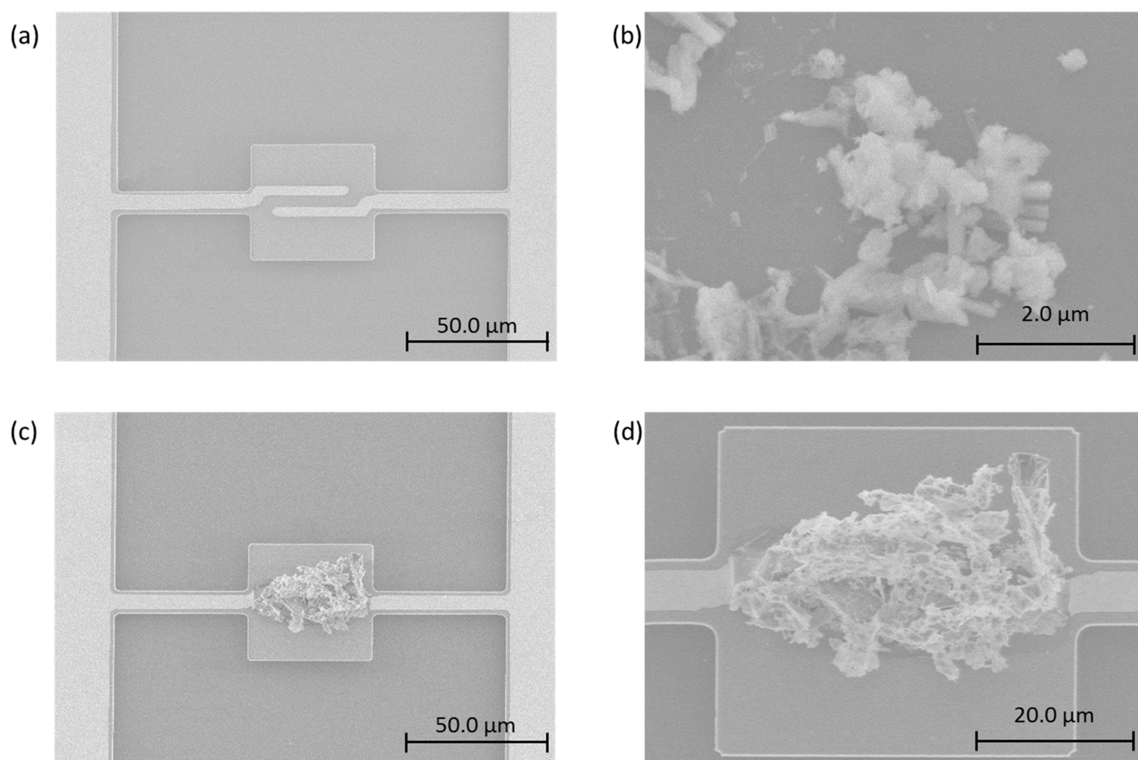

Figure 50. Tilted-view SEM images of the fabricated resonators without ZIFs (left) and with ZIFs (right). ZIF-69 particles assembled on the surface of the resonator are shown as an inset.

6.3 Test setup for self-oscillating

The motions of the ZIF-coupled gas sensors are measured at room temperature with a test setup that consists of a Laser Doppler vibrometer (LDV, Polytec OFV-5000) and a custom-built vacuum chamber, as illustrated in Figure 51. Resonator vibration is differentially detected using two laser signals, one focused on the resonator and the other focused on the anchor of the resonator.

The real time mass sensing is enabled by the incorporation of the resonator into a closed-loop to satisfy Barkhausen criteria that the loop gain of the system is equal to unity and the phase shift

around the loop is zero or an integer multiple of 2π for oscillation at the resonant frequency, as presented in Figure 51 (b). Namely,

Equation 20

$$|H(j\omega)G(j\omega)| = 1$$

$$\measuredangle[H(j\omega)G(j\omega)] = 2\pi n, \ (n = 0, \pm 1, \pm 2\ldots)$$

Here, *H(jω)* is a frequency response of the resonator itself, and *G(jω)* is a frequency response of the feedback circuit. Given the mechanical resonator with nonzero dissipation, it is clear that the resonator itself does not satisfy the Barkhausen criteria without the auxiliary feedback circuit for oscillation [73].

The feedback circuit for a self-sustainable oscillation consists of a gain control, a phase control, and low pass filter in sequence. A schematic for the circuit is illustrated in Figure 51 (b). The first stage for the gain control employs an inverting amplifier with a variable gain, which is determined by

Equation 21

$$Gain = -\frac{R_x}{R_{gain}}$$

By changing the resistance of *Rx*, the gain of the feedback circuit is controllable so as to maintain unity loop gain. The resonator itself has a gain less than 1, and thus its gain requires to be amplified by a following positive feedback, whereas in this case the resonating part (including the LDV system) excluding the feedback circuit has a gain greater than 1. The conversion of mechanical motion to an electrical output signal by the LDV system results in a gain greater than unity. Therefore, the first stage of the feedback circuit is to lower the gain to unity.

The second stage is an active all-pass filter having a unity gain, and the resistor at the positive input terminal of the amplifier controls the phase of this stage. The phase of the second stage is

Equation 22

$$Phase = 180° - 2tan^{-1}(\omega R_y C_{phase})$$

The phase of the second stage varies between $0°$ and $180°$ with the variable resistance of Ry.

At the third stage, a low pass filter removes low frequency signals that can impose drift to the overall system by improper bias. A resistor and a capacitor readily achieve the low pass filter. The third stage is followed by a buffer that isolates the entire feedback circuit from the resonator in order to avoid a loading effect of the resonator on the oscillation circuit. Values of components used in the feedback circuit are compared in Table 7.

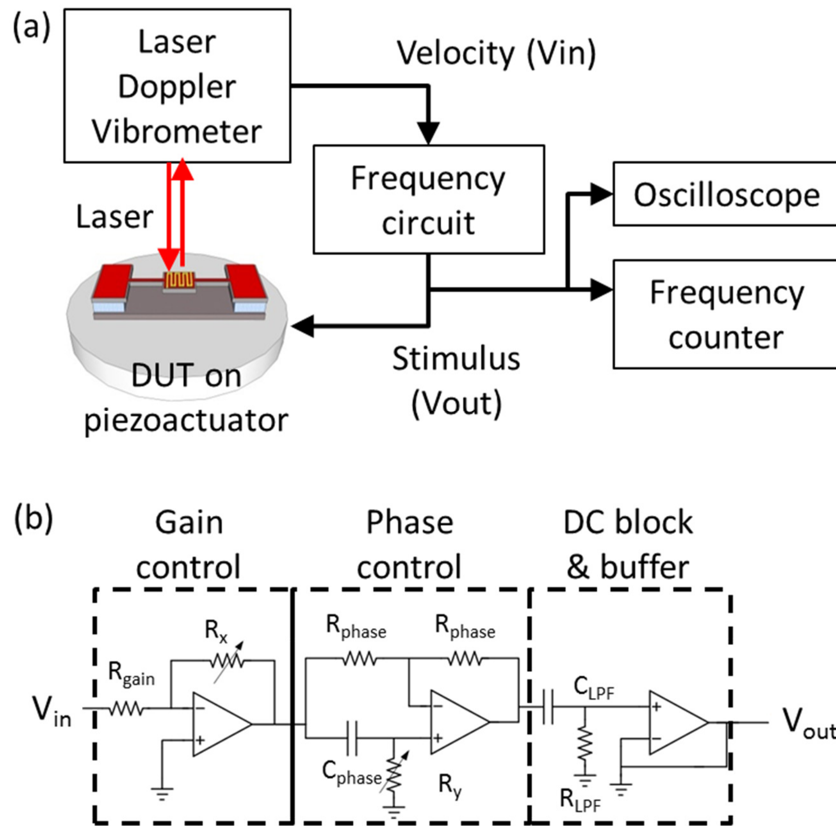

Figure 51. (a) Experimental setup for the self-oscillation of the resonator. (b) Schematic diagram of the feedback circuit.

Table 7. Summary of the feedback circuit design.

Function	Parameter	Value
Gain control stage	R_{gain}	20 kΩ
	R_x	0 – 5 kΩ
Phase control stage	R_{phase}	2 kΩ
	C_{phase}	1 nF
	R_y	0 -5 kΩ
DC block & buffer stage	C_{LPR}	100 pF
	R_{LPF}	6 kΩ

6.4 Experimental results

Figure 52 shows $\Delta f/f_0$ resulting from adsorption of different gases and the responses to gas of the silicon resonators with and without ZIF coupling using an open-loop connected by a network analyzer. Inset is a set of frequency spectra showing change of resonant frequency by adsorption of 2500 ppm CO_2. The ZIF-coupled resonator has a Q factor of 1600.

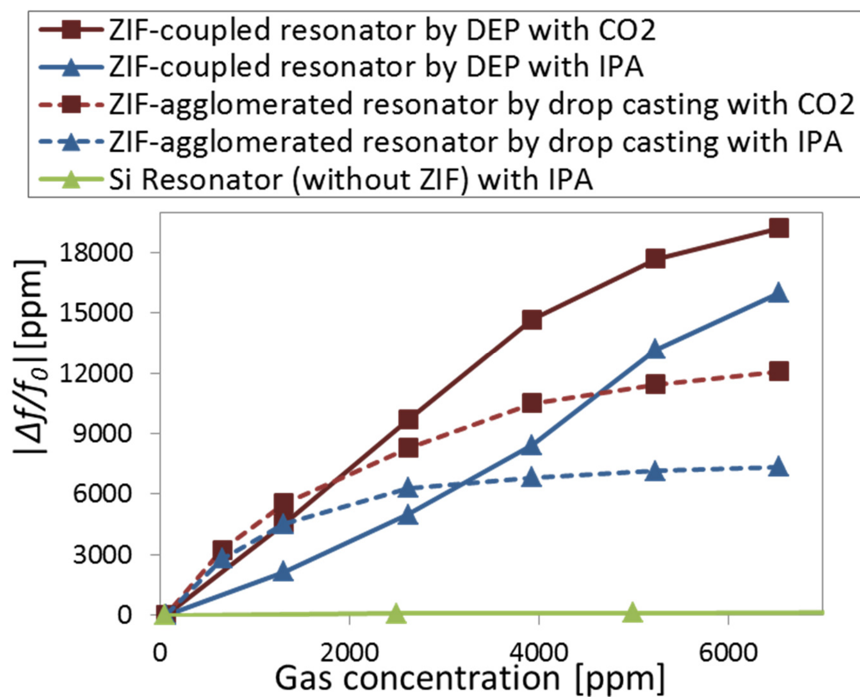

Figure 52. Sensing responses of the ZIF-coupled resonant gas sensors as a function of IPA/CO_2 gas concentration. The resonator with ZIFs assembled by DEP shows higher sensitivity than the resonator with ZIFs agglomerated by drop casting.

Whereas the frequency shifts of the silicon resonator without ZIFs during gas adsorption are almost negligible due to the insufficient adsorption, the resonant frequency of the ZIF-coupled resonators changes substantially due to the increase in surface area afforded by assembled ZIFs.

The results are compared with the ZIF-agglomerated resonator of Chapter 5, which are obtained using the ZIF-agglomerated resonator through a drop casting method. Since the agglomerated ZIFs are likely to obstruct further adsorption of gas into internal ZIFs, the response saturates and the sensitivity gets lower for higher gas concentration range. On the other hand, scattered ZIFs, which are assembled by DEP, have increased exposure to the surrounding environment so as to make maximum contact with gas analytes. Hence, the responses of the ZIF-coupled resonator are approximately linear for entire concentration ranges, indicating that the gas analytes are smoothly transferred to each assembled ZIF particle.

As a result, the ZIF-coupled resonators show enhanced sensitivity ranging between 84 and 54% for different gas concentrations compared to the ZIF-agglomerated resonator, and ranging between 44 and 56 times compared to the silicon resonator without ZIF. Furthermore, because of the inherent selectivity of ZIFs, the ZIF-coupled resonator has higher sensitivity to CO_2 than IPA (isopropyl alcohol) in spite of the lighter molar mass of CO_2. Assuming that the frequency shift is affected only by the mass change, the mass adsorbed on ZIF-coupled resonator for a CO_2 concentration of 5200 ppm is calculated to be 108 pg from Equation 11. As an areal mass of CO_2 is calculated as 28 ng/cm^2, adsorbed amount onto the ZIF-coupled resonator corresponds to 78 monolayers on the silicon resonator surface of 4900 μm^2, which implies the adsorption of the ZIF-coupled resonator occurs not only on the surface but also inside the ZIFs as desired. Therefore, the ZIFs enhance the surface area for gas detection, further enabling the sensitivity of the gas sensor to be improved.

Reactions of ZIFs with different gas molecules affect not only the amplitude of frequency shift, but also the time required for adsorption. The real time detection for the resonant frequency is performed with the closed-loop measurements described in section 6.3 with a period of 50

msec, as presented in Figure 53. The ZIF-coupled resonators are exposed to a series of IPA or CO_2 gas pulses. The resonant frequency decreases rapidly during the injection of gas, and then recovers repeatedly to its baseline values upon removal of gas, indicating reversible adsorption. The frequency shifts reach a steady state within less than 10 seconds.

The measured short-term noise floor is presented in the inset of Figure 53 (b). The standard deviation of the resonant frequencies is 13.5 Hz (58 ppm). The minimum detectable mass is calculated as $\delta M = 2m\delta f/f_0$ [104], where m (~3.1×10^{-9} g) and $\delta f/f_0$ are the total mass and noise floor of the resonator, respectively. Hence, the limit of detection of the ZIF-coupled resonator for gas sensing is expected to ~0.35 pg. When 1300 ppm IPA is introduced into the testing chamber, 495 Hz frequency drop is observed that is about 36 times higher than the noise floor.

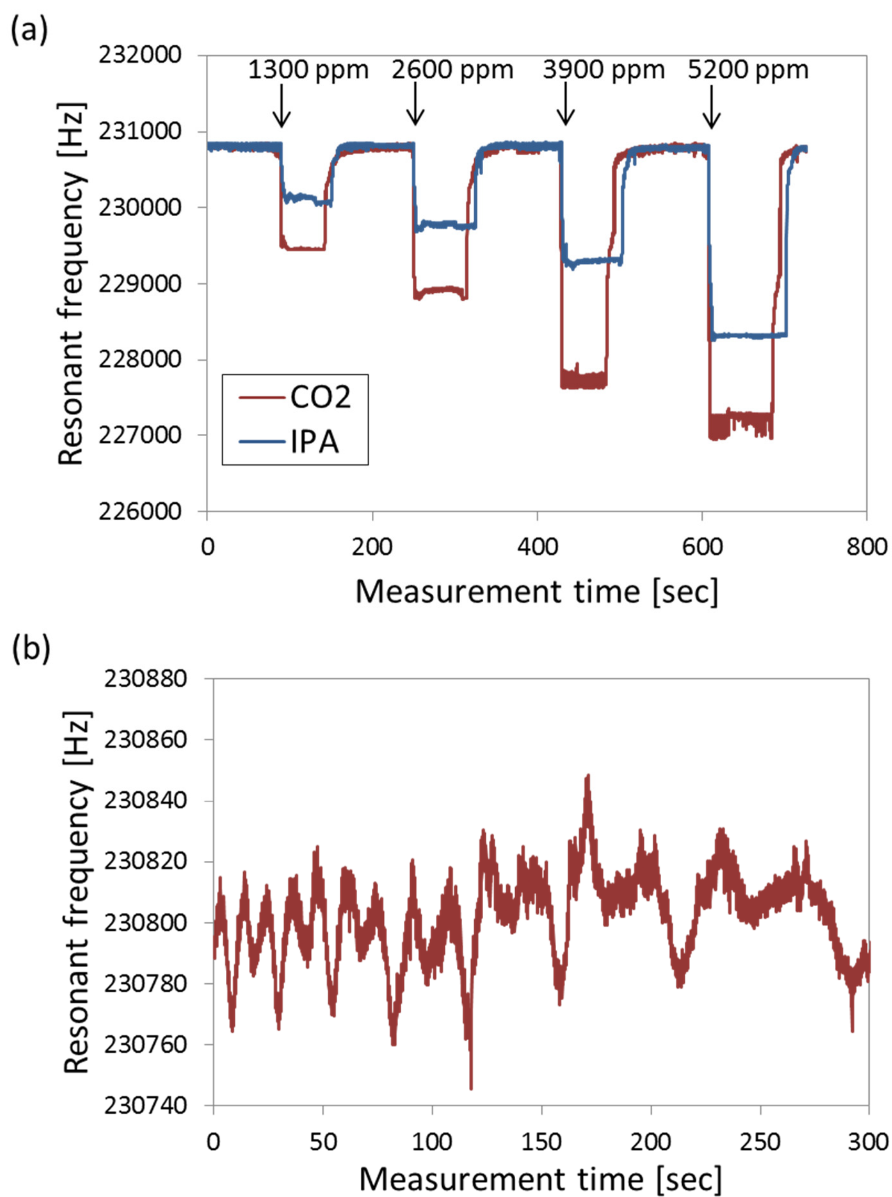

Figure 53. (a) Real time gas sensing experiment with the ZIF-coupled resonator and (b) measured noise floor is over the course of 300 sec. The standard deviation value reflects attainment of ~0.35 pg mass resolution.

During each adsorption, a global fit is performed on the experimental curve according to the time-dependent exponential decay of resonant frequency,

Equation 23

$$f(t) = \Delta f exp[-(t/\tau)]$$

where Δf is the amplitude of frequency shift, and τ is the decay constant, as shown in Figure 54. Table 8 compares the fit parameters that depend on both the concentration of the arriving analyte and its selectivity with ZIF-69. The decay constants for IPA and CO_2 are 1.43±0.28 and 0.49±0.17, respectively, which have consistent values depending on chemical specificity of ZIF-69 to gas species. Faster frequency shift with CO_2 is attributed to inherent selectivity of ZIF-69. Accordingly, in addition to their sensitivity enhancement, ZIF-coupled resonator by DEP appears to offer remarkable selectivity. In other words, the distinct response patterns from both amplitude of frequency shift and decay constant can provide information about both species and concentration of specific gas molecules that has adsorbed onto the sensor, indicating significant chemical recognition ability of the ZIF-coupled resonator sensor.

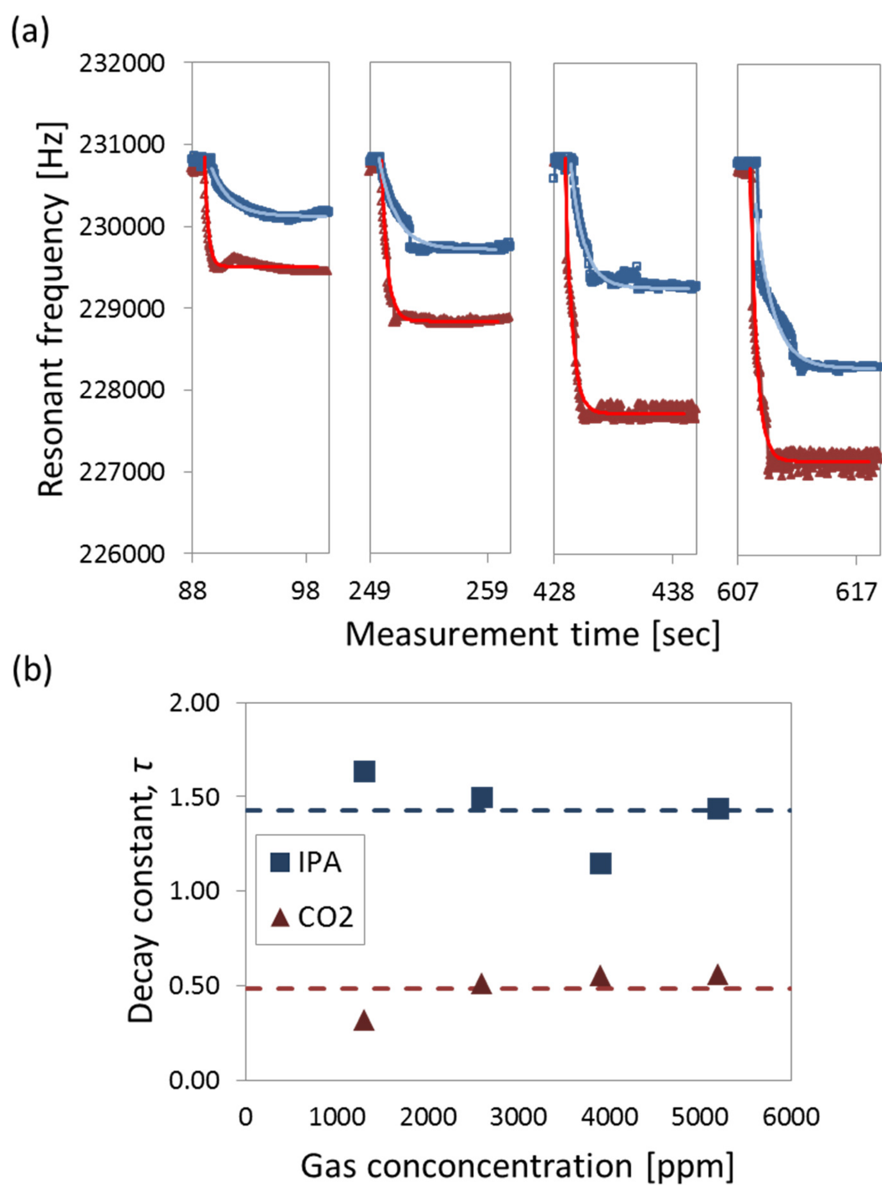

Figure 54. (a) Expanded view of the frequency drop from adsorption of IPA (blue) and CO_2 (red) with a period of 50 msec. The experimental curves are fit to an exponential decay function (light blue and light red solid lines) and the each fitting parameters are compared in Table 8. (b) The decay constants for IPA and CO_2 are 1.43±0.28 and 0.49±0.17, respectively.

Table 8. Fitting parameters of experimental frequency drops arising from different concentration of IPA and CO_2.

Gas	IPA		CO_2	
Concentration [ppm]	Frequency shift, Δf	Decay constant, τ	Frequency shift, Δf	Decay constant, τ
1300	606.64	1.64	1460.54	0.32
2600	1110.26	1.49	2246.66	0.51
3900	1519.30	1.14	3547.28	0.55
5200	2203.10	1.44	3629.07	0.56

In summary, DEP properties for ZIF-69 were studied for the first time, and the assembly technique using DEP force on a freestanding MEMS structure was also investigated. This study demonstrated sensitivity and selectivity improvement of chemical vapor sensing using ZIF-coupled resonators, which have ultrahigh surface area as compared to solid resonators. By using a microscale device with nanoscale features, the advantages of both size scales could be leveraged (*i.e.*, microscale capture area with nanoscale sensitivity).

Chapter 7 Conclusions

Either decreasing the dimensions of the resonator or increasing the adsorbed mass is a viable method to improve sensitivity of a resonant sensor (*i.e.*, larger fractional frequency shifts (Δf / f_0)). Scaling down of the device brings additional challenges, such as limited operating environment, reduction of quality factor, and increase in accumulation time required to adsorb analytes in low concentration. This study developed highly porous surfaces to provide both the sensitivity of nanoscale devices with the capture area of microscale devices and the selectivity to desired analytes. For this purpose, the silicon micromechanical resonant sensors with different porous treatments were fabricated at the Nanoelectronics Research Facility at UCLA.

Firstly, a porous silicon surface directly formed on the resonator surface was studied because it can be developed with little added complexity to fabrication, functionalization, and readout, which may be accompanied with an addition of surface coating. Using the electroless metal-assisted method, characteristics of resonant sensors with nonporous silicon, fully-porous silicon, and partially-porous silicon surfaces were compared. It was demonstrated that the sensor resolution can be optimized by using partially-porous resonators to achieve a better combination of sensitivity and quality factor. The chemical functionalization of the partially-porous resonators was also investigated, enabling the sensor to have further enhancement of the sensitivity of more than just the physical limits of the structure itself. 6.5 times enhancement of sensitivity and 26% improvement of resolution were demonstrated using the partially-porous silicon resonator with 4-MBA coating, compared with the silicon resonator without any porous treatment or functionalization.

Next, surface micromachined nanoparticle-coupled resonant sensors were designed and evaluated. ZIF nanoparticles on the silicon resonator provided the sensitivity improvement due to

their high surface area and the selectivity due to chemical treatment of their organic linkers. To assemble ZIFs with the silicon resonator, drop casting and DEP techniques have been utilized. However, coupling ZIFs requires careful considerations of the thermal and chemical properties of the particles themselves, as well as factors that affect the performance of the sensor. Hence, a novel fabrication technique was developed, allowing deposition of ZIFs on released resonators by providing a temporary support layer of photoresist. The keys of the fabrication of ZIF-coupled resonators are 1) separating etching of the sacrificial layer from assembly of the nanoparticles, 2) using photoresist replacement of sublimated p-dichlorobenzene for temporary support, and 3) assembling ZIFs on targeted regions with either drop casting or DEP technique.

Experimental results demonstrated sensitivity and selectivity improvement of chemical vapor sensing using ZIF-coupled resonators, which have ultrahigh surface area as compared to the solid silicon resonators. The ZIF-coupled resonators by the DEP showed enhanced sensitivity up to 84% for compared to the ZIF-agglomerated resonator by the drop casting, and 158 times compared to the silicon resonator without ZIF. Moreover, the distinct response patterns from both amplitude of frequency shift and decay constant can provide information about discrimination and concentration and of specific gas molecules that has adsorbed onto the sensor.

Four major contributions resulted from this work: (1) By using a microscale device with nanoscale features, the advantages of both size scales could be leveraged (*i.e.*, microscale capture area with nanoscale sensitivity). (2) By coupling ZIF nanoparticles, significant chemical recognition ability of the microfabricated resonant sensor was validated with experiments. (3) A process was presented for localizing nanoparticles that are not compatible with standard microfabrications on the surface of MEMS/NEMS devices. This technique is applicable to enable a wide range of nanoparticles to be assembled with MEMS/NEMS devices, making

resonators useful for a wide variety of adsorption-based sensing applications. (4) DEP phenomena for ZIFs were studied, and were utilized to manipulate ZIFs onto the resonant devices.

Future work for better resolution, sensitivity and selectivity studies of the resonant sensors could include studies of structure design to gain higher quality factor [116-118], adsorption-induced surface stress and its effect on resonant frequency to assemble more ZIFs without a counterbalanced resonant frequency shift due to the stress change [99, 119], and separated responses for various chemical compounds and their mixtures [21, 120].

REFERENCES

[1] M. Vilaseca, J. Coronas, A. Cirera, A. Cornet, J. R. Morante, and J. Santamaria, "Gas detection with SnO2 sensors modified by zeolite films," *Sensors and Actuators B-Chemical,* vol. 124, pp. 99-110, Jun. 2007.

[2] B. Sixou, N. Mermilliod, and J. P. Travers, "Aging effects on the transport properties in conducting polymer polypyrrole," *Physical Review B,* vol. 53, pp. 4509-4521, Feb. 1996.

[3] X. X. Jin, Y. Huang, A. Mason, and X. Q. Zeng, "Multichannel Monolithic Quartz Crystal Microbalance Gas Sensor Array," *Analytical Chemistry,* vol. 81, pp. 595-603, Jan. 2009.

[4] A. Z. Sadek, W. Wlodarski, K. Shin, R. B. Kaner, and K. Kalantar-zadeh, "A layered surface acoustic wave gas sensor based on a polyaniline/In2O3 nanofibre composite," *Nanotechnology,* vol. 17, pp. 4488-4492, Sep. 2006.

[5] N. Ledermann, P. Muralt, J. Baborowski, S. Gentil, K. Mukati, M. Cantoni, A. Seifert, and N. Setter, "{100}-textured, piezoelectric Pb(Zr-x Ti1-x)O-3 thin films for MEMS: integration, deposition and properties," *Sensors and Actuators a-Physical,* vol. 105, pp. 162-170, Jul. 2003.

[6] B. D. Spangler, E. A. Wilkinson, J. T. Murphy, and B. J. Tyler, "Comparison of the Spreeta (R) surface plasmon resonance sensor and a quartz crystal microbalance for detection of Escherichia coli heat-labile enterotoxin," *Analytica Chimica Acta,* vol. 444, pp. 149-161, Oct. 2001.

[7] A. S. Webb, F. Poletti, D. J. Richardson, and J. K. Sahu, "Suspended-core holey fiber for evanescent-field sensing," *Optical Engineering,* vol. 46, Jan. 2007.

[8] D. R. Walt, T. Dickinson, J. White, J. Kauer, S. Johnson, H. Engelhardt, J. Sutter, and P. Jurs, "Optical sensor arrays for odor recognition," *Biosensors & Bioelectronics,* vol. 13, pp. 697-699, Sep. 1998.

[9] M. Haurylau, A. R. Shroff, and P. M. Fauchet, "Optical properties and tunability of macroporous silicon 2-D photonic bandgap structures," *Physica Status Solidi a-Applications and Materials Science,* vol. 202, pp. 1477-1481, Jun. 2005.

[10] O. Bisi, S. Ossicini, and L. Pavesi, "Porous silicon: a quantum sponge structure for silicon based optoelectronics," *Surface Science Reports,* vol. 38, pp. 1-126, Apr. 2000.

[11] J. A. Covington, J. W. Gardner, D. Briand, and N. F. de Rooij, "A polymer gate FET sensor array for detecting organic vapours," *Sensors and Actuators B-Chemical,* vol. 77, pp. 155-162, Jun. 2001.

[12] S. Joo and R. B. Brown, "Chemical sensors with integrated electronics," *Chemical Reviews,* vol. 108, pp. 638-651, Feb. 2008.

[13] D. Briand, H. Sundgren, B. van der Schoot, I. Lundstrom, and N. F. de Rooij, "Thermally isolated MOSFET for gas sending application," *IEEE Electron Device Letters,* vol. 22, pp. 11-13, Jan. 2001.

[14] G. Stoney, "The measurement of stress in layered structures," in *Proc. Royal Society A*, London, U.K., 1909, pp. 172-182.

[15] G. H. Wu, R. H. Datar, K. M. Hansen, T. Thundat, R. J. Cote, and A. Majumdar, "Bioassay of prostate-specific antigen (PSA) using microcantilevers," *Nature Biotechnology,* vol. 19, pp. 856-860, Sep. 2001.

[16] J. W. Ndieyira, M. Watari, A. D. Barrera, D. Zhou, M. Vogtli, M. Batchelor, M. A. Cooper, T. Strunz, M. A. Horton, C. Abell, T. Rayment, G. Aeppli, and R. A. Mckendry, "Nanomechanical detection of antibiotic mucopeptide binding in a model for superbug drug resistance," *Nature Nanotechnology,* vol. 3, pp. 691-696, Nov. 2008.

[17] M. Weinberg, R. Candler, S. Chandorkar, J. Varsanik, T. Kenny, and A. Duwel, "Energy loss in mems resonators and the impact on inertial and rf devicesenergy loss in mems resonators and the impact on inertial and rf devices," in *Proc. International Conference on Solid-State Sensors, Actuators and Microsystems (Transducers)*, Denver, USA, 2009.

[18] Y. S. Jung, W. Jung, H. L. Tuller, and C. A. Ross, "Nanowire Conductive Polymer Gas Sensor Patterned Using Self-Assembled Block Copolymer Lithography," *Nano Letters,* vol. 8, pp. 3776-3780, Nov. 2008.

[19] M. Vilaseca, C. Yagüe, J. Coronas, and J. Santamaria, "Development of QCM sensors modified by AlPO4-18 films," *Sensors and Actuators B: Chemical,* vol. 117, pp. 143-150, Sep. 2006.

[20] Z. Jin, Y. X. Su, and Y. X. Duan, "Development of a polyaniline-based optical ammonia sensor," *Sensors and Actuators B-Chemical,* vol. 72, pp. 75-79, Jan. 2001.

[21] M. Li, E. B. Myers, H. X. Tang, S. J. Aldridge, H. C. McCaig, J. J. Whiting, R. J. Simonson, N. S. Lewis, and M. L. Roukes, "Nanoelectromechanical Resonator Arrays for Ultrafast, Gas-Phase Chromatographic Chemical Analysis," *Nano Letters,* vol. 10, pp. 3899-3903, Oct. 2010.

[22] M. R. Willis, K. J. Markland, and M. R. Fahy, "Organic Films for Seebeck Effect Gas Detectors," *Synthetic Metals,* vol. 28, pp. C781-C786, Jan. 1989.

[23] D. Monroe, "Potentiometric (Bioselective Electrodes) Assay Systems - Utility and Limitations," *Critical Reviews in Clinical Laboratory Sciences,* vol. 27, pp. 109-158, Jan. 1989.

[24] J. Ngehngwainbi, A. A. Suleiman, and G. G. Guilbault, "Piezoelectric Crystal Biosensors," *Biosensors & Bioelectronics,* vol. 5, pp. 13-26, Apr. 1990.

[25] A. K. Naik, M. S. Hanay, W. K. Hiebert, X. L. Feng, and M. L. Roukes, "Towards single-molecule nanomechanical mass spectrometry," *Nature Nanotechnology,* vol. 4, pp. 445-450, Jul. 2009.

[26] P. S. Waggoner and H. G. Craighead, "Micro- and nanomechanical sensors for environmental, chemical, and biological detection," *Lab on a Chip,* vol. 7, pp. 1238-1255, Oct. 2007.

[27] K. L. Ekinci and M. L. Roukes, "Nanoelectromechanical systems," *Review of Scientific Instruments,* vol. 76, p. 061101, May 2005.

[28] Y. T. Yang, C. Callegari, X. L. Feng, K. L. Ekinci, and M. L. Roukes, "Zeptogram-scale nanomechanical mass sensing," *Nano Letters,* vol. 6, pp. 583-586, Apr. 2006.

[29] B. Ilic, Y. Yang, and H. G. Craighead, "Virus detection using nanoelectromechanical devices," *Applied Physics Letters,* vol. 85, pp. 2604-2606, Sep. 2004.

[30] Y. Wang, J. A. Henry, A. T. Zehnder, and M. A. Hines, "Surface chemical control of mechanical energy losses in micromachined silicon structures," *Journal of Physical Chemistry B,* vol. 107, pp. 14270-14277, Dec. 2003.

[31] X. Li, "Cantilever sensors equipped with nano sensing effects for ultra-sensitive detection of bio/chemical molecules," in *Proc. Transducers*, 2009, pp. 1620-1625.

[32] P. A. Truitt, J. B. Hertzberg, C. C. Huang, K. L. Ekinci, and K. C. Schwab, "Efficient and sensitive capacitive readout of nanomechanical resonator arrays," *Nano Letters,* vol. 7, pp. 120-126, Jan. 2007.

[33] L. Sekaric, D. W. Carr, S. Evoy, J. M. Parpia, and H. G. Craighead, "Nanomechanical resonant structures in silicon nitride: fabrication, operation and dissipation issues," *Sensors and Actuators A: Physical,* vol. 101, pp. 215-219, Sep. 2002.

[34] N. Sepulveda, D. Aslam, and J. P. Sullivan, "Polycrystalline diamond MEMS resonator technology for sensor applications," in *Proc. Diamond and Related Materials*, 2006, pp. 398–403.

[35] A. D. O'Connell, M. Hofheinz, M. Ansmann, R. C. Bialczak, M. Lenander, E. Lucero, M. Neeley, D. Sank, H. Wang, M. Weides, J. Wenner, J. M. Martinis, and A. N. Cleland, "Quantum ground state and single-phonon control of a mechanical resonator," *Nature,* vol. 464, pp. 697-703, Apr. 2010.

[36] P. E. Sheehan and L. J. Whitman, "Detection limits for nanoscale biosensors," *Nano Letters,* vol. 5, pp. 803-807, Apr. 2005.

[37] D. T. Pritchard and J. A. Currie, "Diffusion of coefficients of carbon dioxide, nitrous oxide, ethylene and ethane in air and their measurement," *Journal of Soil Science,* vol. 33, pp. 175-184, 1982.

[38] D. W. Carr, S. Evoy, L. Sekaric, H. G. Craighead, and J. M. Parpia, "Measurement of mechanical resonance and losses in nanometer scale silicon wires," *Applied Physics Letters,* vol. 75, pp. 920-922, Aug. 1999.

[39] K. Y. Yasumura, T. D. Stowe, E. M. Chow, T. Pfafman, T. W. Kenny, B. C. Stipe, and D. Rugar, "Quality factors in micron- and submicron-thick cantilevers," *Journal of Microelectromechanical Systems,* vol. 9, pp. 117-125, Mar. 2000.

[40] J. L. Yang, T. Ono, and M. Esashi, "Investigating surface stress: Surface loss in ultrathin single-crystal silicon cantilevers," *Journal of Vacuum Science & Technology B,* vol. 19, pp. 551-556, Apr. 2001.

[41] B. H. Houston, D. M. Photiadis, M. H. Marcus, J. A. Bucaro, X. Liu, and J. F. Vignola, "Thermoelastic loss in microscale oscillators," *Applied Physics Letters,* vol. 80, pp. 1300-1302, Feb. 2002.

[42] T. Mattila, J. Kiihamaki, T. Lamminmaki, O. Jaakkola, P. Rantakari, A. Oja, H. Seppa, H. Kattelus, and I. Tittonen, "A 12 MHz micromechanical bulk acoustic mode oscillator," *Sensors and Actuators a-Physical,* vol. 101, pp. 1-9, Sep. 2002.

[43] W. Duffy, "Acoustic Quality Factor of Aluminum-Alloys from 50 Mk to 300-K," *Journal of Applied Physics,* vol. 68, pp. 5601-5609, Dec. 1990.

[44] D. F. McGuigan, C. C. Lam, R. Q. Gram, A. W. Hoffman, D. H. Douglass, and H. W. Gutche, "Measurements of the mechanical Q of single-crystal silicon at low temperatures," *Journal of Low Temperature Physics,* vol. 30, pp. 621-629, Mar. 1978.

[45] R. N. Kleiman, G. Agnolet, and D. J. Bishop, "2-Level Systems Observed in the Mechanical-Properties of Single-Crystal Silicon at Low-Temperatures," *Physical Review Letters,* vol. 59, pp. 2079-2082, Nov. 1987.

[46] L. Khine, M. Palaniapan, and W. Wai-Kin, "6Mhz Bulk-Mode Resonator with Q Values Exceeding One Million," in *Solid-State Sensors, Actuators and Microsystems Conference, 2007 (TRANSDUCERS 2007)*, 2007, pp. 2445-2448.

[47] D. S. Greywall, "Micromechanical RF filters excited by the Lorentz force," *Journal of Micromechanics and Microengineering,* vol. 9, pp. 78-84, Mar. 1999.

[48] T. O. Rocheleau, T. L. Naing, R. Zeying, and C. T. C. Nguyen, "Acoustic whispering gallery mode resonator with Q >109,000 at 515MHz," in *IEEE Micro Electro Mechanical Systems (2012 MEMS)*, 2012, pp. 672-675.

[49] M. D. LaHaye, J. Suh, P. M. Echternach, K. C. Schwab, and M. L. Roukes, "Nanomechanical measurements of a superconducting qubit," *Nature,* vol. 459, pp. 960-964, Jun. 2009.

[50] T. R. Albrecht, P. Grutter, D. Horne, and D. Rugar, "Frequency-Modulation Detection Using High-Q Cantilevers for Enhanced Force Microscope Sensitivity," *Journal of Applied Physics,* vol. 69, pp. 668-673, Jan. 1991.

[51] J. M. Lauerhaas, G. M. Credo, J. L. Heinrich, and M. J. Sailor, "Reversible luminescence quenching of porous silicon by solvents," *Journal of the American Chemical Society,* vol. 114, pp. 1911-1912, Feb. 1992.

[52] R. C. Anderson, R. S. Muller, and C. W. Tobias, "Investigations of Porous Silicon for Vapor Sensing," *Sensors and Actuators a-Physical,* vol. 23, pp. 835-839, Apr. 1990.

[53] G. Gesele, J. Linsmeier, V. Drach, J. Fricke, and R. ArensFischer, "Temperature-dependent thermal conductivity of porous silicon," *Journal of Physics D-Applied Physics,* vol. 30, pp. 2911-2916, Nov. 1997.

[54] T. A. Desai, W. H. Chu, M. Ferrari, G. Rasi, P. Sinibaldi-Vallebona, P. Borboni, G. Beattie, and A. Hayek, "Implantation of microfabricated immunoisolating biocapsules," in *Proc. SPIE*, 1998, pp. 40-47.

[55] P. G. Datskos, N. V. Lavrik, and M. J. Sepaniak, "Detection of explosive compounds with the use of microcantilevers with nanoporous coatings," *Sensor Letters,* vol. 1, pp. 25-32, Dec. 2003.

[56] P. C. Xu, H. T. Yu, and X. X. Li, "Functionalized Mesoporous Silica for Microgravimetric Sensing of Trace Chemical Vapors," *Analytical Chemistry,* vol. 83, pp. 3448-3454, May 2011.

[57] R. N. Candler, A. Duwel, M. Varghese, S. A. Chandorkar, M. A. Hopcroft, W. T. Park, B. Kim, G. Yama, A. Partridge, M. Lutz, and T. W. Kenny, "Impact of geometry on thermoelastic dissipation in micromechanical resonant beams," *Journal of Microelectromechanical Systems,* vol. 15, pp. 927-934, Aug. 2006.

[58] D. Z. Jin, X. X. Li, H. H. Bao, Z. X. Zhang, Y. L. Wang, H. T. Yu, and G. M. Zuo, "Integrated cantilever sensors with a torsional resonance mode for ultraresoluble on-the-spot bio/chemical detection," *Applied Physics Letters,* vol. 90, p. 041901, Jan. 2007.

[59] X. Y. Xia and X. X. Li, "Resonance-mode effect on microcantilever mass-sensing performance in air," *Review of Scientific Instruments,* vol. 79, p. 074301, Jul. 2008.

[60] P. Mohanty, D. A. Harrington, K. L. Ekinci, Y. T. Yang, M. J. Murphy, and M. L. Roukes, "Intrinsic dissipation in high-frequency micromechanical resonators," *Physical Review B,* vol. 66, Aug. 2002.

[61] S. Evoy, D. W. Carr, L. Sekaric, A. Olkhovets, J. M. Parpia, and H. G. Craighead, "Nanofabrication and electrostatic operation of single-crystal silicon paddle oscillators," *Journal of Applied Physics,* vol. 86, pp. 6072-6077, Dec. 1999.

[62] N. Lobontiu, B. Ilic, E. Garcia, T. Reissman, and H. G. Craighead, "Modeling of nanofabricated paddle bridges for resonant mass sensing," *Review of Scientific Instruments,* vol. 77, pp. 073301-9, Jul. 2006.

[63] S.-J. Kim, T. Ono, and M. Esashi, "Mass detection using capacitive resonant silicon resonator employing LC resonant circuit technique," *Review of Scientific Instruments,* vol. 78, pp. 085103-1-6, Aug. 2007.

[64] L. Sujatha and E. Bhattacharya, "Enhancement of the sensitivity of pressure sensors with a composite Si/porous silicon membrane," *Journal of Micromechanics and Microengineering,* vol. 17, pp. 1605-1610, Aug. 2007.

[65] D. Bellet, P. Lamagnere, A. Vincent, and Y. Brechet, "Nanoindentation investigation of the Young's modulus of porous silicon," *Journal of Applied Physics,* vol. 80, pp. 3772-3776, Oct. 1996.

[66] Y.-H. Hwang, F. Gao, and R. N. Candler, "Porous silicon resonators for sensitive vapor detection," in *Proc. Solid State Sensors, Actuators, and Microsystems Workshop (Hilton Head)*, 2010, pp. 150-153.

[67] C. Lee and C.-J. Kim, "Maximizing the Giant Liquid Slip on Superhydrophobic Microstructures by Nanostructuring Their Sidewalls," *Langmuir,* vol. 25, pp. 12812-12818, Jul. 2009.

[68] L. Cao, T. P. Price, M. Weiss, and D. Gao, "Super Water- and Oil-Repellent Surfaces on Intrinsically Hydrophilic and Oleophilic Porous Silicon Films," *Langmuir,* vol. 24, pp. 1640-1643, Jan. 2008.

[69] J. A. Glass, E. A. Wovchko, and J. T. Yates, "Reaction of Methanol with Porous Silicon," *Surface Science,* vol. 338, pp. 125-137, Sep. 1995.

[70] Y. J. Yang, M. A. Gretillat, and S. D. Senturia, "Effect of air damping on the dynamics of nonuniform deformations of microstructures," in *Proc. Transducers*, 1997, pp. 1093-1096.

[71] W. E. Newell, "Miniaturization of Tuning Forks," *Science,* vol. 161, pp. 1320-1326, Sep. 1968.

[72] A. Orsini and A. D'Amico, "Chemical sensors and chemical sensor systems: fundamentals limitations and new trends," in *Advances in Sensing with Security Applications*. vol. 2, ed: Springer Netherlands, 2006, pp. 69-94.

[73] A. N. Cleland and M. L. Roukes, "Noise processes in nanomechanical resonators," *Journal of Applied Physics,* vol. 92, pp. 2758-2769, Jun. 2002.

[74] K. L. Ekinci, X. M. H. Huang, and M. L. Roukes, "Ultrasensitive nanoelectromechanical mass detection," *Applied Physics Letters,* vol. 84, pp. 4469-4471, May 2004.

[75] T. Thundat, E. A. Wachter, S. L. Sharp, and R. J. Warmack, "Detection of Mercury-Vapor Using Resonating Microcantilevers," *Applied Physics Letters,* vol. 66, pp. 1695-1697, Mar. 1995.

[76] T. Thundat, G. Y. Chen, R. J. Warmack, D. P. Allison, and E. A. Wachter, "Vapor Detection Using Resonating Microcantilevers," *Analytical Chemistry,* vol. 67, pp. 519-521, Feb. 1995.

[77] D. Lange, C. Hagleitner, A. Hierlemann, O. Brand, and H. Baltes, "Complementary metal oxide semiconductor cantilever arrays on a single chip: Mass-sensitive detection of volatile organic compounds," *Analytical Chemistry,* vol. 74, pp. 3084-3095, Jul. 2002.

[78] M. K. Baller, H. P. Lang, J. Fritz, C. Gerber, J. K. Gimzewski, U. Drechsler, H. Rothuizen, M. Despont, P. Vettiger, F. M. Battiston, J. P. Ramseyer, P. Fornaro, E. Meyer, and H. J. Guntherodt, "A cantilever array-based artificial nose," *Ultramicroscopy,* vol. 82, pp. 1-9, Feb. 2000.

[79] J. Wang, W. G. Wu, Y. Huang, and Y. L. Hao, "< 100 > n-type metal-oxide-semiconductor field-effect transistor-embedded microcantilever sensor for observing the kinetics of chemical molecules interaction," *Applied Physics Letters,* vol. 95, p. 124101, Sep. 2009.

[80] K. Galatsis, Y. X. Li, W. Wlodarski, E. Comini, G. Sberveglieri, C. Cantalini, S. Santucci, and M. Passacantando, "Comparison of single and binary oxide MoO3, TiO2 and WO3 sol-gel gas sensors," *Sensors and Actuators B-Chemical,* vol. 83, pp. 276-280, Mar. 2002.

[81] T. Braun, M. K. Ghatkesar, N. Backmann, W. Grange, P. Boulanger, L. Letellier, H. P. Lang, A. Bietsch, C. Gerber, and M. Hegner, "Quantitative time-resolved measurement of membrane protein-ligand interactions using microcantilever array sensors," *Nature Nanotechnology,* vol. 4, pp. 179-185, Mar. 2009.

[82] D. Lee, N. Shin, K. H. Lee, and S. Jeon, "Microcantilevers with nanowells as moisture sensors," *Sensors and Actuators B-Chemical,* vol. 137, pp. 561-565, Apr. 2009.

[83] R. Banerjee, A. Phan, B. Wang, C. Knobler, H. Furukawa, M. O'Keeffe, and O. M. Yaghi, "High-throughput synthesis of zeolitic imidazolate frameworks and application to CO2 capture," *Science,* vol. 319, pp. 939-943, Feb. 2008.

[84] J.-R. Li, R. J. Kuppler, and H.-C. Zhou, "Selective gas adsorption and separation in metal-organic frameworks," *Chemical Society Reviews,* vol. 38, pp. 1477-1504, Mar. 2009.

[85] L. J. Murray, M. Dinca, and J. R. Long, "Hydrogen storage in metal-organic frameworks," *Chemical Society Reviews,* vol. 38, pp. 1294-1314, Mar. 2009.

[86] S. Achmann, G. Hagen, J. Kita, I. M. Malkowsky, C. Kiener, and R. Moos, "Metal-Organic Frameworks for Sensing Applications in the Gas Phase," *Sensors,* vol. 9, pp. 1574-1589, Mar. 2009.

[87] G. Lu and J. T. Hupp, "Metal–Organic Frameworks as Sensors: A ZIF-8 Based Fabry–Pérot Device as a Selective Sensor for Chemical Vapors and Gases," *J. Am. Chem. Soc.,* vol. 132, pp. 7832-7833, Jun. 2010.

[88] L. E. Kreno, J. T. Hupp, and R. P. Van Duyne, "Metal-Organic Framework Thin Film for Enhanced Localized Surface Plasmon Resonance Gas Sensing," *Analytical Chemistry,* vol. 82, pp. 8042-8046, Oct. 2010.

[89] M. D. Allendorf, R. J. T. Houk, L. Andruszkiewicz, A. A. Talin, J. Pikarsky, A. Choudhury, K. A. Gall, and P. J. Hesketh, "Stress-induced Chemical Detection Using Flexible Metal-Organic Frameworks," *Journal of the American Chemical Society,* vol. 130, p. 14404, Nov. 2008.

[90] A. L. Robinson, V. L. Stavila, T. R. Zeitler, M. I. White, S. M. Thornberg, J. A. Greathouse, and M. D. Allendorf, "Ultrasensitive Humidity Detection Using Metal-Organic Framework-Coated Microsensors," *Analytical Chemistry,* vol. 84, pp. 7043-7051, Aug. 2012.

[91] A. Phan, C. J. Doonan, F. J. Uribe-Romo, C. B. Knobler, M. O'Keeffe, and O. M. Yaghi, "Synthesis, structure, and carbon dioxide capture properties of zeolitic Imidazolate frameworks," *Accounts of Chemical Research,* vol. 43, pp. 58-67, Jan. 2010.

[92] R. Maboudian and R. T. Howe, "Critical review: Adhesion in surface micromechanical structures," *Journal of Vacuum Science & Technology B,* vol. 15, pp. 1-20, Jan. 1997.

[93] N. Takeshima, K. J. Gabriel, M. Ozaki, J. Takahashi, H. Horiguchi, and H. Fujita, "Electrostatic parallelogram actuators," in *Int. Conf. on Solid-State Sensors and Actuators (Transducers)*, 1991, pp. 63-66.

[94] Y. I. Lee, K. H. Park, J. Lee, C. S. Lee, H. J. Yoo, C. J. Kim, and Y. S. Yoon, "Dry release for surface micromachining with HF vapor-phase etching," *Journal of Microelectromechanical Systems,* vol. 6, pp. 226-233, Sep. 1997.

[95] G. T. Mulhern, D. S. Soane, and R. T. Howe, "Supercritical carbon dioxide drying of microstructures," in *Int. Conf. on Solid-State Sensors and Actuators (Transducers)*, 1993, pp. 296 - 299.

[96] D. Kobayashi, T. Hirano, T. Furuhata, and H. Fujita, "An integrated lateral tunneling unit," in *IEEE MEMS*, 1992, pp. 214-219.

[97] R. Martel, T. Schmidt, H. R. Shea, T. Hertel, and P. Avouris, "Single- and multi-wall carbon nanotube field-effect transistors," *Applied Physics Letters,* vol. 73, pp. 2447-2449, Oct. 1998.

[98] D. Lixin, S. Kaiyu, D. R. Frutiger, A. Subramanian, Z. Li, B. J. Nelson, T. Xinyong, and Z. Xiaobin, "Engineering Multiwalled Carbon Nanotubes Inside a Transmission Electron Microscope Using Nanorobotic Manipulation," *IEEE Transactions on Nanotechnology,* vol. 7, pp. 508-517, Jul. 2008.

[99] G. Y. Chen, T. Thundat, E. A. Wachter, and R. J. Warmack, "Adsorption-induced surface stress and its effects on resonance frequency of microcantilevers," *Journal of Applied Physics,* vol. 77, pp. 3618-3622, Jan. 1995.

[100] P. A. Hartley, G. D. Parfitt, and L. B. Pollack, "The role of the van der Waals force in the agglomeration of powders containing submicron particles," *Powder Technology,* vol. 42, pp. 35-46, 1985.

[101] M. J. Tudor, M. V. Andres, K. W. H. Foulds, and J. M. Naden, "Silicon resonator sensors: interrogation techniques and characteristics," *IEE Proceedings D. Control Theory and Applications,* vol. 135, pp. 364-368, Sep. 1988.

[102] B. Kim, R. N. Candler, M. A. Hopcroft, M. Agarwal, W.-T. Park, and T. W. Kenny, "Frequency stability of wafer-scale film encapsulated silicon based MEMS resonators," *Sensors and Actuators A: Physical,* vol. 136, pp. 125-131, Nov. 2007.

[103] F. Shen, P. Lu, S. J. O'Shea, K. H. Lee, and T. Y. Ng, "Thermal effects on coated resonant microcantilevers," *Sensors and Actuators A: Physical,* vol. 95, pp. 17-23, Aug. 2001.

[104] E. Forsen, G. Abadal, S. Ghatnekar-Nilsson, J. Teva, J. Verd, R. Sandberg, W. Svendsen, F. Perez-Murano, J. Esteve, E. Figueras, F. Campabadal, L. Montelius, N. Barniol, and A. Boisen, "Ultrasensitive mass sensor fully integrated with complementary metal-oxide-semiconductor circuitry," *Applied Physics Letters,* vol. 87, Jul 25 2005.

[105] H. Furukawa, N. Ko, Y. B. Go, N. Aratani, S. B. Choi, E. Choi, A. O. Yazaydin, R. Q. Snurr, M. O'Keeffe, J. Kim, and O. M. Yaghi, "Ultrahigh porosity in metal-organic frameworks," *Science,* vol. 329, pp. 424-428, Jul. 2010.

[106] N. R. Franklin, Y. M. Li, R. J. Chen, A. Javey, and H. J. Dai, "Patterned growth of single-walled carbon nanotubes on full 4-inch wafers," *Applied Physics Letters,* vol. 79, pp. 4571-4573, Dec. 2001.

[107] M. Cantoro, S. Hofmann, S. Pisana, V. Scardaci, A. Parvez, C. Ducati, A. C. Ferrari, A. M. Blackburn, K. Y. Wang, and J. Robertson, "Catalytic chemical vapor deposition of single-wall carbon nanotubes at low temperatures," *Nano Letters,* vol. 6, pp. 1107-1112, Jun. 2006.

[108] Y. Huang, X. F. Duan, Q. Q. Wei, and C. M. Lieber, "Directed assembly of one-dimensional nanostructures into functional networks," *Science,* vol. 291, pp. 630-633, Jan. 2001.

[109] N. Wang, B. J. Bowers, and D. P. Arnold, "Wax-bonded NdFeB micromagnets for microelectromechanical systems applications," *Journal of Applied Physics,* vol. 103, Apr. 2008.

[110] T. Honegger, K. Berton, E. Picard, and D. Peyrade, "Determination of Clausius--Mossotti factors and surface capacitances for colloidal particles," *Applied Physics Letters,* vol. 98, pp. 181906-3, May 2011.

[111] N. G. Green and H. Morgan, "Dielectrophoresis of submicrometer latex spheres. 1. Experimental results," *Journal of Physical Chemistry B,* vol. 103, pp. 41-50, Jan. 1999.

[112] J. Oh, R. Hart, J. Capurro, and H. Noh, "Comprehensive analysis of particle motion under non-uniform AC electric fields in a microchannel," *Lab on a Chip,* vol. 9, pp. 62-78, Oct. 2009.

[113] O. H. Paydar, C. N. Paredes, and R. N. Candler, "Three Dimensionally-Printed (3DP) Microfluidic Devices," in *Proc. Solid State Sensors, Actuators, and Microsystems Workshop (Hilton Head)*, Hilton Head, 2012, pp. 217-220.

[114] I. F. Sbalzarini and P. Koumoutsakos, "Feature point tracking and trajectory analysis for video imaging in cell biology," *Journal of Structural Biology,* vol. 151, pp. 182-195, Aug. 2005.

[115] P. D. Hoffman and Y. X. Zhu, "Double-layer effects on low frequency dielectrophoresis-induced colloidal assembly," *Applied Physics Letters,* vol. 92, Jun. 2008.

[116] W. Pang, L. Yan, H. Zhang, H. Y. Yu, E. S. Kim, and W. C. Tang, "Femtogram mass sensing platform based on lateral extensional mode piezoelectric resonator," *Applied Physics Letters,* vol. 88, Jun. 2006.

[117] Y. W. Lin, S. Lee, S. S. Li, Y. Xie, Z. Y. Ren, and C. T. C. Nguyen, "Series-resonant VHF micromechanical resonator reference oscillators," *Ieee Journal of Solid-State Circuits,* vol. 39, pp. 2477-2491, Dec. 2004.

[118] K. Wang, A. C. Wong, and C. T. C. Nguyen, "VHF free-free beam high-Q micromechanical resonators," *Journal of Microelectromechanical Systems,* vol. 9, pp. 347-360, Sep. 2000.

[119] P. Kapa, L. Pan, A. Bandhanadham, J. Fang, K. Varahramyan, W. Davis, and H. F. Ji, "Moisture measurement using porous aluminum oxide coated microcantilevers," *Sensors and Actuators B-Chemical,* vol. 134, pp. 390-395, Sep. 2008.

[120] S. Ampuero and J. O. Bosset, "The electronic nose applied to dairy products: a review," *Sensors and Actuators B-Chemical,* vol. 94, pp. 1-12, Aug. 2003.